Heliyon 10 (2024) e33023

Contents lists available at ScienceDirect

Heliyon

journal homepage: www.cell.com/heliyon

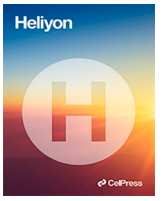

Review article

Ink-based additive manufacturing for electrochemical applications

Runzhi Zhang [a], Tao Sun [a,b,*]

[a] Department of Materials Science and Engineering, University of Virginia, Charlottesville, VA, USA
[b] Department of Mechanical Engineering, Northwestern University, Evanston, IL, USA

A B S T R A C T

Additive manufacturing (AM), commonly known as three-dimensional (3D) printing, has drawn substantial attention in recent decades due to its efficiency and precise control in part fabrication. The limitations of conventional fabrication processes, especially regarding geometry complexity, supply chain, and environmental impact, have prompted the exploration of diverse AM technologies in electrochemistry. Especially, three ink-based AM techniques, binder jet printing (BJP), direct ink writing (DIW), and Inkjet Printing (IJP), have been extensively applied by numerous research teams to produce electrodes, catalyst scaffolds, supercapacitors, batteries, etc. BJP's versatility in utilizing a wide range of materials as powder feedstock promotes its potential for various electrode and battery applications. DIW and IJP stand out for their ability to handle multi-material manufacturing tasks and deliver high printing resolution. To capture recent advancements in this field, we present a comprehensive review of the applications of BJP, DIW, and IJP techniques in fabricating electrochemical devices and components. This review intends to provide an overview of the process-structure-property relationship in electrochemical materials and components across diverse applications manufactured using AM techniques. We delve into how the significantly improved design freedom over the structure offered by these ink-based AM techniques highlights the performance of electrochemical products. Moreover, we highlight their advantages in terms of material compatibility, geometry control, and cost-effectiveness. In specific cases, we also compare the performance of electrochemical components fabricated using AM and conventional manufacturing methods. Finally, we conclude this review article by offering some insights into the future development in this research field.

1. Introduction

The Fourth Industrial Revolution (or Industry 4.0), marked by the fusion of digital technologies with physical systems, has created a new era of innovation and transformation across industries worldwide. This new-era shift holds a profound influence on electrochemical applications, particularly when combined with the capabilities of additive manufacturing (AM) [1,2]. Industry 4.0 represents a fundamental change in manufacturing, featuring interconnectedness, automation, data exchange, and real-time analytics. These elements revolutionize traditional production processes, unlocking unprecedented levels of efficiency, agility, and customization. In the field of electrochemistry, this technological advancement holds great promise to change the design, fabrication, and performance of electrochemical devices. These devices, used as batteries, catalysts, environmental monitors, fuel cells, sensors, and more, are essential in satisfying the personnel and societal needs in a fast-changing decentralized global manufacturing landscape [3,4].

One of the advantages of AM lies in its unique capability and flexibility in design. Traditional manufacturing techniques often have constraints on the geometry and architecture of electrochemical components, limiting their performance and functionality. In contrast, AM techniques offered designers unprecedented freedom to realize complex, crucially structured electrodes, electrolytes, and other important elements in electrochemical systems. This freedom enables the optimization of device performance by tailoring the internal microstructures and surface morphologies to increase mass transport, charge transfer kinetics, and overall electrochemical activity. Moreover, AM facilitates researchers and engineers to explore innovative designs and materials that were previously unattainable

* Corresponding author. Department of Materials Science and Engineering, University of Virginia, Charlottesville, VA, USA
E-mail address: taosun@northwestern.edu (T. Sun).

https://doi.org/10.1016/j.heliyon.2024.e33023
Received 18 January 2024; Received in revised form 28 May 2024; Accepted 12 June 2024
Available online 14 June 2024

using conventional fabrication methods. By using advanced materials such as conductive polymers, metal alloys, nanocomposites, and even biocompatible substrates, AM enables the creation of multifunctional and hybrid electrochemical architectures with better properties, such as improved mechanical strength, chemical stability, and biocompatibility [5]. These capabilities open new frontiers in the development of next-generation electrochemical devices with modified properties and functionalities optimized for specific applications, ranging from wearable biosensors to high-performance energy storage systems. Furthermore, the inherent scalability and cost-effectiveness of AM technologies promote access to advanced manufacturing capabilities, particularly for small and medium-sized enterprises and academic research institutions [5]. Traditional manufacturing processes often entail high setup costs, long lead times, and limited scalability, posing barriers to innovation and commercialization. In contrast, AM platforms provide rapid prototyping capabilities, enabling researchers and engineers to iterate designs quickly and cost-effectively, as shown in Fig. 1. This accelerated innovation cycle accelerates the translation of research findings into real-world applications, driving progress in fields such as batteries, fuel cells, and electrochemical sensors [6–8].

In the context of Industry 4.0, researchers can collect comprehensive data on electrochemical processes on important performance metrics such as temperature, pressure, flow rate, and electrochemical impedance. This abundance of data enables the implementation of advanced process control strategies, predictive maintenance algorithms, and machine learning models to improve device performance, increase operational lifespans, and minimize downtime [9]. The fusion of AM (a digital technology), with advanced data analytics, artificial intelligence, and machine learning techniques allows for the creation of digital twins for electrochemical systems that can simulate the manufacturing process, materials structure and properties, and device performance. Such virtual replicas can aid in design optimization and performance prediction, thereby expediting the development and validation of innovative electrochemical concepts and reducing time-to-market [10]. In addition, AM holds the potential for promoting sustainable and environmental practices in electrochemistry. Traditional subtractive manufacturing methods often result in significant material waste, energy consumption, and environmental pollution. In contrast, AM processes minimize waste by depositing materials selectively layer-by-layer, thus reducing material usage and environmental impact. This will promote the sustainability of electrochemical manufacturing and applications.

The integration of AM technologies with electrochemical applications presents its own set of challenges and limitations. Technical barriers such as material selection, process scalability, surface finish, and dimensional accuracy must be effectively solved to fully achieve the potential of AM in electrochemistry. Among various AM technologies, ink-based AM stands out due to several advantages it offers. Ink-based methods enable the production of fast, multi-material prints with fine details and high resolution. In addition, different types of inks and binders can be synthesized to achieve specific properties such as flexibility, transparency, or strength, in applications. Furthermore, ink-based AM minimizes the heat-affected zone (HAZ) compared to other AM methods that require a heat source like lasers or electron beams [11]. This reduction in the HAZ can mitigate thermal distortion, material degradation, and thermal stress, and thereby help preserve the integrity and quality of printed objects.

In this review paper, we will highlight the significance and practical applications of AM technologies for fabricating electrochemical devices, such as batteries, supercapacitors, fuel cells, and catalyst engineering. We will discuss the process-structure-property relationship across various applications, with a particular focus on ink-based AM technologies including binder jet printing (BJP), direct ink writing (DIW), and inkjet printing (IJP) methods. Based on previous research and understanding, we anticipate a surge in developing novel electrochemical devices characterized by unparalleled performance, functionality, and scalability. From advanced energy storage solutions to point-of-care diagnostics and environmental monitoring systems, the convergence of AM and electrochemistry promises to solve global challenges while unlocking new avenues for scientific exploration, economic development, and societal welfare.

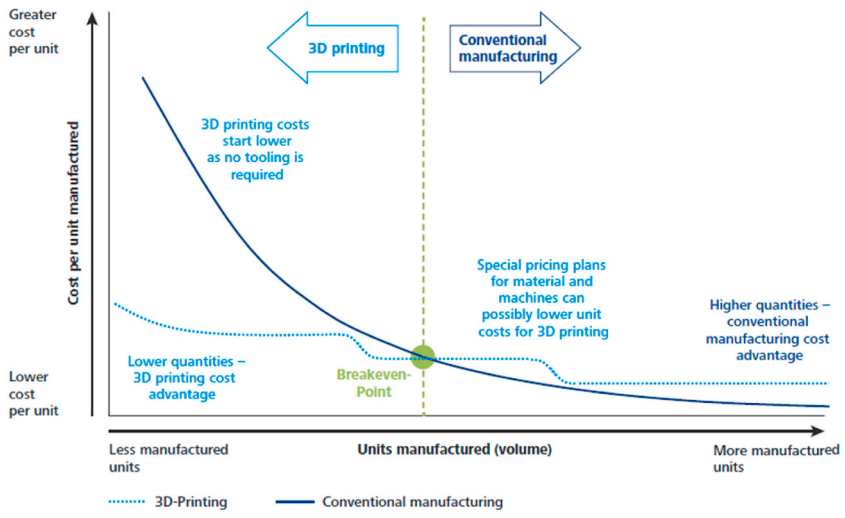

Fig. 1. Comparison between 3D-Printing and Conventional Manufacturing on Cost per Unit (Schlaepfer et al. [3]).

2. Important electrochemical applications and traditional manufacturing technologies

Traditional fabrication methods for electrodes, such as freeze-casting [12], chemical deposition [13,14], intertwining [15–17], laser irradiation [18,19], and lithography [20,21], exhibit limitations in electrochemical applications due to their complex procedures and difficulty in preparing specimens with high geometric precision. These methods often require extensive post-processing to achieve the desired surface finish, resulting in prolonged lead times. Similarly, injection molding has limitations to the production of single-material components and the intricacies of designing composite structures. Moreover, its application is often less feasible where biocompatible materials are required, limiting its application in fields like medical device manufacturing. Further, conventional manufacturing techniques, such as CNC machining, encounter limitations in the complexity of shapes they can fabricate because of the tooling constraint. Also, they tend to generate significant material waste due to their subtractive nature, which can be a concern from both an economic and environmental perspective. For instance, Fig. 2 outlines various conventional methods and materials utilized in battery fabrication processes, summarized by Zhang et al. [22]. As demonstrated, AM is preferred over traditional techniques when fabricating structures requiring high precision and complex shapes in a periodic arrangement [23].

To compare with AM techniques, a brief introduction to the traditional methods is summarized below:

Lithography encompasses various forms, including photolithography, electron beam lithography, and X-ray lithography, which are widely employed in the semiconductor and microfabrication industries. Nonetheless, inherent limitations exist. Lithography adopts a subtractive process, initiating with a solid material and subsequently removing excess material to attain the desired features. This method generates a large deal of material waste, an issue exacerbated at smaller length scales where precision is of paramount concern [24].

Freeze casting, a technique commonly used for the fabrication of porous materials, presents notable constraints in terms of design freedom. Its optimal application is observed in relatively straightforward structures, while it inadequately solves the manufacturing issues associated with geometrically complex components. In addition, the freeze-casting process is often associated with the occurrence of defects and microstructural irregularities, which may compromise the final product's quality [25].

Screen printing, as another traditional method frequently employed for pattern creation on various substrates, exhibits limitations

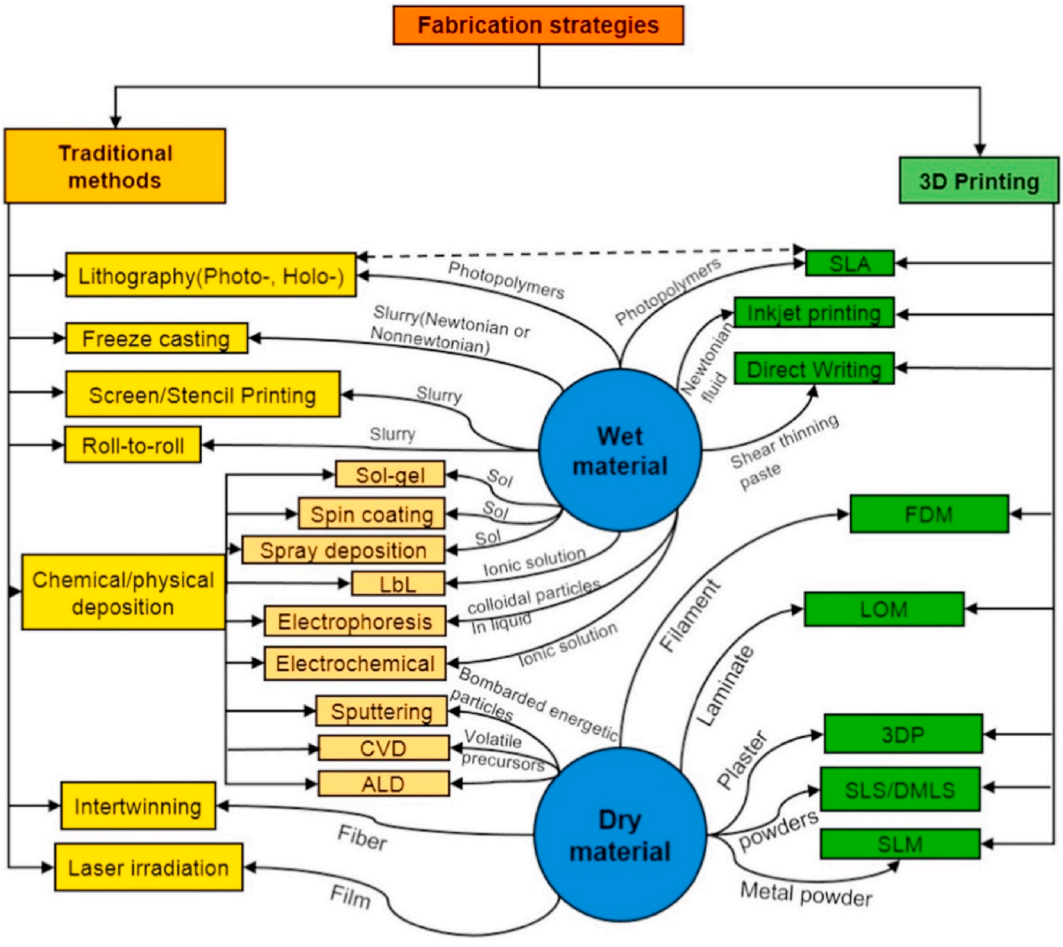

Fig. 2. A systematic map showing the various methods and materials (Zhang et al. [22]).

in scalability and versatility limitations. This issue is predominantly ascribed to the size of the stencil or screen, which constrains the scale and complexity of patterns that can be realized [26]. Furthermore, achieving high-resolution printing is a formidable challenge, thus impeding its application in fields that require exacting precision.

Roll-to-roll processing, often utilized in the production of flexible electronics and thin films, suffers from constraints about material compatibility and cost. This manufacturing method requires the deployment of specialized equipment and materials, resulting in substantial setup and maintenance expenses [27]. Furthermore, the limited array of materials deemed suitable for roll-to-roll processing restricts its adaptability to diverse applications.

Chemical and physical deposition methods, such as CVD and PVD, are extensively employed for thin film deposition and coatings. These methodologies, however, suffer from inherent constraints, especially line-of-sight deposition, that limit their efficacy in uniformly coating 3D surfaces. In addition, these techniques typically require resource-intensive conditions, including elevated temperatures or vacuums for operation [28,29].

Intertwining, which is used in the domains of textiles and wire production, primarily involves the weaving or braiding of individual strands to forge a unified structure. While suitable for applications that emphasize flexibility and structural integrity, this method regrettably lacks the precision and flexibility required for the creation of complex structures [30].

Laser irradiation, conventionally used in material cutting and welding processes, is bound by its line-of-sight operational limitation, which severely hinders its applicability for manipulating materials in 3D patterns. Moreover, laser irradiation is associated with the generation of considerable heat, which, in turn, may induce thermal distortion and material stress. AM represents an emerging technology with considerable potential for electrochemical applications, particularly in catalyst engineering and electrochemical energy storage [31,32].

2.1. Battery

Among all electrochemical systems, batteries serve as a representative platform for converting chemical energy into electric potential through redox (reduction-oxidation) reactions [33]. The operational specifics depend on the type of battery, yet the fundamental principles remain consistent. Within the complex electrochemical framework, the anode facilitates the oxidation of atoms or ions, leading to the release of electrons. These released electrons then generate an electric current in the external circuit, which can be utilized for various practical applications. Conversely, the cathode complements this process by providing a site for reduction, where atoms or ions accept electrons from the external circuit. These electrodes are spatially separated by the electrolyte, which plays a central role in mediating the migration of ions from the anode to the cathode while blocking the passage of electrons. This segregation of roles and functions among the anode, cathode, and electrolyte forms the foundational basis of battery operation across different types and applications [34,35]. As examples, the diagrams of Na^+/ion and Li_2S/Si batteries are shown in Fig. 3(A). Through this ionic

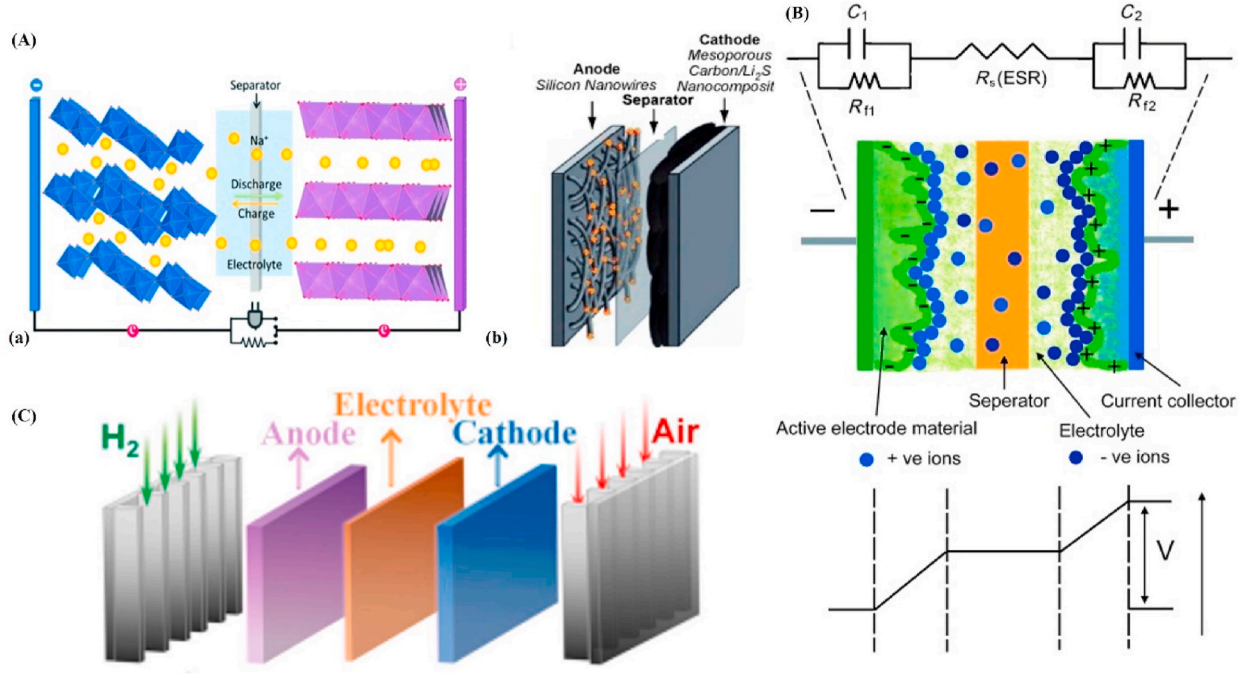

Fig. 3. (A) (a)Non-aqueous or aqueous sodium-ion battery (Kundu et al. [37]). (b) Diagram showing the structure of a Li_2S/Si battery (Yin et al. [36]).(B) Representation of a two-electrode supercapacitor cell and its resistor-capacitor equivalent circuit. (Zhang et al. [60]).(C) Representation of fuel cells. (Lu et al. [61]).

conduction, the electrolyte effectively bridges the electrical divide between the anode and cathode, thus ensuring the uninterrupted flow of charge and the consistent operation of the battery. Collectively, these configurations support the redox reactions, where the oxidation event at the anode achieves equilibrium through simultaneous reduction at the cathode. The energy from these reactions converts to the electric potential, which can be conducted through an external circuit to execute work applications [36,37]. Rechargeable batteries, with the lithium-ion variation serving as a good example, introduce more complexity through their inherently reversible electrochemical reactions. By applying an external voltage in the opposite direction, the reactions at the anode and cathode are reversed, reinstating the initial state and enabling the battery to be recharged for subsequent usage [38]. The battery operation generally requires complex chemical reactions between multiple materials. The specific chemical composition determines a battery's characteristics and its suitability for different applications [39].

Promoting the performance of batteries within electrochemistry through traditional manufacturing methods presents multifaceted challenges. Conventional manufacturing techniques, particularly those related to electrode and separator fabrication, often face limitations in achieving the precision and uniformity required for optimal battery performance [40,41]. The mass production of battery components may lead to inconsistencies in thickness, porosity, and composition, affecting overall energy density and charge-discharge efficiency. In addition, traditional manufacturing processes can be resource-intensive, generating material waste and increasing production costs. The use of heavier materials in these techniques can contribute to reduced energy density, hindering the overall efficiency of batteries. Battery production using these methods can become cost-prohibitive, limiting their commercial viability and hampering advancements in energy storage solutions [42,43]. Consequently, the solution to these challenges is essential to improve the performance, affordability, and sustainability of batteries.

2.2. Supercapacitor

Supercapacitors, also known as ultracapacitors or electric double-layer capacitors (EDLCs), are important energy storage devices. In contrast to conventional batteries, which primarily rely on chemical reactions, supercapacitors affect electrochemical processes and the establishment of electric double layers for energy storage [44]. A standard supercapacitor comprises a pair of electrodes, conventionally crafted from activated carbon, immersed within an electrolyte solution, and separated by a separator to avert electrical contact, as displayed in Fig. 3(B). When an electric potential is applied to the electrodes, a complex sequence releases positive and negative charges that accumulate on the electrode surfaces, resulting in the formation of electric double layers. These double-layers consist of ions from the electrolyte and charge carriers from the electrode material, forming a robust electrostatic attraction between them. In the charging phase, electrons migrate from the power source to one electrode, causing the buildup of an excess of negative charge on the surface of that electrode [45]. Simultaneously, the other electrode loses electrons, resulting in an excess of positive charge. This charge separation serves as the storage of electrical energy in the form of an electrostatic potential. During discharge, the stored energy is released as electrons traverse from one electrode to the other through an external circuit, supplying electrical power. Supercapacitors are known for their exceptional capability to achieve rapid charge and discharge cycles, which suit themselves to applications that require swift energy bursts, elevated power density, and extended operational lifecycles [46].

Building supercapacitors using traditional manufacturing methods, which include techniques like roll-to-roll processing [47,48] and screen printing [49], presents several multiple challenges. These processes often face limitations in the electrode design and morphology. Traditional manufacturing techniques struggle to produce complex, three-dimensional (3D) electrode structures that maximize surface area and tailor porosity for optimal charge storage and rapid charge-discharge rates [50]. The line-of-sight deposition inherent in many traditional processes, such as physical vapor deposition (PVD) and chemical vapor deposition (CVD), can hinder uniform coatings on 3D surfaces, impacting the performance of supercapacitor electrodes [51]. These limitations highlight the need for advanced manufacturing approaches, such as AM, to solve the intricate and customized requirements of supercapacitors to achieve better electrochemical performance.

2.3. Fuel cell

The working mechanism of fuel cells is based on the conversion of chemical energy from a fuel source, typically hydrogen, into electrical energy through a redox reaction. In a typical hydrogen fuel cell like the model illustrated in Fig. 3(C), hydrogen gas is introduced to the anode, where it undergoes oxidation, releasing protons (H^+) and electrons (e^-). These electrons flow through an external circuit, generating an electrical current that can be used for various applications. Simultaneously, oxygen or air is supplied at the cathode, where it accepts the migrating protons and electrons, facilitating a reduction reaction that forms water as a byproduct [52,53]. This flow of protons through an electrolyte membrane between the anode and cathode is essential to maintaining charge balance and completes the electrical circuit. The chemical energy in hydrogen fuel is transformed into the form of electrical energy with remarkable efficiency, producing only water and heat as environmentally friendly byproducts. Fuel cells offer a clean, sustainable, and high-efficiency energy conversion method, making them valuable for a range of applications, including transportation and stationary power generation [54,55].

However, traditional manufacturing techniques, such as stamping [56], machining [57], and molding [58], face challenges when fabricating fuel cells. Traditional methods often struggle to achieve the complex and precise structures required for components like catalyst-coated electrodes and proton-exchange membranes. They don't have the fine feature sizes essential for efficient catalyst distribution and cannot also provide the uniformity necessary for consistent fuel cell operation [59]. Moreover, these processes are often operated on bulkier and heavier materials, which can adversely impact energy density and system efficiency, limiting portability and compactness. Scaling up production through traditional methods can be cost-prohibitive due to the demand for heavy-duty

equipment and intensive labor. This largely impedes mass production and quick scalability, crucial for widespread fuel cell adoption, particularly in automotive and stationary power generation applications. Innovative manufacturing techniques and materials are necessary to solve these challenges and realize the full potential of fuel cells in a competitive energy landscape.

2.4. Catalyst engineering

In electrochemistry, catalysis engineering plays an important role in developing advanced materials and systems. Through tailoring the physicochemical properties of catalysts, including composition, morphology, and surface structure, researchers can control the reactions and kinetics of electrochemical processes [62,63]. This enables the optimization of key performance parameters, such as energy efficiency, stability, and durability [64–66]. Catalysis engineering also involves exploring the potential of emerging materials as high-performance electrocatalysts, including transition metal complexes [67], metal-organic frameworks [68–70], and two-dimensional materials [71]. Furthermore, the field employs computational modeling and advanced characterization techniques, such as in situ and operando spectroscopy, to achieve fundamental insights into the underlying reaction mechanisms and structure-performance relationships [72,73].

Photocatalysts, electrocatalysts, and enzymes serve as different catalyst types, accelerating chemical reactions through different mechanisms such as light absorption, electron transfer, or biological processes [74,75]. These catalysts find diverse applications in environmental remediation, renewable energy, and industrial processes, driving advancements in fields like organic synthesis, fuel cells, and biotechnology. Meanwhile, homogeneous and heterogeneous catalysts categorize catalysts based on their physical phase relationship with reactants. Homogeneous catalysts operate in the same phase, often enabling management over reaction conditions and selectivity, while heterogeneous catalysts, with their robustness and ease of separation, dominate large-scale industrial processes [76,77]. Ongoing research in all these areas aims to develop more efficient, selective, and sustainable catalytic systems to solve pressing societal challenges and drive innovation across various sectors. Catalyst engineering involves the deliberate design and optimization of electrocatalysts and control chemical reactions at the electrode-electrolyte interface, as illustrated in Fig. 4. This process integrates materials science, surface chemistry, and reaction kinetics to improve the efficiency and selectivity of electrochemical reactions, like those in fuel cells or batteries. It begins with the choice of suitable catalyst materials based on electronic conductivity and chemical stability. Then, careful control over catalyst composition, structure, and morphology is applied [78]. Tuning the surface properties and active sites with methods like doping, alloying, and nanostructuring is essential for facilitating electrochemical reactions and promoting reaction kinetics. Catalyst-support materials and electrode designs also play significant roles in providing stability and higher catalyst activity. In addition, catalyst engineering involves developing bifunctional or multifunctional catalysts to promote multiple reactions simultaneously. Through these scientific adjustments, catalyst engineering aims to maximize the potential of electrochemical systems, improving energy conversion and storage technologies while reducing costs and negative environmental impact.

Improving the performance of catalyst-engineered systems in the context of traditional manufacturing methods faces several scientific challenges. A significant issue is the limited control over the catalyst's structure, composition, and morphology, which can impact its electrocatalytic activity. Those traditional manufacturing techniques, like impregnation [79], precipitation [80], or mechanical mixing [81], often result in poor micro-level control, making it challenging to tailor catalysts for specific electrochemical reactions. In addition, these methods may produce catalysts with irregular particle sizes and distribution, leading to less efficient utilization of active sites and reduced long-term stability [82]. In addition, traditional manufacturing processes tend to be energy and resource-intensive, leading to increased production costs and environmental concerns. To overcome these challenges, there is a growing shift towards advanced manufacturing techniques, such as atomic layer deposition and electrochemical deposition, that offer superior control over catalyst structure and composition, enabling the design of more efficient and durable electrocatalysts for a range of applications in electrochemistry [83–85].

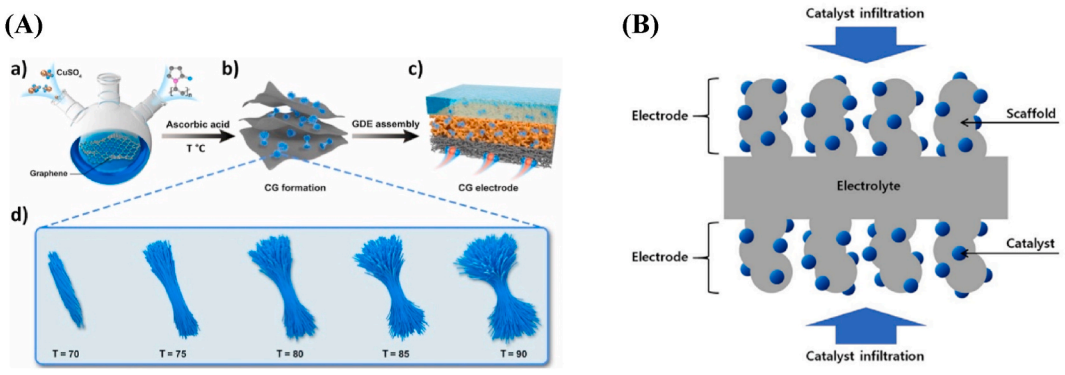

Fig. 4. (A) Scheme of Cu_2O/graphene (CG) electrodes for eCO_2RR in Cu_2O nano-flowers/graphene scaffolding structure catalyst. (Wang et al. [86]). (B) schematic diagram of the catalyst infiltration in the electrochemical scaffold. (Kwon et al. [87]).

2.5. Sensor

Electrochemical sensors are important components in a broad spectrum of applications across fields such as environmental monitoring, healthcare, industrial processes, and safety systems [88]. Their importance is affirmed as they provide essential data that help regulate environmental pollutants, manage diseases such as diabetes through blood glucose monitoring, and ensure workplace safety through the detection of toxic gases. These sensors operate based on the measurement of electrical parameters that change in response to chemical reactions at the electrode surface. Typically, they consist of a working electrode where the analyte undergoes a redox reaction, a reference electrode that stabilizes the potential, and often a counter electrode to complete the circuit in the electrochemical cell. The sensor's response is manipulated and read using techniques like amperometry or voltammetry, which involve measuring the current at a fixed potential or varying the potential, respectively, to determine the concentration of the analyte.

Despite their widespread use and critical role, traditional methods of fabricating electrochemical sensors come with significant drawbacks primarily related to complexity, cost, and scalability. Traditional fabrication techniques, such as PVD and CVD [88], require sophisticated setups involving high vacuum and precise temperature controls that are not only resource-intensive but also limit the types of materials that can be used, particularly when sensitive biological elements are involved [88]. These methods struggle with scalability and consistency across large production volumes, and they often involve hazardous chemicals and waste generation, posing environmental and health risks.

3. INK-BASED additive manufacturing technologies

There has been a lack of focus on fabrication procedures that ensure the integrity and uniformity of key components in a system, particularly when it comes to electrodes and electrolytes for electrochemical energy storage devices that are hard to manufacture using traditional methods. To solve this issue, AM technology has emerged as a potential solution. AM possesses the capability to create complex and customized geometries in rapid, energy-efficient, material-minimizing, and cost-effective manners. High-performance heat exchangers [89–91] and reactors [92,93] are among many other energy-related applications where AM has found great success. In the field of electrochemistry, AM also offers significant advantages over traditional techniques, due to its exceptional precision and adaptability in fabricating conductive electrodes with tailored shapes or compositional alterations suited for redox reactions in various fluidic systems. Also, AM can create interdigital patterns in a periodic manner, ensuring specimen uniformity and consistency [94,95]. Besides, the layer-by-layer process employed in AM allows for the deposition of thin films without sacrificing the out-of-plane uniformity of layer thickness, which is hard to solve with conventional approaches [96].

Different AM technologies offer unique features that make them suitable for a range of applications. The choice of AM technology depends on the specific requirements of the application, considering factors such as part complexity, material properties, surface finish, and post-processing considerations. Each technology has its strengths and limitations, and understanding these characteristics is essential for selecting the most suitable method for a given application [97,98]. There are primarily two major categories of AM methods: with or without heat sources.

Selective laser sintering (SLS), laser-based powder bed fusion (LPBF), directed energy deposition (DED), and fused deposition modeling (FDM) are AM techniques that involve using heat sources to fuse materials. These technologies are known for their rapid prototyping of complex geometries, high density, and excellent mechanical properties. However, these methods often rely on a restricted range of materials, primarily metallic powders or thermoplastic polymers, which may not satisfy the specialized material requirements of certain electrochemical applications. Besides, the presence of heat sources in these methods inevitably leads to a HAZ around the welding or joint area, which can result in thermal distortion, over-saturated solid solution, material degradation, or thermal stress, adversely affecting overall mechanical behavior or electrochemical performance. For instance, LPBF is a widely used method used for producing high-precision metal components. Its printing process minimizes the need for post-processing, thereby reducing waste and associated costs. Moreover, LPBF enables the creation of lightweight lattice structures, making it particularly advantageous in industries such as aerospace and automotive. During the LPBF process, however, one of the challenges arises from the rapid cooling. This rapid solidification can lead to the formation of an oversaturated solid solution in the printed part. These oversaturated regions act as scattering centers for electric currents passing through the material, which can ultimately result in a decrease in the electrochemical performance of the component. Structure defects are also present in LPBF parts, which can disrupt the flow of electrons, leading to increased electrical resistance and reduced electrochemical efficiency.

Another category of AM methods involves techniques that do not rely on heat resources for the printing process. Examples include BJP, DIW, stereolithography (SLA), IJP, and digital light processing (DLP), which require post-sintering or exposure to UV light for densification of the printed part. These methods offer the flexibility to use a wide range of materials, allowing for the selection of materials that are not only compatible with the printing method but also suitable for specific applications, including those requiring minimal thermal stress. Within this category, ink-based AM stands out as a significant group. Ink-based AM allows for the customization of binders, inks, or resins to meet different structural, or material requirements based on specific applications.

3.1. Binder jet printing

BJP is a powder-bed-based AM technology, which is capable of fabricating complex parts containing fine features without support structures. This is particularly advantageous for applications in the electrochemical field. Electrochemical systems (e.g. fuel cells) often require electrodes with finely tuned surface properties, precise mass transport characteristics, and unique designs to maximize performance. One of its most notable features is the capability to print a diverse array of materials, such as ceramics [99], metals [100],

composites [101], and polymers [102]. This is important in electrochemistry, where materials with high electrical conductivity and excellent chemical stability are prerequisites for the creation of efficient and long-lasting electrodes and electrocatalysts. BJP's versatility in accommodating a broad spectrum of materials provides a multitude of possibilities for designing customized electrochemical systems.

The working mechanism of BJP involves the selective deposition of minuscule, water-based binder droplets (typically less than 100 μm diameter) onto specific regions of a powder bed [103–105]. The binder permeates the powder layer and adheres to powder particles at locations following the cross-sectional model design, creating a green part embedded within the powder bed [106]. Subsequently, the build stage is lowered, allowing for an additional powder layer to be spread on top by a rolling recoater. Both the saturated area (where the powder is "glued" by the binder) and the unsaturated area are then covered by another layer of fresh powder [107]. This layer-by-layer process continues until the entire part is printed. After the deposition of binder droplets on each layer, a heating lamp is used to radiate the powder bed, accelerating binder curing. Following the removal of unbound powder through a depowdering process in the chamber, the fragile green part undergoes heat treatment in a furnace to fully cure the binder and then sinter the powder particles, to increase the material density and mechanical strength [108]. The aforementioned steps of the BJP process are depicted in Fig. 5. The end product, after pressureless sintering, often exhibits a porous structure. If a fully dense part is required, an infiltration process can be applied, creating a composite structure [109,110].

Various processing parameters in BJP influence the integrity, quality, and mechanical properties of the green and sintered parts. These parameters include binder viscosity, powder size distribution, curing time and temperature, recoating speed, powder shape, etc. [111,112]. Defects in samples may arise due to various factors, such as powder impurities, damage to the green part during handling [101], excessive binder saturation (bleeding) [113], or weak interlayer bonding [114].

The ability of BJP to create such components is unmatched by many other AM techniques. In addition, BJP can also create highly porous structures with ease, which is important for promoting electrochemical performance, as it enables optimized electrolyte infiltration and gas diffusion within the electrode material [115]. The high production rate offered by BJP is another factor that makes it attractive for electrochemical applications. Great scalability can be efficient in reducing the time and costs associated with the mass production of electrochemical devices. Moreover, unused powder can be readily recycled and reused for future printing. Therefore, material saving is significant in BJP compared to traditional manufacturing techniques, which is advantageous in the industry setting when using high-value feedstock [116]. Whether it is the development of advanced batteries or catalyst scaffolds, BJP offers processing flexibility for fine tailoring material performance in electrochemical devices. However, BJP falls short when it comes to multi-material build, or for applications where full-dense structures are required.

3.1.1. Fuel cells manufactured using binder jet printing

Fuel cells are an environmental-friendly electrochemical device, as they convert chemical energy stored in fuels like hydrogen or hydrocarbons directly into electricity and heat without combustion, which effectively eliminates heat or carbon dioxide as by-products [118–120]. The core components in a fuel cell include an electrolyte, anode (where fuel, often hydrogen, is supplied), and cathode (where oxygen or an oxidizing agent is provided). The electrochemical reaction at the anode splits hydrogen molecules into protons and electrons, while at the cathode, oxygen combines with the protons and electrons to produce water, generating electrical energy. This results in the flow of electrons through an external circuit, creating an electric current. Fuel cells are highly efficient, with minimal emissions of only water vapor.

As for fuel cell construction, both the anode and cathode need to have robust mechanical properties [121–123], high porosity [121,

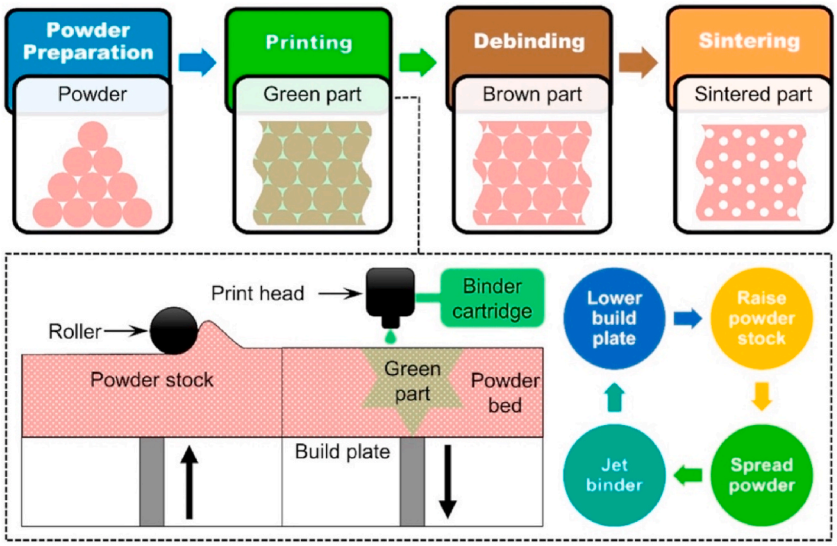

Fig. 5. Steps of BJP additive manufacturing process (Ma et al. [117]).

124], and excellent conductivity [121]. Traditional methods such as tape casting, extrusion, slurry coating, and vapor deposition are limited in their ability to control electrode porosity, which is important for increasing the inner surface area [125–129]. AM has been employed for fuel cell fabrication because it offers shape design flexibility, broad material selection, and printing pattern convenience. With improved designs and materials, AM fuel cells exhibit better performance than those manufactured using traditional approaches [121,124,130]. There are different types of fuel cells, such as Proton Exchange Membrane Fuel Cells (PEMFC), Solid Oxide Fuel Cells (SOFC), Molten Carbonate Fuel Cells (MCFC), and Alkaline Fuel Cells (AFC), each suited for different applications such as stationary power generation, transportation (e.g., hydrogen fuel cell vehicles), and portable power sources [131,132]. Information on a few typical fuel cell types including materials, working temperature, and application are summarized in Table 1.

Only a few teams reported the fabrication of SOFC using BJP. In a SOFC, the fuel is transferred to the anode, and an oxidant is fed to the cathode to produce an electric current. A higher operating temperature allows for increased efficiency and flexibility in fuel choice [145–147]. Manogharan et al. reported a new approach for producing SOFC using BJP technology, which takes advantage of hydrogen as the fuel source [148]. The results presented in Fig. 6 demonstrate the key innovation of controlling porosity, surface area, and gas diffusion characteristics in various layers of solid oxide fuel cells (SOFCs), including the Ni-YSZ anode (nickel oxide–yttria-stabilized zirconia), LSM-2 cathode (lanthanum strontium manganite (20 %)), and oxygen ion-conducting YSZ electrolyte layers (yttria-stabilized zirconia (8 % Y)). This control allows for the optimization of conductivity while minimizing adverse impacts on other properties.

Researchers emphasize the importance of porosity in the electrode layers of SOFCs, which function as gas diffusion electrodes. The desired porosity facilitates the penetration of reactive gases into the electrodes, establishing contact with the electrode/electrolyte interface and enabling efficient gas-solid reactions and electron/ion transport at the tri-phase boundary. To assess the effects of BJP on SOFC properties, researchers analyzed the fuel cell material composition using SEM with EDS. This analysis helps understand how the material composition influences fuel cell performance, essential for optimizing functionality and durability.

Furthermore, the evaluation of SOFC performance through electrical discharge and permeability tests provides insights into how the fabricated cells operate under different conditions. These tests contribute to establishing the relationship between the structural characteristics of the fuel cell, its electrical output, and gas flow properties, improving our understanding of SOFC behavior and performance.

While BJP offers advantages such as customization of complex structures and material compatibility, it also suffers from drawbacks including poor dimensional accuracy and structure integrity, which can limit the construction of intricate fuel cell components. Surface roughness resulting from the printing process may also impact the integrity of solid oxide fuel cell (SOFC) components and could require additional post-processing steps for smoothing. Furthermore, ensuring clean removal of binder residue is crucial for achieving high performance in fuel cell applications. Achieving uniform material distribution and homogeneity throughout the printed parts can be challenging with BJP, potentially leading to variations in material composition or density within SOFC components. These inconsistencies may translate to performance and property variations across the fuel cell. Hence, the suitability of BJP for fuel cell fabrication depends on specific application needs, with its effectiveness varying based on the structural and material requirements of the fuel cell components being produced.

3.1.2. Catalysis scaffolds manufactured using binder jet printing

The primary purpose of catalysis engineering is to improve the efficiency and selectivity of electrocatalytic reactions, promoting sustainable energy conversion and storage technologies [149–151]. Catalysis engineering has explored the application of AM for heterogeneous catalysis systems. Specifically for BJP, the impact of ink-powder wettability, powder flowability, and powder size distribution on the structure, mechanical properties, and performance of catalysts has been widely studied. Also, the as-printed green parts, after depowdering, are typical of low density and fragile, which requires post-sintering in a high-temperature furnace. However, higher sintering temperatures result in reduced porosity by forming more necking areas [152–154]. Consequently, the structure of catalyst scaffolds is significantly influenced by BJP parameters, sintering temperature and duration [155], designed channel size [155], pore size distribution [156], surface roughness [157], and other factors. Researchers have investigated catalyst monoliths with varying channel geometries, such as spherical, cylindrical, and honeycomb structures, each exhibiting distinct overall catalytic properties and performances [158]. Summary of the different catalysts printed using BJP, as presented in Table 2, including catalyst type, uniformity, features, etc.

Aluminum oxide (Al_2O_3) is a commonly employed heterogeneous catalyst scaffold, owing to its good mechanical properties and

Table 1
Categories of fuel cells.

Fuel Cell Types	Materials	Working Temperature	Application	Reference
Direct Methanol Fuel Cell (DMFC)	Electrolyte: polymer Fuel: liquid methanol	60–90 °C	Portable Electronic Devices	[133–135]
Protonic Ceramic Fuel Cell (PCFC)	Electrolyte: barium ceramic oxide Fuel: hydrocarbons	500–700 °C	Combined Heat and Power (CHP) Systems	[136–138]
Molten Carbonate Fuel Cell (MCFC)	Electrolyte: $LiAlO_2$ matrix with molten carbonate salt mixtures Fuel: various fossil fuels	600–700 °C	Stationary Power Generation	[139–141]
Solid Oxide Fuel Cell (SOFC)	Electrolyte: oxide ion-conducting ceramic Fuel: natural gas or propane	800–1000 °C	Large-scale Industrial Power	[142–144]

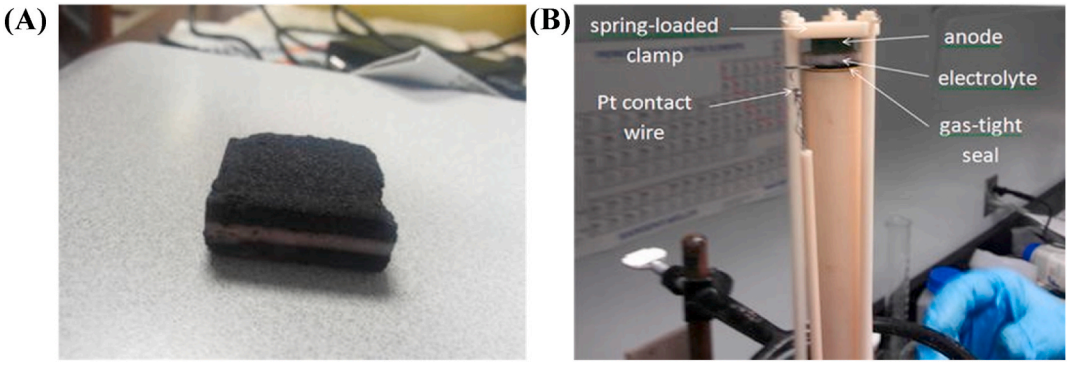

Fig. 6. (A) Sample of a SOFC fabricated using BJP. (B) Cell mounted on the ProboStat support tube (Manogharan et al. [148]).

suitability for large-scale production [162,163]. Catalytic reactions within these scaffolds are facilitated by their high porosity and extensive internal surface areas. Reactants in fluids can move effectively through pores of varying dimensions, where active catalyst nuclei reside [163]. Bui et al. [160] fabricated η- and γ- Al_2O_3 from boehmite and bayerite for use in heterogeneous catalysis through low-temperature calcination and ambient boehmite slurry drip infiltration. This BJP fabrication strategy effectively stabilizes the Al_2O_3 framework, ensuring robustness and high porosity while maintaining a surface area of 223 m^2/g and 80 % open porosity. The structure of Al_2O_3 supports is characterized by their porosity and pore size distribution, which are important for their effectiveness in heterogeneous catalysis. Porosity influences the available surface area for catalytic reactions, as shown in Fig. 7. The void structure of printed parts evolves during the manufacturing process, transitioning from a fine and even void structure in the green part to a coarser and more porous structure in the infiltrated parts. Structural analysis using micro-computed tomography (μCT) allows for the evaluation of shrinkage in the printed parts, providing valuable information on dimensional changes during manufacturing. The property of crushing strength is evaluated at different stages of the manufacturing process, from green parts to infiltrated parts. The crushing strength significantly improves through the infiltration process, emphasizing the importance of post-processing steps in fortifying mechanical properties. Porosity directly impacts the catalytic performance of Al_2O_3 supports. The distribution of pore sizes and effective porosity play critical roles in determining suitability for heterogeneous catalysis. Properties such as mass increase and density are monitored throughout the manufacturing process, offering insights into material characteristics and structural changes during printing and post-processing. These analyses contribute to a comprehensive understanding of how the manufacturing process affects the physical and mechanical properties of Al_2O_3 supports, ultimately influencing their performance in catalytic applications.

In another study, Bui et al. demonstrated BJP Pt/Al_2O_3 catalysts employed in the dehydrogenation of perhydro-dibenzyl toluene (18H-DBT) [161], part of the research is shown in Fig. 8. BJP produces parts that are especially porous with a rough surface texture, often exhibiting a parallel line pattern indicative of the print head movement during printing. Compared to DIW at lower calcination temperatures, BJP generates shapes with higher specific surface areas due to increased porosity. It also demonstrates higher meso- and macro-porosity, facilitating faster penetration during impregnation processes and deeper metal deposition within the catalyst structure. Therefore, BJP-printed Pt/Al_2O_3 catalysts have a slightly higher 18H-DBT dehydrogenation rate. BJP is particularly suited for generating complex channel geometries, which can increase fluid flow within catalyst structures, potentially improving mass transfer and reaction rates. These attributes make BJP a favorable AM method for producing catalyst structures with tailored properties suitable for various applications in catalysis and beyond.

Photocatalysis is one of the catalysts that accelerate chemical reactions by absorbing photons (light) to initiate reactions. This phenomenon finds application in various fields such as water purification, air purification, and self-cleaning surfaces. Titanium dioxide (TiO_2) stands out as a widely used photocatalyst in environmental and industrial applications.

In a recent study by Liu et al. [159], shown in Fig. 9, specimens were printed layer-by-layer with a specific binder-to-cement ratio, affecting the bonding between layers and the overall structural integrity. Curing conditions, including relative humidity and temperature, are essential for the hydration process and mechanical property development. The addition of TiO_2 particles of different sizes influences the overall microstructure, porosity, density, and interfacial characteristics of the cement-based material. Variations in curing conditions during manufacturing can lead to structural variations within printed specimens, impacting their mechanical

Table 2
Different catalysts printed using BJP.

Types	Materials	Uniformity	Feature	Applications	Reference
Photocatalysts	1. TiO_2	heterogeneous	1. accelerate chemical reactions through the absorption of photons (light) to initiate the reaction.	1. Water/air purification, industry, and self-cleaning surfaces	[159]
Electrocatalysts	1. Pt/Al_2O_3	heterogeneous	1, increase the rate of electrochemical reactions, typically occurring at electrodes. 2. facilitate the transfer of electrons during redox reactions, either by promoting oxidation or reduction.	1. Electrolysis, and fuel cells industry	[160, 161]

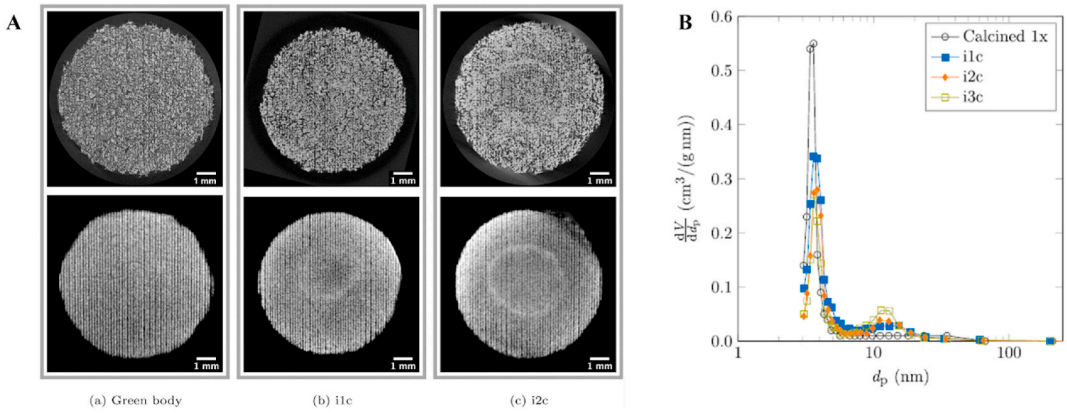

Fig. 7. (A) Cross-sectional views of μCT scans of printed cylinders perpendicular to the z-axis of the green body, i1c and i2c samples. (B) Pore size distribution of one to three times infiltrated samples compared to the debinded (calcined) part (Bui et al. [160]).

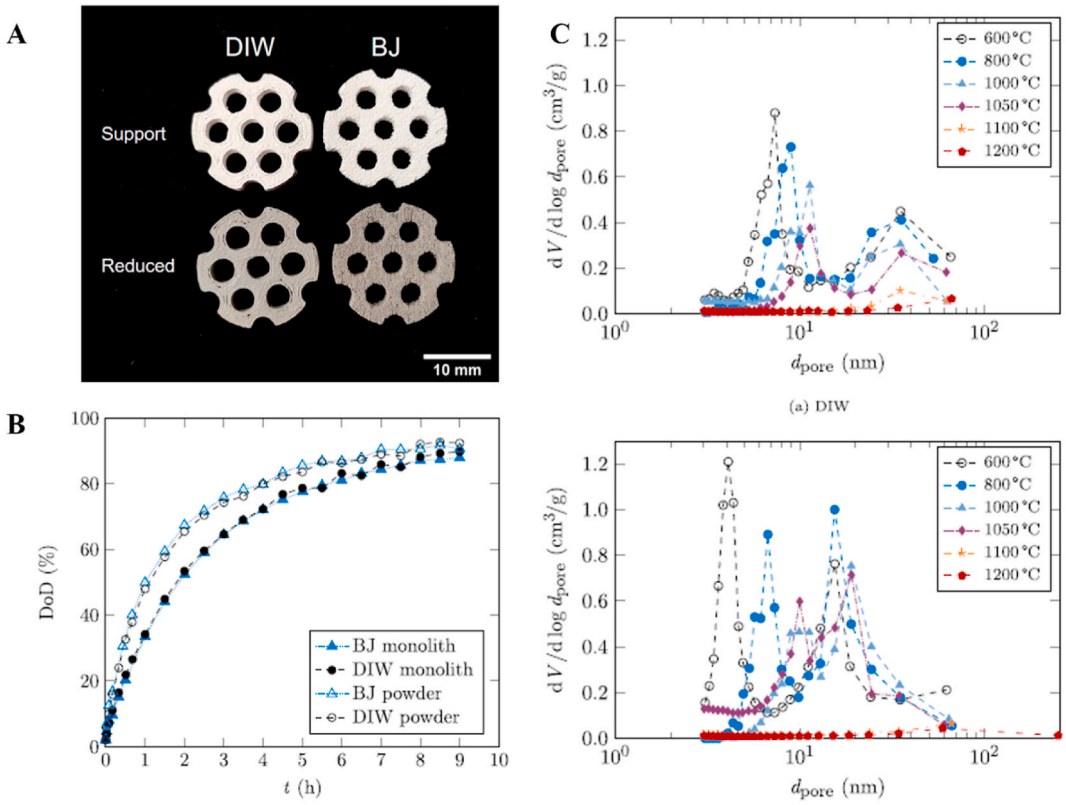

Fig. 8. (A) Photos of monolithic alumina supports (first row) and reduced Pt/Al_2O_3 catalysts (second row) fabricated by DIW and BJP. (B) 18H-DBT dehydrogenation over BJ and DIW printed Pt/Al_2O_3 catalysts in a semi-batch reactor setup, tested with monolithic and powder catalysts, respectively. (C) Pore size distribution of the 3D printed alumina supports from (a) DIW and (b) BJ calcined at varying calcination temperatures (Bui et al. [161]).

properties.

The mechanical properties of cement-based materials, including compressive strength, flexural strength, and durability, are influenced by particle addition and the AM process. Mechanical stress increases with rising relative humidity, likely due to raised moisture that facilitates hydration reactions in cement-based materials, leading to more hydration products. However, in the early stages (under 7 days), no significant increase in strength is observed because binder dilution weakens layer bonds. Large-sized TiO_2 particles exhibit superior mechanical properties. These particles provide sufficient surface area for nucleating hydration products, thereby amplifying nucleation effects, precipitating hydration products, and accelerating cement hydration. Moreover, they fill voids

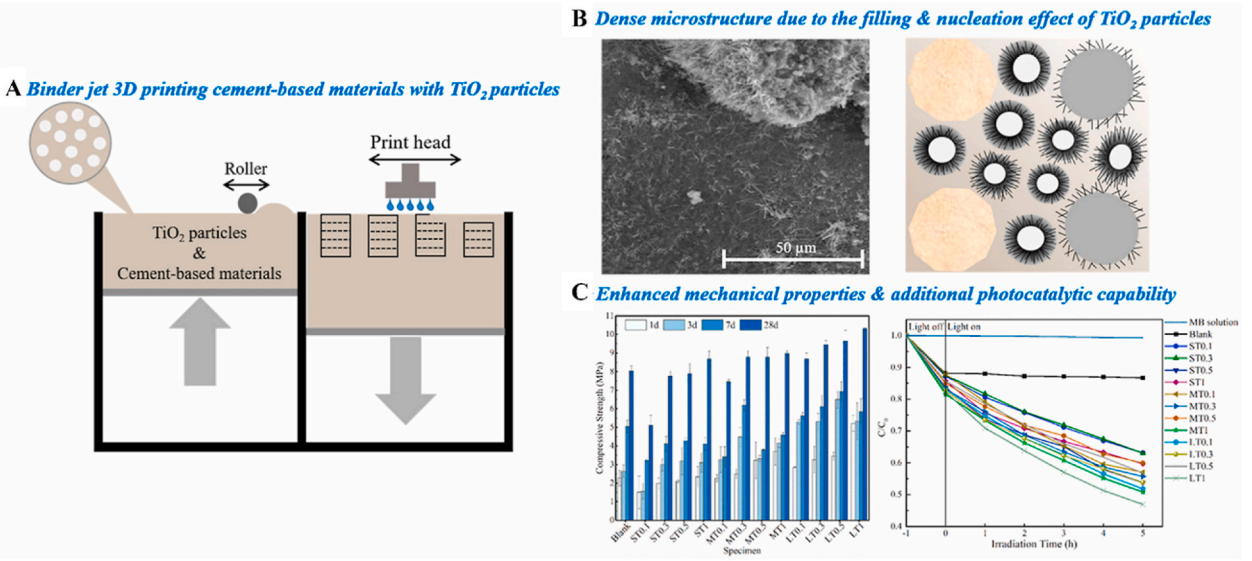

Fig. 9. (A) Schematic of TiO_2-reinforced cement-based materials in BJP. (B) surface of specimens and schematic diagram of the filling and nucleation effect of differently sized TiO_2 particles. (C) Compressive strength and photocatalytic effect of the specimen (Liu et al. [159]).

in specimens, resulting in a denser microstructure and increased compressive strength.

The photocatalytic activity of printed specimens was evaluated by measuring changes in methylene blue (MB) concentration using ultraviolet–visible (UV–vis) spectroscopy. Small-sized powder exhibits no significant photocatalytic effect as it tends to be wrapped in hydration products, preventing direct contact with pollutants. Conversely, large powder size demonstrates the best photocatalytic performance.

3.2. Direct ink writing and inkjet printing

DIW and IJP are 2 a.m. techniques that offer unique capabilities for fabricating complex structures with tailored properties. Unlike other ink-based AM technologies, such as BJP, DIW and IJP operate without the need for a powder bed. Instead, they utilize ink or paste materials directly deposited onto a substrate. However, both techniques require support structures to maintain the integrity of the printed objects during fabrication to prevent deformation or collapse of overhanging features during printing.

DIW involves the extrusion of a continuous flow of ink or paste material through a nozzle, which is precisely controlled to deposit material layer by layer according to a computer-generated design. This method enables the creation of complex geometries with high resolution and excellent control over material placement. In addition, DIW allows for the incorporation of multiple materials or

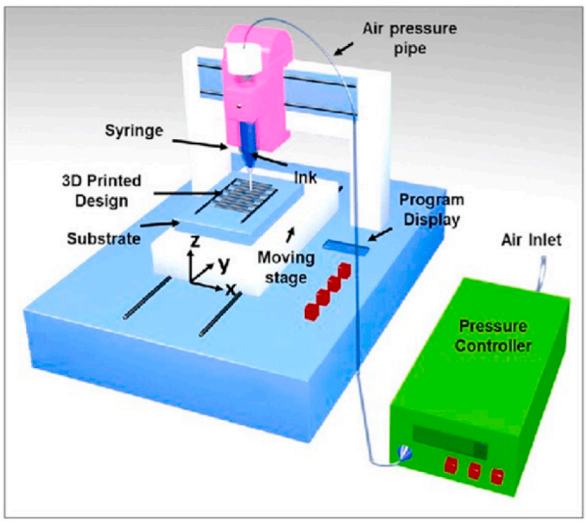

Fig. 10. Schematic illustration of DIW AM method (Ovhal et al. [166]).

functional additives within the ink, offering control over material properties and functionality [164]. The working principle of DIW is illustrated in Fig. 10. The selection of ink is important, with options including polymers, resin-bound ceramics, metals, composites, or even biological materials, each tailored to the desired properties and application. The ink is prepared and loaded into a syringe or cartridge, then passed through a controllable nozzle. By adjusting the nozzle diameter and temperature, the viscosity and flow rate of the ink are fine-tuned, which can influence the extrusion rate and layer precision. As with all AM techniques, DIW prints 3D objects layer by layer, as the tool path precisely follows the sliced CAD model, depositing ink onto the build platform along the X and Y axes. After all layers are laid down, bonding and solidification follow, which are induced by either curing with UV light or heat for polymers, or sintering at high temperatures for ceramics and metals [165]. If the design incorporates overhangs or complex features, support structures are required to prevent the collapsing issue during printing, which will be removed in the end. Post-processing steps are application-specific and may include further curing, sintering, or additional treatments to improve material properties and structural integrity.

The advantages of DIW are significant. One of its most compelling strengths is its capability to construct highly intricate structures that would be exceptionally difficult to achieve using traditional manufacturing methods. This makes DIW well-suited for fabricating customized, specialized components, such as complex lattices or personalized medical implants. Moreover, DIW extends its compatibility with a wide range of materials, including polymers, ceramics, metals, and composites. This diversity in materials enables the integration of multiple materials and functionalities within a single print.

Another advantage of DIW is its high resolution. Depending on factors such as nozzle size and ink rheological properties, DIW can produce parts with very fine features, allowing for the management of the geometry of the printed structures. This high-resolution capability opens up opportunities for manufacturing detailed components across various industries [167]. Moreover, DIW offers the advantage of reduced material waste. By depositing material only where it is needed, DIW minimizes excess material usage, leading to a reduction in environmental footprint and cost savings [168].

While DIW offers numerous advantages, it also presents certain challenges. These include speed limitations, post-processing requirements, material constraints, high equipment costs, the necessity for support structures, and the resolution-speed trade-off. However, ongoing research and development (R&D) endeavors are actively facing these limitations, across diverse industries such as aerospace, healthcare, electronics, and art. By solving existing challenges and pushing the boundaries of innovation, DIW has the potential to contribute to efficiency and innovation in various sectors. With advancements in materials, processes, and equipment, DIW can be used to unlock new possibilities and pave the way for transformative advancements in manufacturing and beyond.

Another AM technology, IJP utilizes droplets of ink ejected from a printhead onto a substrate in a controlled manner to build up the desired structure. This technique offers rapid printing speeds and high spatial resolution, making it well-suited for applications requiring fine features or complex patterns. Furthermore, IJP allows for the deposition of a wide range of materials, including conductive inks, biomaterials, and functional polymers, enabling the fabrication of diverse functional components. The working principle of IJP involves the precise deposition of ink droplets onto a substrate to create patterns, as shown in Fig. 11(A) [169]. This process begins with the digital image or pattern being rasterized into small dots, with each dot corresponding to a specific position on the substrate. Ink droplets are then expelled from the nozzles in the printhead in response to electrical signals from the control electronics, forming the desired image or pattern on the substrate. After printing, the ink must be allowed to dry or undergo curing under the lamp to adhere to the substrate properly, ensuring that the printed pattern remains intact and durable over time. There are two types of printheads for IJP: piezoelectric inkjet printheads and continuous inkjet printheads, as shown in Fig. 11(B) [170]. Piezoelectric printheads are renowned for their precise droplet control, leveraging piezoelectric crystals that undergo shape changes in

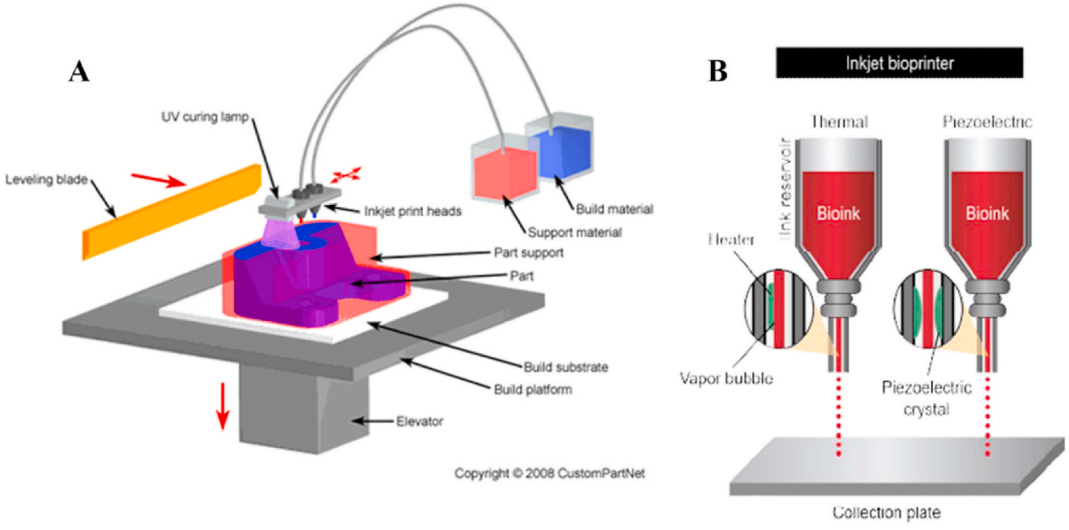

Fig. 11. (A) Schematic illustration of IJP AM method (Waheed et al. [169]) (B) Schematic of Piezoelectric inkjet printheads and Continuous inkjet printheads (Seyedmahmoud et al. [170]).

response to an applied electric current. This deformation results in pressure pulses, which expel ink droplets from the printhead nozzles. These printheads can eject droplets of varying sizes, facilitating high-resolution printing, and enabling the deposition of a broad spectrum of ink formulations. On the other hand, continuous inkjet printheads operate by continuously ejecting ink droplets from the printhead. Ink is propelled through a small nozzle at elevated pressure and heat, generating a continuous stream of droplets. Each droplet is then subject to an electrostatic charge, allowing for their deflection or precise directing onto the substrate. These printheads are particularly well-suited for high-speed printing applications.

IJP offers several advantages, including high-speed printing capabilities, droplet placement, and the ability to produce high-resolution structures with fine details [171]. It allows for printing on a wide range of substrates, from paper and textiles to plastics and metals, making it suitable for various applications across industries. In addition, IJP is a non-contact printing method, reducing the risk of damage to delicate substrates, and enabling printing on uneven or curved surfaces. However, IJP also has its limitations. Routine maintenance, such as printhead cleaning and alignment, is necessary to ensure optimal print quality and prevent clogging or other issues that can affect performance.

In summary, DIW and IJP stand out as suitable methods for printing electrochemical devices due to their material compatibility, customization, and scalability. DIW and IJP allow for the creation of complex electrode geometries essential for optimizing electrochemical performance. Their compatibility with a wide array of conductive and functional ink formulations enables the integration of diverse materials within the same device, facilitating the fabrication of complex electrode structures tailored to specific electrochemical applications. Moreover, the rapid prototyping and iterative capabilities of DIW and IJP are invaluable for R&D efforts improving device performance and exploring new applications. As scalable manufacturing methods, DIW and IJP hold promise for the mass production of electrochemical devices, essential for commercialization across industries.

3.2.1. Batteries manufactured using direct ink writing and inkjet printing

In electrochemistry made by AM, batteries are often manufactured using DIW and IJP techniques, while BJP is less frequently employed due to several scientific and practical factors. Each of these printing methods has its distinct advantages and disadvantages. However, the primary limitation of BJP lies in its single feedstock, making it less suitable for multi-material battery components. This is an essential requirement in battery fabrication for creating diverse and tailored battery structures.

DIW is known for its customization capabilities, making it possible to design hierarchical structures in batteries, ultimately improving their performance. In contrast to BJP, DIW offers multi-material printing, allowing for the creation of complex battery structures with various components. The inks with higher viscosity can be beneficial for diverse battery material options [172–174]. Oftentimes, DIW is utilized to create tailor-made electrodes and solid-state electrolytes with better performance. The technique permits

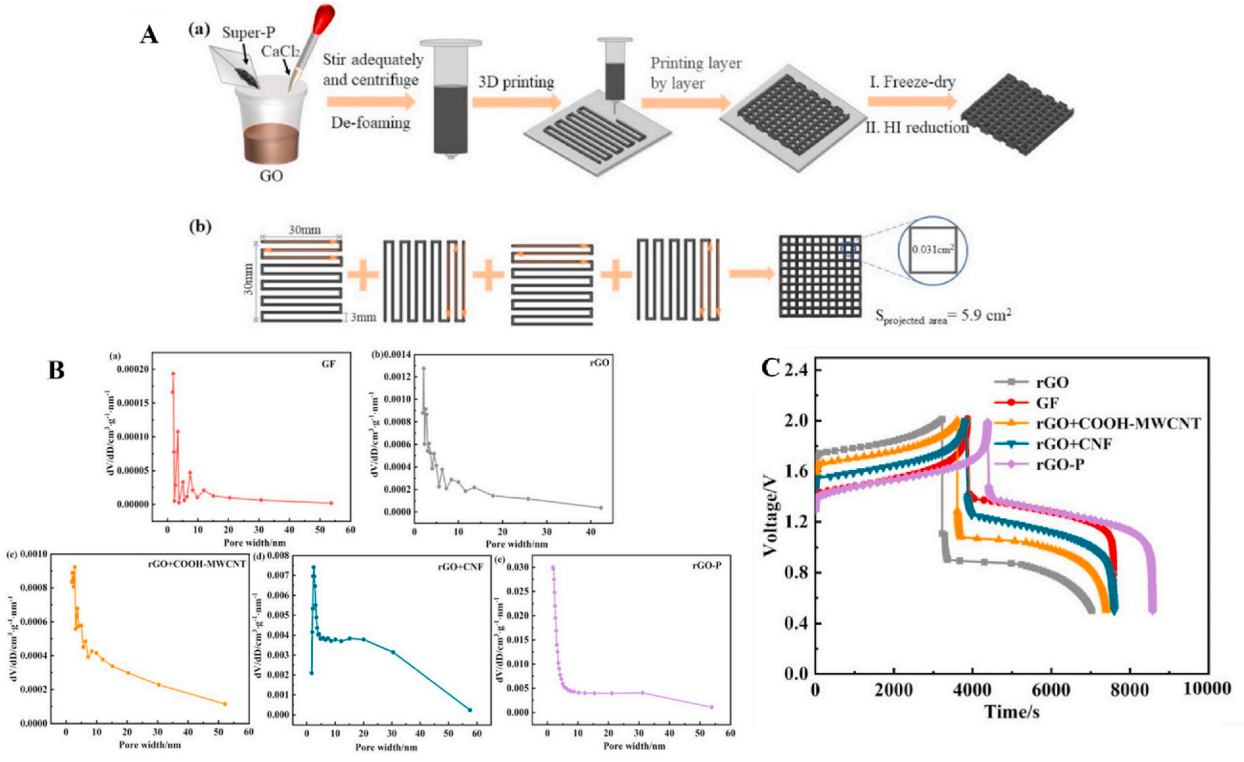

Fig. 12. (A) Schematic illustration of the preparation process (a) and printing path (b) of 3D printed graphene aerogel. (B) The pore size distribution curves of GF (a), rGO (b), rGO + COOH-MWCNT (c), rGO + CNF (d) and rGO-P (e).(C) Comparison of charging and discharging curves of different electrodes at the current density of 80 mA cm $^{-2}$ (Li et al. [173]).

the fine-tuning of parameters such as porosity, surface area, and material composition, which directly influence the electrochemical performance of batteries [173,175]. This degree of control over material properties ultimately results in improvements in energy and power density and cycling stability [176,177]. Furthermore, the layer-by-layer assembly process of DIW facilitates the incorporation of multiple materials and functional components within a single battery structure. This approach promotes the development of innovative architectures and groundbreaking electrochemical systems, including all-solid-state batteries, flexible batteries, and 3D micro batteries [173,174].

As shown in Fig. 12, Li et al. have demonstrated the utilization of DIW for precise deposition of graphene oxide (GO) ink in fabricating graphene/Super-P aerogel composite electrodes for vanadium redox flow batteries (VRFBs) [173]. The choice of printing path and the concentration of GO ink are essential parameters influencing the structure and overall properties of the final electrode. DIW presents design flexibility, enabling the creation of complex and tailored electrode structures with high precision. Moreover, the DIW process facilitates the development of a hierarchical porous structure in the graphene aerogel composite electrode, with its

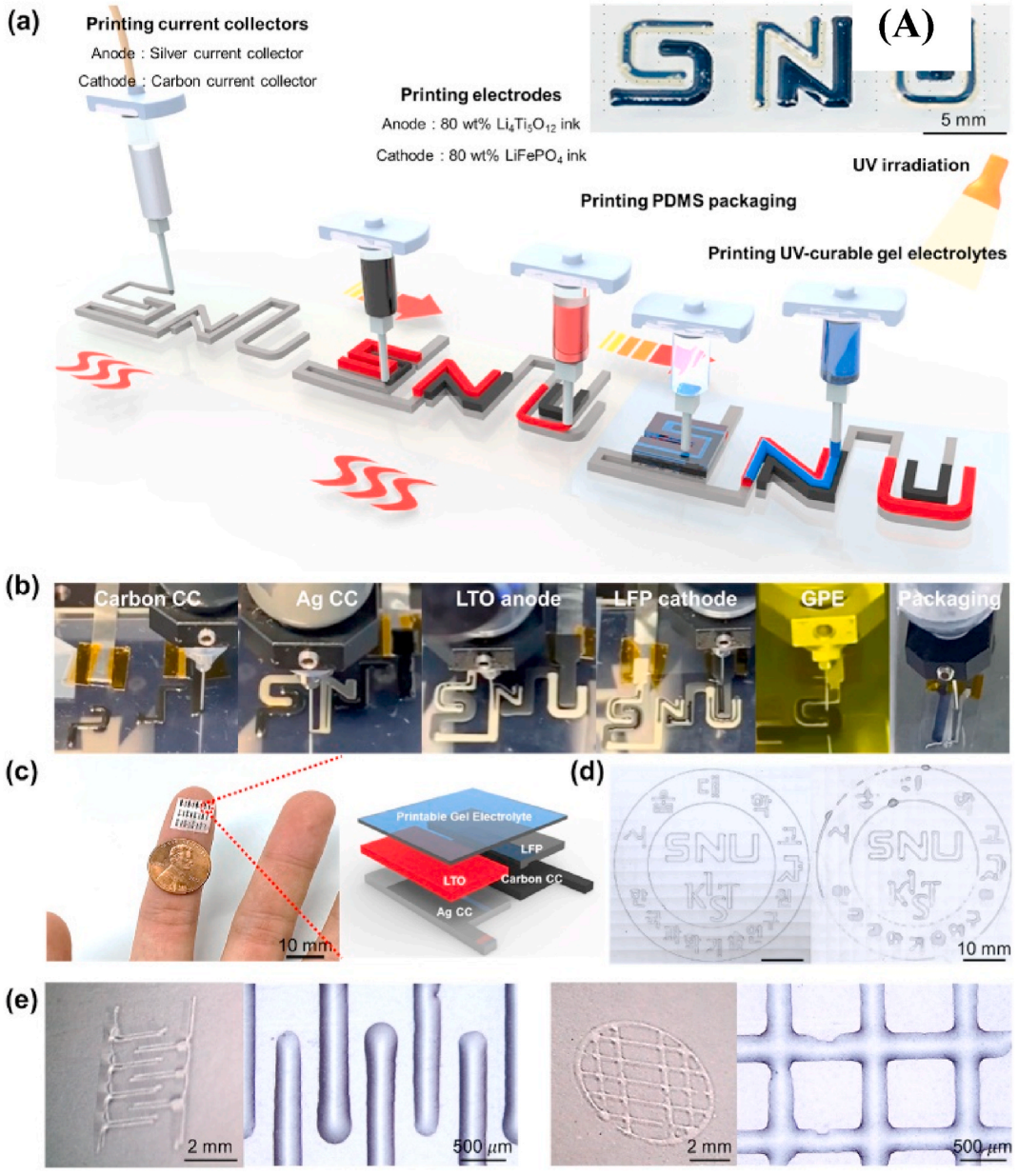

Fig. 13. (A) AM quasi-solid-state lithium-ion batteries (LIBs) with printable gel polymer electrolytes (GPEs). (a) Fabrication procedure. (b) Photos of all DIW printing steps. (c) Photo of DIW printed micro-battery arrays and the structure of single LIB. (d) Optical microscopy images of printed letters with AM GPE (left) and conventional gel composite electrolyte (right). (e) High-resolution patterns of the AM GPE: interdigitated structure (Left), circle-grid structure (right) (Bae et al. [178]).

architecture precisely controllable by adjusting the printing path and ink concentration.

During the printing, DIW enables the fabrication of both macro and microscale features in the graphene aerogel, thereby augmenting its performance in VRFB applications. The resultant hierarchical porous structure offers a high specific surface area, thereby improving the performance of the electrode, which exhibits a superior discharge capacity of 848.4 mA h at a current density of 80 mA cm^{-2}. Furthermore, the graphene aerogel composite electrode demonstrates exceptional mechanical strength, attributed to the controlled architecture achieved through DIW. This electrode also showcases high chemical stability and conductivity, important properties for efficient energy storage in VRFBs. Among the various compositions, GO-P exhibits the most promising cell performance owing to the introduction of the Super-P component, which facilitates conductivity and provides additional active sites for reaction. In addition, the rGO-P, featuring a porous structure at both macro- and microscales, facilitates the mass transfer of reactants and products in the vanadium redox reaction, thereby mitigating concentration polarization.

Micro batteries can be integrated directly onto a device substrate using a simple yet versatile direct write dispenser printing process. This is further highlighted by Bae et al.'s work [178], which demonstrates the creation of customized quasi-solid-state lithium-ion batteries with a high capacity of 120 mAh/g. This innovation paves the way for multifunctional applications such as miniaturized wearable biomedical devices and soft robots. The printing process and electrochemical characterization are shown in Fig. 13.

Utilizing DIW as the manufacturing process enables the creation of intricate 3D structures layer-by-layer, eliminating the need for lithographic or shadow masks. This approach offers unparalleled customization for Li-ion batteries on platforms of arbitrary shapes, providing great design flexibility and scalability. Rheological optimization of printable inks for these components ensures the production of well-defined, high-resolution patterns without dispersion or aggregation issues.

By incorporating printable Gel Polymer Electrolytes (GPEs) comprising Li-ion electrolytes and UV-curable polymers, the printed batteries exhibit thixotropic fluid behaviors and appropriate viscosity for high-throughput and mechanically robust electrolyte layers. These electrolytes offer excellent ion transport properties, crucial for performance. They ensure uniform and well-defined deposition of electrolytes, thereby amplifying the overall efficiency of the battery fabrication process. GPEs also uplift the overall conductivity of the electrolyte, leading to improved battery performance in terms of charge/discharge rates and stability over cycling. Moreover, their incorporation adds mechanical robustness to the printed batteries, maintaining the integrity of the battery components during operation. This mitigates the risk of delamination or structural failure, ensuring long-term stability and reliability.

In contrast to DIW, another ink-based AM technology frequently utilized for printing batteries is IJP. Unlike DIW, where ink is extruded continuously from the nozzle from a print head onto a surface. Meanwhile, IJP differs from BJP as the ink injected contains the feedstock material rather than serving solely as a binder. Consequently, while IJP shares common practices with both BJP and DIW, it represents a distinct AM technique in practice. Furthermore, its capability for multi-material printing allows for the seamless integration of diverse materials into various battery components, such as electrodes and electrolytes, tailored precisely for specific electrochemical processes.

Lithium iron phosphate is considered more environmentally benign than other lithium-based batteries like those using cobalt or nickel. The extraction and processing of iron are generally less damaging to the environment, and the material is less toxic. Gu et al. conducted a study on the preparation of water-soluble $LiFePO_4$ inks with varying initial pH values, followed by IJP of electrodes on current collectors like aluminum foil and carbon nanotube paper [179]. This IJP process enables precise deposition of the cathode material, presenting advantages in scalability, cost-effectiveness, and customization, as shown in Fig. 14.

The structure of the printed electrodes plays an important role in determining the performance of lithium-ion batteries. Insights into impurities generated as the pH stabilizes can impact the structural properties of the electrodes, as revealed by results from inductively coupled plasma (ICP) and X-ray diffraction (XRD). In addition, SEM images illustrate the morphology and composition of the printed electrodes with different current collectors. Properties like electrical conductivity, particle size, and terahertz transmission

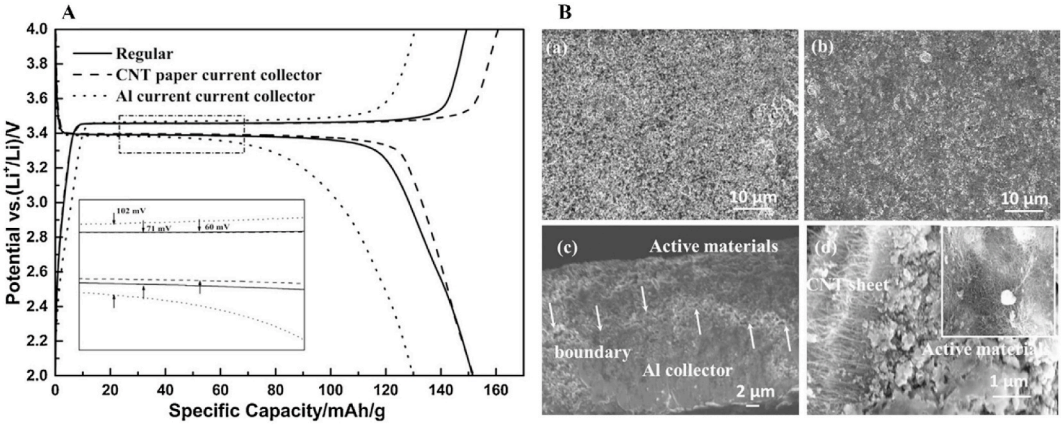

Fig. 14. (A) The charge/discharge curves of the battery made by tape casting and printed electrodes at 0.1C current rates between 2.0 and 4.0 V at 25 °C. (B) (a) SEM image of Surface and (c) side section of printed electrode with Al current collector; (b) surface and (d) side section of printed electrode with CNT current collector (Gu et al. [179]).

intensity of the inkjet-printed cathodes significantly influence battery performance. The study indicates that impurities affect the electrical conductivity of $LiFePO_4$, while changes in ion concentration based on initial pH values influence particle size and terahertz transmission intensity.

The electrochemical reactivity of the ink is evaluated through cyclic voltammetry, elucidating the impact of composition changes on the stability and performance of the printed electrode. Non-electrochemically active impurities in the $LiFePO_4$ ink are found to decrease electrical conductivity, emphasizing the importance of understanding impurity effects for optimizing cathode performance. Changes in ion concentration, influenced by the initial pH values of the inks, lead to variations in particle size of the $LiFePO_4$ material, attributed to different binder adsorption mechanisms on the carbon surface, emphasizing the importance of ink formulation in controlling electrode properties. Utilizing IJP technology, electrodes are fabricated on diverse current collectors, such as aluminum foil and carbon nanotube (CNT) paper, offering customized designs and scalable production of lithium-ion battery components.

In another study, Delannoy et al. utilized IJP to fabricate porous composite $LiFePO_4$ electrodes, leveraging its precise and scalable deposition method for creating complex structures with high resolution [180]. The study, as illustrated in Fig. 15, focused on optimizing ink formulations and printing parameters to achieve electrodes with improved electrochemical properties, essential for high-power micro battery applications. The rheological properties of the inks were extensively investigated to ensure compatibility with piezoelectric IJP specifications. Low molecular weight poly-acrylic-*co*-maleic acid (PAMA) copolymer was employed as a binder and dispersant, refining ink rheology and stability. The optimized ink formulation, with the right balance of active materials, conductive additives, and binders, resulted in electrodes exhibiting high power output and cyclability.

The researchers controlled the deposition process by adjusting parameters such as nozzle voltage, jetting frequency, and dwell time to achieve the desired electrode structure. PAMA copolymer, with its low viscosity at high shear rates, facilitated smooth ink flow through the nozzles during ejection, ensuring precise and uniform printing onto the substrate. Moreover, the stability of PAMA at rest prevented issues like flocculation and nozzle clogging, ensuring consistent ink performance over time. The porous structure of the composite $LiFePO_4$ electrodes significantly influenced their electrochemical performance. IJP allowed the changing of electrode morphology, porosity, and thickness, promoting ion diffusion and electron transport. SEM analysis provided insights into the microscale morphology of the printed electrodes, highlighting their thin and porous structures.

The IJP electrodes underwent thorough electrochemical testing, demonstrating high specific capacities of 80 $mAh.g^{-1}$, low polarization of 100 mV, and stable cycling performance under different conditions. The large surface area of the electrode facilitated electrochemical reactions, improving charge/discharge rates and overall power output, making them suitable for high-power micro

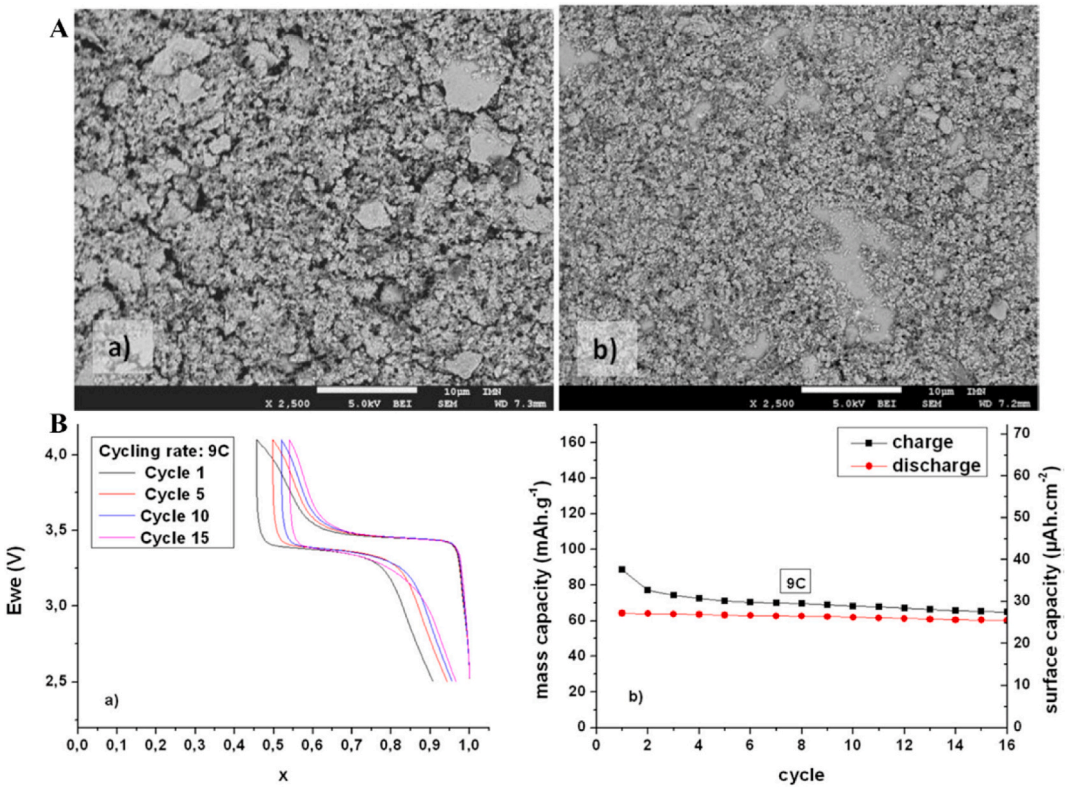

Fig. 15. (A) SEM pictures of a) tape-cast electrode and b) printed electrode. (B) Galvanostatic cycling, at a 9C rate, of LiFePO4 porous composite printed electrode (from ink 3) in ES assembled in Swagelok cell. a) Intercalated lithium ratio (x) versus potential; b) charge (black square) and discharge (red circle) mass capacity (Delannoy et al. [180]).

battery applications.

$LiCoO_2$ is known for its high energy density, which is an essential attribute for rechargeable batteries used in portable electronic devices like smartphones, laptops, and cameras. Lee et al. investigated the use of IJP for fabricating $LiCoO_2$ electrodes with surface-modified carbon black (CB), aiming to improve the dispersion properties of the ink important for achieving uniform and well-structured electrodes [181]. The research is shown in Fig. 16. Surface-modified CB particles were introduced to promote dispersibility, leading to a more homogeneous distribution around each $LiCoO_2$ particle, resulting in a denser and more uniform microstructure. The study extensively analyzed the microstructure of the IJP electrodes, evaluating parameters like pore size distribution, surface roughness, and morphology. Surface modification significantly reduced large-size pores above 40 nm in the electrodes, particularly pronounced in those treated with UV/ozone–TETA. This reduction contributed to a more compact and uniform electrode structure, potentially boosting battery performance and stability.

The surface modification also led to electrodes with lower surface roughness compared to those using as-received CB, indicating a smoother and more uniform electrode surface conducive to improved electrical contact between CB and $LiCoO_2$ nanoparticles, thereby strengthening electrochemical performance. High-resolution transmission electron microscopy (HRTEM) and SEM were employed to observe CB morphology and investigate microstructural changes in the electrodes. In addition, Barrett-Joyner-Halenda (BJH) pore size distribution analysis highlighted the impact of surface modification on electrode structure.

The IJP-printed $LiCoO_2$ electrodes with surface-modified CB exhibited improved electrochemical properties, including higher initial discharge capacities, attributed to the modified microstructure and better CB dispersion. Better dispersion properties resulted in improved electrical contact between CB and $LiCoO_2$, leading to higher specific discharge capacities and overall electrochemical performance. Electrochemical evaluations, including area-specific impedance (ASI) measurements, provided insights into how microstructural differences influenced by CB dispersion affected battery performance. By strategically modifying the CB surface and optimizing its dispersion, the study promotes electrode properties, such as capacity, cycling stability, and overall efficiency, for lithium-ion battery applications.

Huang et al. also employed IJP to fabricate $LiCoO_2$ thin film electrodes, a process that involves precise deposition of $LiCoO_2$ ink onto a substrate [182]. The dispersion technique utilized ultrasonic dispersion with a surfactant to ensure uniform dispersion of $LiCoO_2$ particles in the ink, critical for achieving a homogeneous thin film, as illustrated in Fig. 17. The $LiCoO_2$ powder synthesized through a modified sol-gel method allowed the controlled formation of $LiCoO_2$ nanoparticles, which were subsequently used to prepare the ink. Optimization of printing parameters is important for achieving desired properties, as they control the thickness and uniformity of the thin film, which can impact its electrochemical performance. Crystallographic analysis via XRD revealed well-defined diffraction

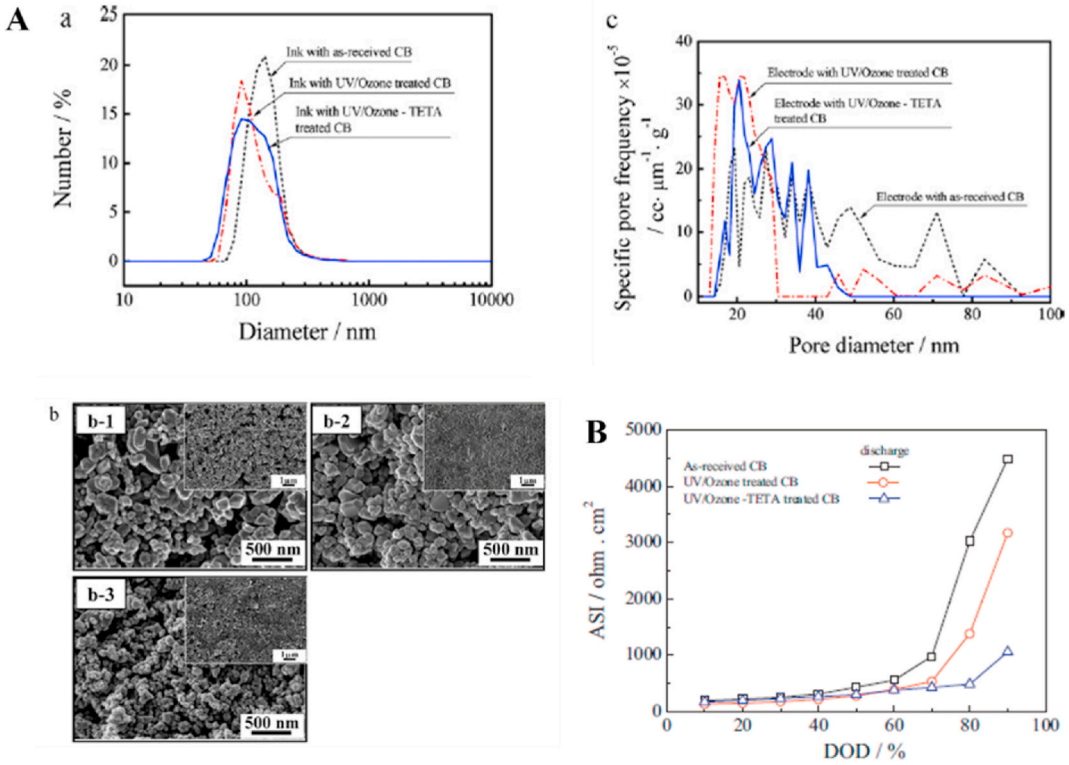

Fig. 16. (A) (a) Particle size distribution of $LiCoO_2$ ink prepared with CBs before and after surface modification, (b) SEM images, (c) Barrett–Joyner–Halenda(BJH) pore size distributions of the electrodes prepared with CBs before and after surface modification. (B) charge–discharge curves as a function of cycle number(Lee et al. [181]).

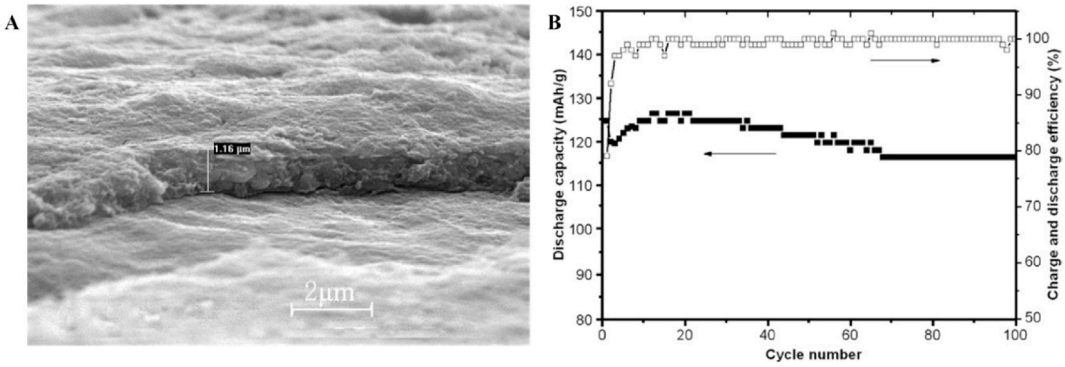

Fig. 17. (A) SEM image of the cross-section of $LiCoO_2$ thin film electrode. (B) Cycling performance, charge, and discharge efficiency of $LiCoO_2$ thin film electrode at charge-discharge current density of 192 μA/cm2(Huang et al. [182]).

peaks, confirming the crystalline nature and specific crystal faces of the $LiCoO_2$ thin film. Surface morphology observed through SEM showed pores and cracks that enlarge the electrode/electrolyte contact area, affecting electrochemical behavior. Cross-section imaging provided insights into the thickness of the film and $LiCoO_2$ material amount.

The electrochemical performance of the $LiCoO_2$ thin film electrodes exhibited excellent stability over multiple charge-discharge cycles, with high discharge capacities, near 100 % charge-discharge efficiencies, and minimal capacity loss after cycling. The electrodes displayed excellent discharge performance even at high discharge rates, indicating efficient Li + intercalation/deintercalation abilities. Redox peaks observed in voltammograms reflected the efficient Li + intercalation/deintercalation. The maintenance of good crystallinity during charge-discharge processes and the stability of the film structure contributed to the excellent cycling performance. Stable discharge capacities and near 100 % charge-discharge efficiencies were observed across different charge and discharge rates, highlighting the stability of the electrode over multiple cycles. After 100 charge-discharge cycles at a discharge current density of 192 $\mu A/cm^2$, the $LiCoO_2$ thin film electrode exhibited minimal capacity loss, retaining its capacity and performance over extended cycling. This stability was attributed to the persistence of good crystallinity and high structural stability of the thin film electrode.

Milroy et al. utilized IJP to manufacture lithium-sulfur batteries and achieved high capacities, as demonstrated in Fig. 18. The structure of IJP lithium-sulfur micro-cathodes significantly impacted their performance. The study discussed the arrangement of

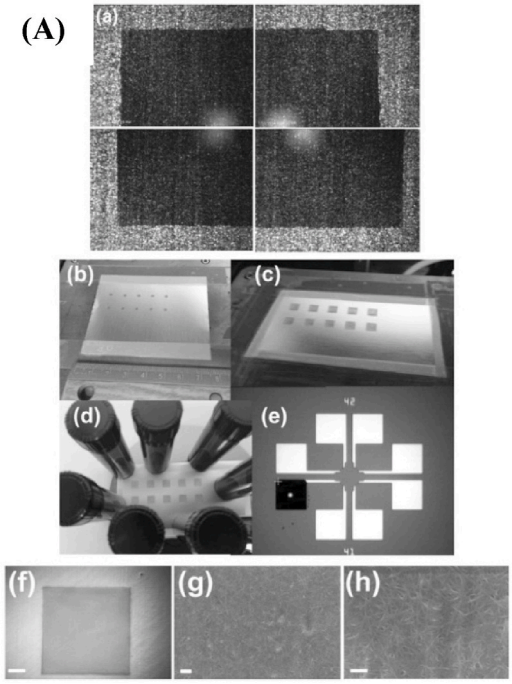

Fig. 18. (A)IJP battery (a) Optical image of printed 2 × 2 mm SWNT ink square (black area) on aluminum foil (gray area). (b) 2 × 2 mm, (c) 5 × 5 cm squares, and (d) electrode arrays during the annealing process. I Freshly printed 200 μm square on a Pt-patterned, SiO_2-capped silicon wafer. (f–h) SEM images of printed electrodes after annealing (Milroy et al. [183]).

single-wall carbon nanotubes (SWNTs) and sulfur within the cathode, emphasizing inter-SWNT connectivity and the importance of electrode pore spaces. SWNTs served as a conductive matrix for straight-chain sulfur, facilitating electrochemical reactions during charge and discharge cycles, thus advancing cathode performance. SWNTs infused with sulfur acted as an integrated current collector/active material composite, simplifying the cathode structure and improving energy storage efficiency. The electrode internal structure was also investigated, with a focus on SWNT interstice size and arrangement. SWNTs infused with sulfur exhibited pseudocapacitive characteristics, indicating a combination of capacitive and faradaic processes that potentially charge storage and cycling stability. The electronically conductive straight-chain sulfur within SWNTs contributed to stable discharge capacity.

IJP cathodes exhibited stable performance at different rates, up to 1C, indicating good rate capability and capacity retention. By controlling ink formulation and printing parameters, micro-cathode properties such as capacity, cycling stability, and rate performance could be optimized for specific applications. The IJP cathodes demonstrated pseudocapacitive characteristics, avoiding soluble polysulfide formation, and contributing to performance and stability. Utilizing SWNTs infused with straight-chain sulfur aimed to sharpen lithium-sulfur cathode performance and stability. The initial discharge capacity was approximately 800 mAh g^{-1} sulfur, with a stable discharge capacity of around 700 mAh g^{-1} sulfur after 100 cycles at a C/2 rate, indicating good capacity retention. The cathodes exhibited consistent cycle performance, suggesting long-term reliability.

3.2.2. *Supercapacitors manufactured using direct ink writing and inkjet printing*

Supercapacitors, also known as ultracapacitors or electrochemical capacitors, showcase high power density, fast charge and discharge capabilities, and long-lasting cycle life [184]. These properties make them suitable as intermediate energy storage options between traditional capacitors and batteries. The electrodes, such as graphene, carbon nanotube, or conductive polymers are responsible for storing energy during the charging process and releasing it during discharge. The electrolyte serves as a medium that facilitates ion transportation between the electrodes during charge-discharge cycles [185,186]. In AM supercapacitors, the electrolyte can be an aqueous or non-aqueous solution, ionic liquid, or solid-state material. The selection of an appropriate electrolyte significantly influences the voltage window, conductivity, and overall performance of a supercapacitor [185,186]. And the separator material must exhibit excellent chemical stability, mechanical strength, and high porosity to maintain an optimal balance between safety and performance [187].

DIW offers the advantages of good material compatibility and multi-material printing capability. Supercapacitors typically require different materials for electrodes, electrolytes, and separators, all of which can be precisely deposited using DIW. In addition, DIW allows for high levels of customization and precision, making it suitable for building complex supercapacitor structures. MXenes offer higher volumetric and areal capacitance than conventional materials such as carbon, conducting polymers, or transition metal oxides [188–190]. Li et al. researched the process-structure-property relationship in DIW of programmable micro-supercapacitors, employing

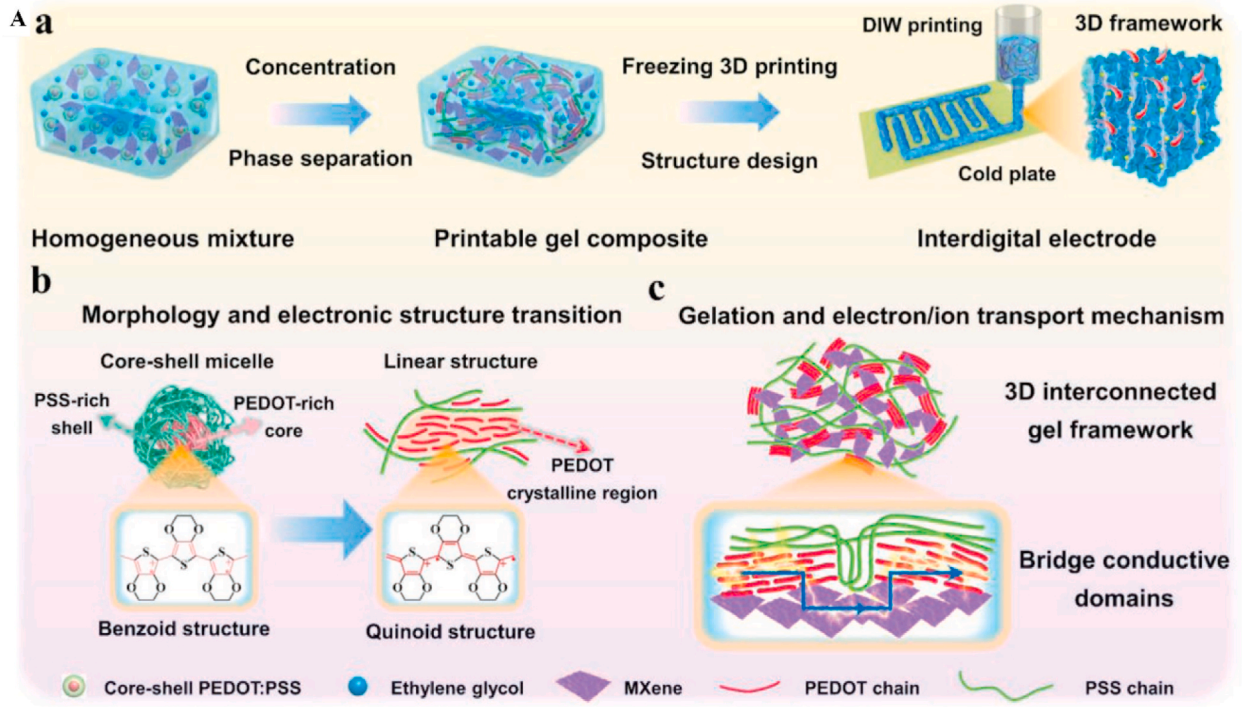

Fig. 19. (A)AM of PME gel composites for MSC devices. (a) Schematic illustration of the preparation of the 3D printable PME gel composite inks and interdigital electrodes. (b) Morphology and electronic structure transition of PEDOT: PSS within the PME gel composites. (c) Schematic illustration of the gelation and electron/ion transport enhancement mechanism for the PME gel composites (Li et al. [191]).

MXene-regulating conducting polymer inks [191]. The DIW printing process involved layer-by-layer fabrication of micro-supercapacitors using a specialized ink comprising PEDOT: PSS, MXene nanosheets, and ethylene glycol (EG). This method offered good control over material deposition, facilitating the creation of complex and customizable micro-supercapacitor designs. The rheological properties of the ink, characterized by shear-thinning behavior, were important in ensuring printability and shape fidelity during the DIW process. The results are shown in Fig. 19.

The composite gel ink, comprising a homogeneous blend of PEDOT: PSS, MXene nanosheets, and EG, formed a stable and conductive network for energy storage. XRD patterns elucidate the crystal structures and molecular interactions within the gel composite, revealing successful MXene nanosheet exfoliation and extending π–π coupling of PEDOT chains. The optimized morphology and electronic structure of the gel composite, attributed to the interlayer spacing of MXene nanosheets and self-intercalation of PEDOT chains into MXene, contribute significantly to its properties.

Improvement in charge transport kinetics and redox activity were observed within the gel composite, leading to improved performance of micro-supercapacitors. Transitioning from polarons to bipolarons in PEDOT chains resulted in heightened conductivity and electrochemical activity, further augmenting energy storage capabilities. The capacitance, rate performance, power density, and cycling stability of micro-supercapacitors were influenced by the unique structure and properties of the PEDOT: PSS/MXene composite gel. In particular, increasing electrode thickness during layer-by-layer manufacturing improved capacitance and energy density by enabling the deposition of high-mass-loading electrodes, improving energy storage capacity, optimizing charge transport pathways, and ensuring electrode stability. These benefits collectively contributed to the development of advanced energy storage solutions with superior performance characteristics and application versatility.

Wu et al. present a comprehensive study on the fabrication, structure, properties, and applications of poly(3,4-ethylenedioxythiophene): poly(styrenesulfonate) (PEDOT: PSS)-based flexible micro-supercapacitors utilizing DIW technology [192]. To optimize the process, the rheological properties of PEDOT: PSS inks were fine-tuned, ensuring suitable viscosity and shear-thinning behavior for stable printing. The fabrication steps included ink preparation, printing of interdigitated electrodes, and deposition of ion gel electrolytes, showcasing the efficiency of DIW printing in micro-supercapacitor production, as illustrated in Fig. 20.

Characterization techniques such as optical microscopy and field-emission SEM were employed to analyze the morphology and structure of the printed electrodes. The resulting interdigitated electrode structures exhibited high conductivity, serving as both current collectors and active materials in the micro-supercapacitors. Remarkably, the PEDOT: PSS-based micro-supercapacitors demonstrated impressive areal capacitance and outstanding cycle stability, retaining 87 % of their initial capacitance after 10,000 charge-discharge cycles. In addition, these devices exhibited excellent bending stability, which could maintain capacitance under various bending conditions, highlighting their suitability for flexible and wearable electronics applications.

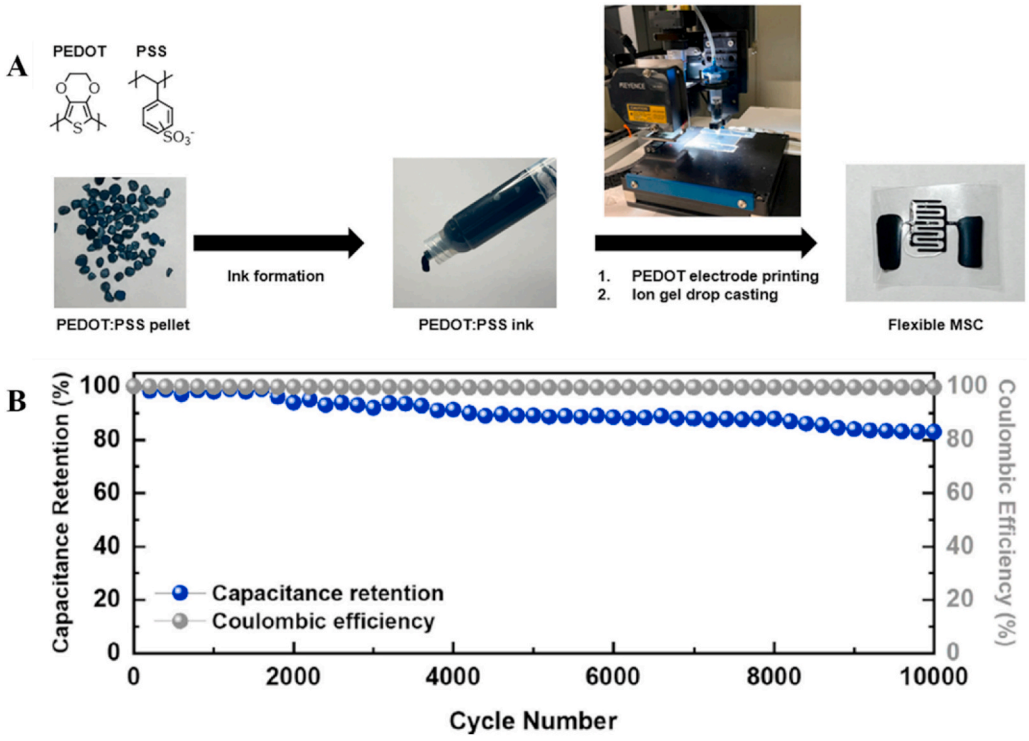

Fig. 20. (A) schematic of the fabrication of PEDOT: PSS-based MSCs. (B) Charge/discharge cycle stability of the PEDOT: PSS-based MSC at a current density of 100 μA/cm^2 (Wu et al. [192]).

Furthermore, the ability to customize output voltage and capacitance by connecting multiple micro-supercapacitors in series or parallel configurations emphasized meeting specific power requirements. This, coupled with their fast charging and discharging capabilities, makes them promising candidates for various energy storage applications. Moreover, the simplicity, cost-effectiveness, and compatibility with flexible substrates make DIW an attractive manufacturing method for the scalable production of these high-performance energy storage devices, facilitating their integration into next-generation electronics and systems. In addition, the PEDOT: PSS-based micro-supercapacitors exhibited high areal capacitance, reaching 2005 μF/cm^2 at a current density of 10 μA/cm^2. This remarkable capacitance further solidifies their potential for delivering robust and efficient energy storage solutions in a wide range of applications.

Zhang et al. have successfully demonstrated the fabrication of all-printed solid-state micro-supercapacitors with a multilayer structure using a multi-material DIW technique [193]. The DIW technique, involving precise extrusion of electrode ink to construct complex 3D structures layer by layer, relies on the stability, shear-thinning behavior, and homogeneity of the ink. Ink formulation and rheological properties are important in ensuring successful AM. The results are shown in Fig. 21. The composite electrode ink, comprising polypyrrole nanotubes (PPyNT), GO, and conductive carbon black, forms an interconnected network structure through π-π stacking interactions, boosting ion transport and stability during charge-discharge cycles. The shear-thinning behavior of the ink was attributed to the orientable nanostructures of the electrode materials, which influenced the viscosity, modulus, and active material loading. Characterization of the PPCANT nanotubes reveals their distinctive morphology, exhibiting a well-defined co-axial structure with a polypyrrole core and a polyaniline shell. Microscopy imaging confirms this structure, with the polyaniline shell having a wall thickness of approximately 20 nm.

The interaction between the polypyrrole core and polyaniline shell was crucial for enhancing the electrochemical properties of the PPCANT nanotubes. This co-axial structure facilitated rapid ion transport and stability during charge-discharge cycles, contributing to improved electrochemical performance. The multi-layer structure of printed MSCs reduced equivalent series resistance (ESR) and better electronic transmission efficiency. Incorporating pseudo-capacitive materials like PPyNT and GO significantly improved the capacitance and energy density, with stable ink formulation and AM contributing to improved cycle performance. Furthermore, the conductive nature of both polypyrrole and polyaniline components increased the conductivity of the PPCANT nanotubes, essential for efficient charge transfer in supercapacitor applications. This conductivity, combined with the unique co-axial structure, resulted in fortified electrochemical performance, including high capacitance and stability during cycling. Moreover, boasting a calculated highest energy density of 19.6 mWh/cm^3 at a power density of 0.91 mW/cm^3, it demonstrated a remarkable energy storage capacity relative to its volume.

Tung et al. utilized a DIW printing process to deposit graphene and cobalt ferrite nanoparticles ink onto a substrate, as shown in Fig. 22 [194]. They optimized parameters such as printing speed and temperature to facilitate efficient printing. The ink formulation was tailored to ensure evaporation efficiency, enabling continuous and multi-layer printing while preserving substrate adhesion. The morphology and composition of the GP-CoFe hybrid nanomaterial were characterized using SEM and TEM, revealing the layered structure of graphene and the spherical shape of cobalt ferrite nanoparticles. SEM with EDX mapping analyzed the material distribution on the supercapacitor electrodes. Graphene sheets were functionalized with SDS and dispersed in water, then combined with hydrophilic cobalt ferrite nanoparticles and a PVA binder to form stable colloidal dispersions of GP-CoFe hybrid ink. This ink exhibited uniform distribution for efficient electrode fabrication.

Regarding electrode performance, microwave-treated electrodes showed specific capacitance values of 233.3 F/g in CV tests and 304 F/g in GCD tests, indicative of efficient electrical energy storage. Electrodes displayed good electrochemical durability, with 94.7 % capacitance retention after 16,000 charge-discharge cycles. Microwave treatment increased electrical conductivity and porosity,

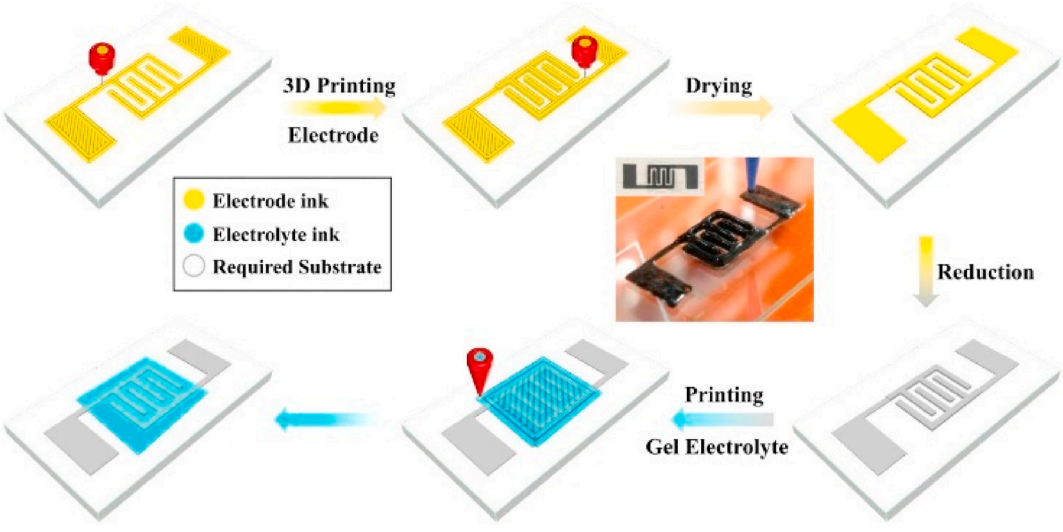

Fig. 21. Schematic illustration of the fabrication process of all-printed micro-supercapacitors with different layers (Zhang et al. [193]).

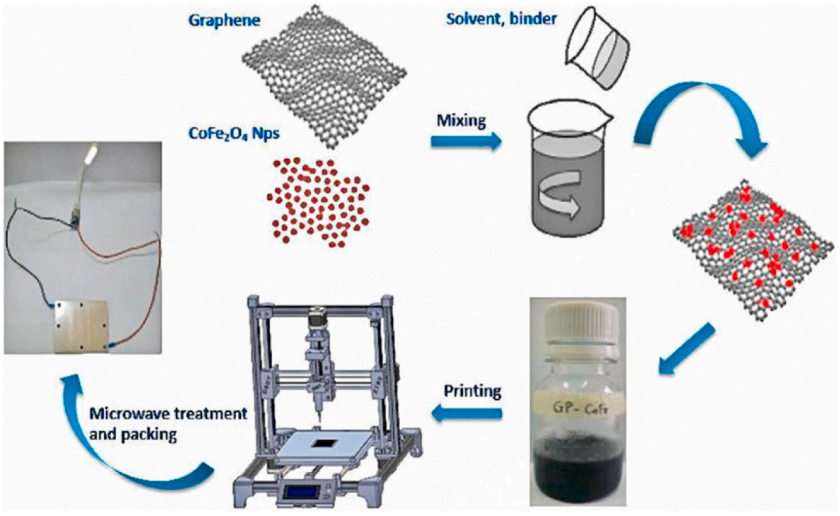

Fig. 22. Schematic of Printing Process for DIW of the Proposed Supercapacitor(Tung et al. [194]).

and thereby promoted efficient charge transfer and ion diffusion. The DIW process coupled with microwave treatment provided an efficient method for producing high-performance supercapacitor electrodes, showcasing the potential of GP-CoFe hybrid ink in energy storage applications.

Chen et al. fabricated supercapacitors using a DIW process involving several critical steps [195]. Firstly, they developed an ink formula tailored for DIW. This ink formulation needed compatibility with supercapacitor materials like single-wall carbon nanotubes (SW-CNT) for electrodes, poly(vinyl alcohol) (PVA)-based gel electrolyte, and silicone for packaging and sealing. In addition, the ink required specific rheological properties optimized for DIW, ensuring controlled flow and deposition onto the substrate. Once the ink formulation was developed, the printing setup was configured using a DIW testbed. This setup enabled layer-by-layer fabrication of the supercapacitors, with control over ink dispensing rates, platform temperature, and movement. During the printing process, SW-CNT ink was deposited for electrodes, PVA electrolyte was dispensed, and silicone was used for packaging and sealing. This multifunctional

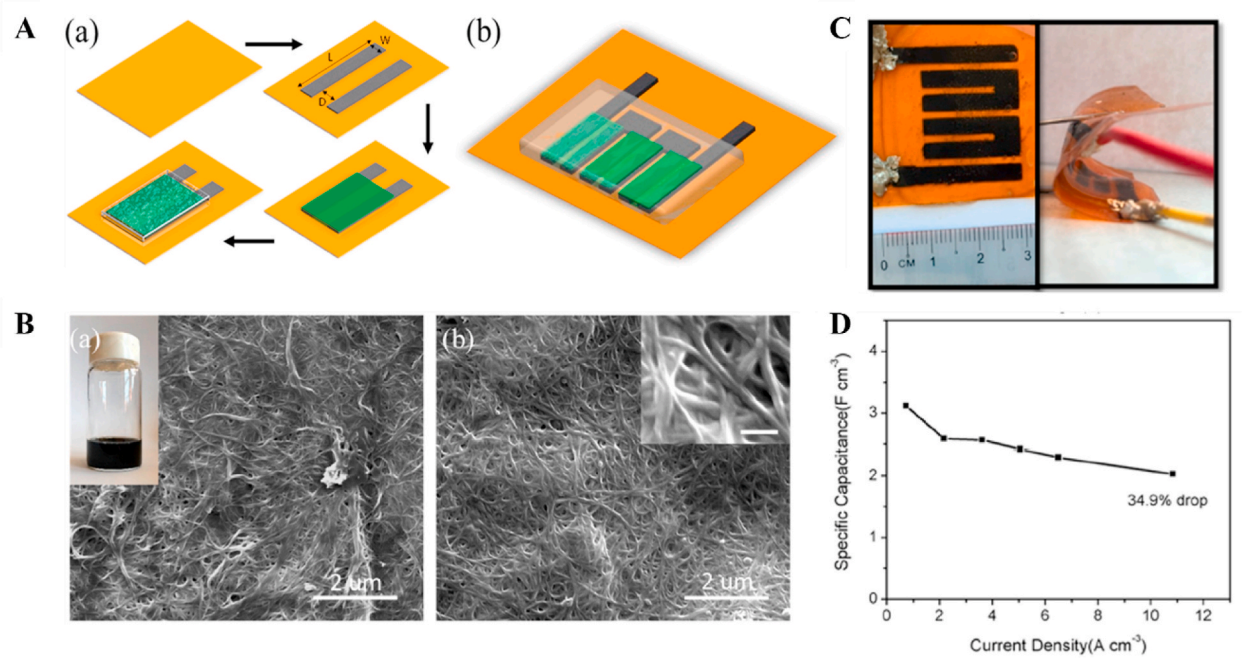

Fig. 23. (A) (a) Schematic of Layer Design and Printing Process for DIW of the Proposed Supercapacitors; (b) Array of Three Identical Cells Connected in Series (B) (a) SEM of as-printed CNT electrode surface without acid treatment and developed SW-CNT ink. (b) SEM of the acid-treated electrode surface. (C) Optical picture of the as-printed 3-cell supercapacitor array. (D) Calculated specific capacitance at different current densities (Chen et al. [195]).

printing capability showed the capability of DIW in fabricating complex devices. This work is illustrated in Fig. 23.

The structural design of the supercapacitors played a critical role in their performance. The study investigated the impact of electrode pattern width and gap distance on specific capacitance. Wider electrode patterns and narrower gap distances were found to strengthen specific capacitance. The scalability of the technology was also demonstrated by printing multicell supercapacitor arrays with three identical cells connected in series. In terms of property, the supercapacitors exhibited high specific capacitance and good rate capability, with only a 34.9 % drop in specific capacitance as the current density increased. This highlighted the excellent performance of the printed devices. Moreover, the cyclic stability of the supercapacitors was evaluated, showing a minimal decrease in cell capacitance after 1000 cycles of charge/discharge, indicating long-term stability and reliability. The fully packaged SW-CNT supercapacitors measured energy and power performances comparable to planar carbon-based supercapacitors, which demonstrated that high performance could be achieved through the DIW process. In summary, these supercapacitors exhibited excellent capacitance performance, cyclic stability, and energy/power characteristics, positioning them as promising energy storage solutions for various applications.

Idrees et al. introduced an innovative approach to creating AM thin-film solid-state supercapacitors, whereby both the electrodes and electrolyte are printed using the DIW technique without any post-processing [196]. The fabrication process involved AM of supercapacitor electrodes and electrolytes using a Hyrel3D 30 M printer with an extrusion head, as shown in Fig. 24. Activated carbon mixed with a PVA/H3PO4 electrolyte solution formed a paste for the electrodes, with approximately 35 wt% activated carbon. The solid electrolyte is prepared by mixing PVA with deionized water and phosphoric acid, then 3D printed using specific parameters.

Characterization techniques such as XRD, Raman spectroscopy, SEM, and TEM revealed the microstructure and morphology of activated carbon and DIW electrode surfaces. The electrodes exhibited a porous structure with gaps between printed beads, allowing for efficient charge storage and electrolyte penetration. Activated carbon showed a lower extent of crystalline graphitic domains, with D and G bands in the Raman spectrum indicating disordered graphitic rings and controlled oxygen levels. EDS analysis confirmed the presence of carbon, oxygen, and nitrogen.

This DIW-printed supercapacitor exhibited a capacitance of 328.95 mF/cm^2 at 2.5 mA, the highest reported among similar devices, as observed from GCD and CV curves. This high capacitance is attributed to the use of porous activated carbon and high loading. In addition, boosted energy density and power density were achieved. The devices demonstrated good cyclic stability, with only a small capacitance decrease over 500 cycles. The reliable paste extrusion process eliminated significant post-processing, streamlining manufacturing. In summary, these supercapacitors possessed high capacitance, improved energy storage, and stability, and they could be efficiently fabricated using packaging waste-derived materials.

In addition, Li et al. have also presented an innovative method for fabricating stretchable micro-supercapacitors with superior electrochemical performance [185]. This approach involved ink-writing and unidirectional freezing of a pseudoplastic nanocomposite gel composed of $Ti_3C_2T_x$ MXene nanosheets, manganese dioxide nanowires, silver nanowires, and fullerene. The resulting electrodes exhibited a thick, honeycomb-like porous structure, which contributed to enriched areal energy and power density due to increased active material loading, a larger interfacial area, and accelerated ion transport. The AM micro-supercapacitor demonstrated an exceptional areal capacitance of 216 mF/cm^2 at a scan rate of 10 mV/s and maintained stability even when stretched by up to 50 % and subjected to 1000 stretch/release cycles. Moreover, the micro-supercapacitor displayed an impressive areal energy density of 19.2 μWh/cm^2 and power density of 58.3 mW/cm^2. The results are shown in Fig. 25. This strategy represents a promising advancement towards the practical application of stretchable energy storage devices in wearable and portable electronic devices.

Inkjet printing (IJP) is increasingly recognized for its potential in fabricating supercapacitors, as highlighted by various research

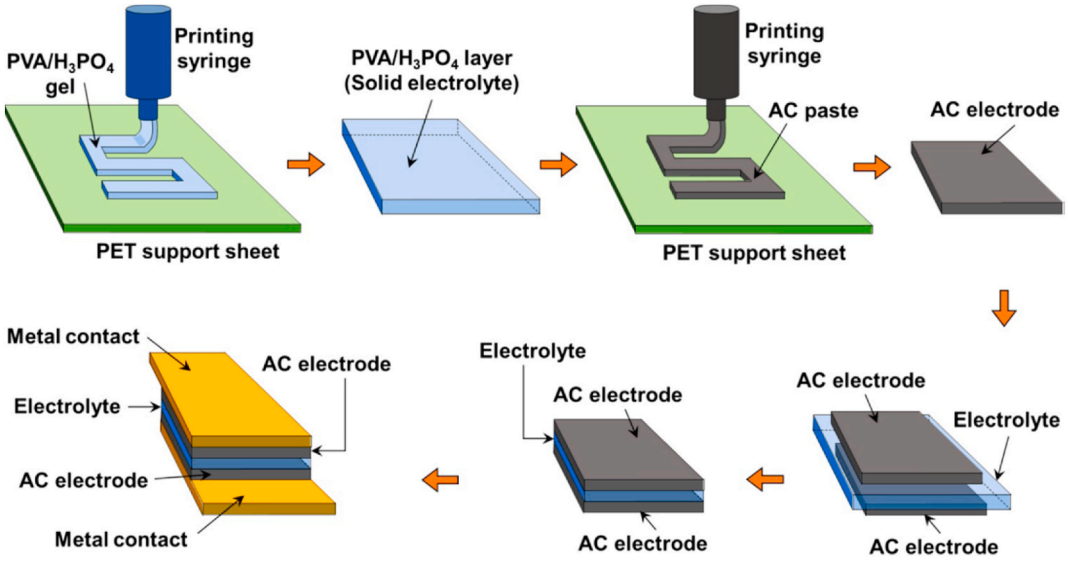

Fig. 24. Schematic representation of the supercapacitor fabrication process (Idrees et al. [196]).

studies. In the review paper by Sajedi-Moghaddam et al. [197], they detail multiple processing techniques used in inkjet printing to create supercapacitor components. IJP is favored for its precision, cost-effectiveness, and ability to produce high-resolution patterns. The process involves digitally controlling the deposition of liquid ink, which can be tailored to produce intricate designs essential for efficient energy storage devices. The formulation of inks is a critical aspect of IJP. These inks typically contain active materials such as carbon nanotubes, graphene, or metal oxides. The rheological properties of the ink—such as viscosity and surface tension—are crucial as they directly influence the printing process and the quality of the deposited layers. Properly formulated inks ensure that the printed materials form the desired microstructures, which are key to the performance of the final supercapacitor.

The properties of supercapacitors, such as high energy density, fast charge/discharge rates, and long-term stability, are largely determined by the microstructure of the printed materials. The paper highlights that combining IJP with novel materials like graphene/MnO_2/PANI nanocomposites can provide supercapacitors with superior performance metrics.

Zhang et al. have demonstrated the use of additive-free, two-dimensional titanium carbide ($Ti_3C_2T_x$) MXene inks to print supercapacitors [198]. These inks were aqueous for extrusion printing and organic for IJP, respectively. High printing resolution and spatial uniformity were achieved. The resulting MXene micro-supercapacitors exhibited distinct structural characteristics based on the printing technique employed, shown in Fig. 26. Direct ink-printed devices featured compacted structures with stacked and interconnected MXene nanosheets forming continuous films. These structures eliminated the need for additional current collectors and conductive agents thereby improving the overall conductivity and energy storage efficiency of the devices. deposition offered by IJP ensured that the printed lines maintained optimal thickness and spacing, which maximized the performance of the device.

The superior properties of all-MXene-printed micro-supercapacitors stem from several key factors. Firstly, the metallic conductivity of the extrusion-printed lines and IJP patterns was essential for the efficient operation of the devices. Secondly, the strong adhesion of stacked MXene sheets, facilitated by hydrogen bonds, contributed to the high conductivity of the printed structures. Thirdly, the intensified energy storage capacity was attributed to the unique structure of MXene nanosheets, which offered a large surface area for charge storage.

With a volumetric capacitance of up to 562 F cm^{-3} and an energy density reaching 0.32 μW h cm^{-2}, these devices outperformed existing printed materials, demonstrating exceptional energy storage capabilities. Meanwhile, their excellent mechanical flexibility allowed them to bend and conform to different shapes without compromising performance, making them suitable for deformable or wearable energy storage devices. Moreover, the stable electrochemical cycling performance, with high capacitance retention over 97 %–100 % during cycling, ensured the longevity and reliability of the devices. Furthermore, the oxidation stability of MXene nanosheets during the printing process ensured the structural integrity and performance of the printed devices. Raman spectra analysis confirmed that the characteristic peaks of MXene were well retained in the extrusion-printed lines, indicating minimal oxidation during printing. This stability is essential for maintaining consistent device performance over time, even under harsh operating conditions. In summary, the combination of advanced printing techniques and unique material properties enabled the fabrication of high-performance micro-supercapacitors using MXene ink, offering promising solutions for various energy storage applications.

Ervin and Le reported a study on the IJP of GO ink for supercapacitors [199]. As shown in Fig. 27, their process began with the precise deposition of GO ink onto metal foil current collectors using an inkjet printer. The subsequent step involved annealing the printed electrodes at 200 °C for 10 h to reduce GO to conductive reduced graphene oxide (rGO) to increase the conductivity of the electrodes, which could affect the charge/discharge efficiency and overall performance of the device. The resulting structure of the graphene electrodes was determined by the printing process and the subsequent reduction step. The choice of substrate, such as flexible Kapton substrates with or without FEP coatings, affected the mechanical stability and flexibility of the supercapacitor.

The capacitance measurement revealed promising values, with the electrodes exhibiting 124 F/g at a scan rate of 20 mV/s, emphasizing their energy storage potential. Thermal annealing at 200 °C for 10 h reduced GO to conductive graphene and significantly

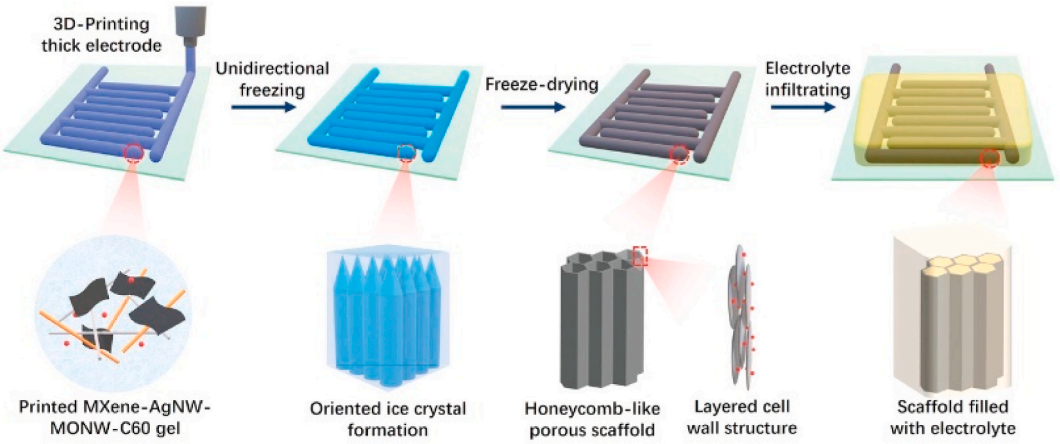

Fig. 25. Schematic illustration of the fabrication process of intrinsically stretchable micro-supercapacitors through AM and unidirectional freezing. The AM thick interdigitated electrodes possess a honeycomb-like porous structure in combination with a layered cell wall architecture (Li et al. [185]).

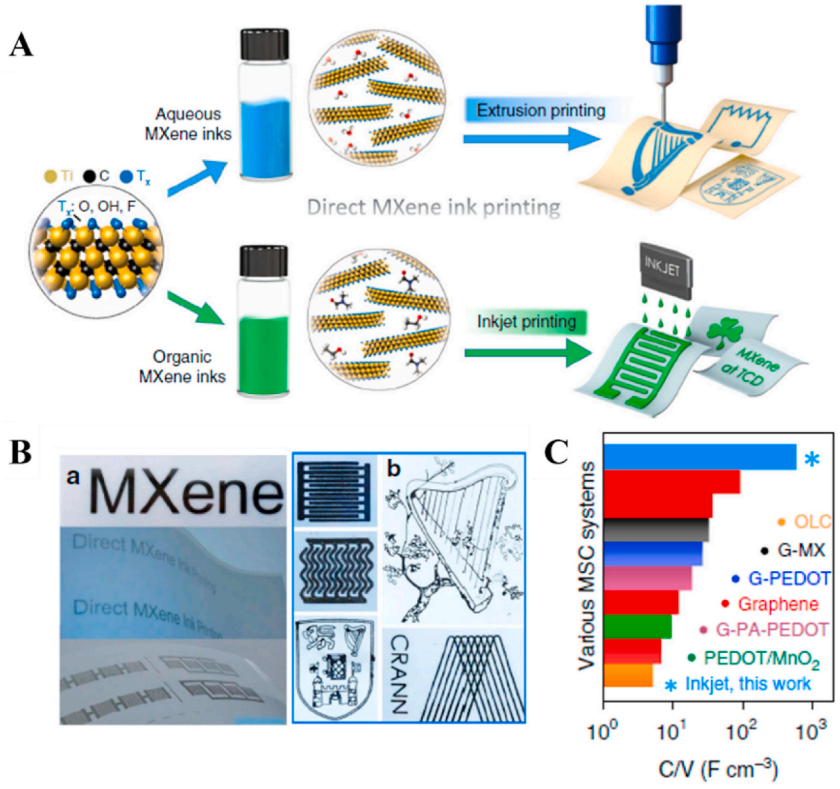

Fig. 26. (A) Schematic illustration of aqueous direct MXene ink print and organic MXene IJP. (B) (a) Optical images of IJP "MXene" word (b) Optical images of direct ink-printed patterns. (C) volumetric capacitance (C/V) comparison of this work to other reported MSC systems(Zhang et al. [198]).

boosted specific capacitance. Assessments of cycle life performance highlighted the stability and durability of the electrode across numerous charge-discharge cycles. Furthermore, comparisons of annealing conditions emphasize the impact of temperature on specific capacitance. In summary, the thermal reduction process ensures uniform conductivity and performance, fostering consistency important for dependable device operation. This research demonstrated the potential of the IJP technique in fabricating flexible graphene-based supercapacitors with advanced energy storage capabilities.

Le et al. conducted a systematic investigation into the fabrication and properties of IJP-printed graphene electrodes tailored for supercapacitor applications [200]. As shown in Fig. 28, their approach started with the preparation of GO ink, which underwent thorough dispersion in water and subsequent treatment involving sonication and filtration before being loaded into the printhead cartridge. Leveraging sophisticated piezoelectric nozzles, the inkjet printer then precisely deposited droplets onto titanium surfaces, with each droplet generating spherical ink at a velocity of approximately 7.5 m/s. Subsequently, a critical thermal reduction process was employed, occurring at 200 °C within a nitrogen atmosphere, effectively transforming GO into conductive graphene. The resultant electrode structures exhibited distinctive morphological characteristics, as evidenced by SEM analysis, which revealed disk-shaped dots with discernible island features and continuous boundaries. A notable transformation occurred in terms of electrical conductivity, with post-reduction resistance plummeting to below ~1 MΩ, signifying a significant improvement over the infinite resistance observed in the as-printed GO film. Electrochemical assessments yielded specific capacitance values ranging from 48 to 132 F/g. This suggested that the electrochemical behavior of the IJP-printed electrode was on par with traditionally prepared electrodes. However, challenges persisted in achieving comparable power density levels to carbon nanotube-based counterparts due to inherent interconnectivity limitations among 2D graphene nanosheets for electron conduction and 3D mesoscale porosity for ion conduction.

The thermal reduction process played an essential role not only in improving electrical conductivity but also in fostering stability and reliability by facilitating the formation of a well-connected graphene network within the electrodes. This augment holds significant implications for the long-term performance and durability of the electrodes in supercapacitor applications. Moreover, the precision afforded by IJP enabled the realization of new electrode designs with a lateral spatial resolution of approximately 50 μm, effectively solving safety, health, and environmental concerns associated with the handling of nanomaterials like graphene while mitigating waste generation and raw material usage.

Li's research, shown in Fig. 29, presents a comprehensive exploration of the fabrication process for flexible micro-supercapacitors using IJP [201]. The methodology delved into the intricate details of ink formulation, wherein aqueous inks containing GO and ammonium molybdate tetrahydrate were prepared and fine-tuned for optimal performance during IJP onto flexible substrates. Subsequent thermal treatment of the printed inks served as an important step to catalyze the transformation into rGO/molybdenum

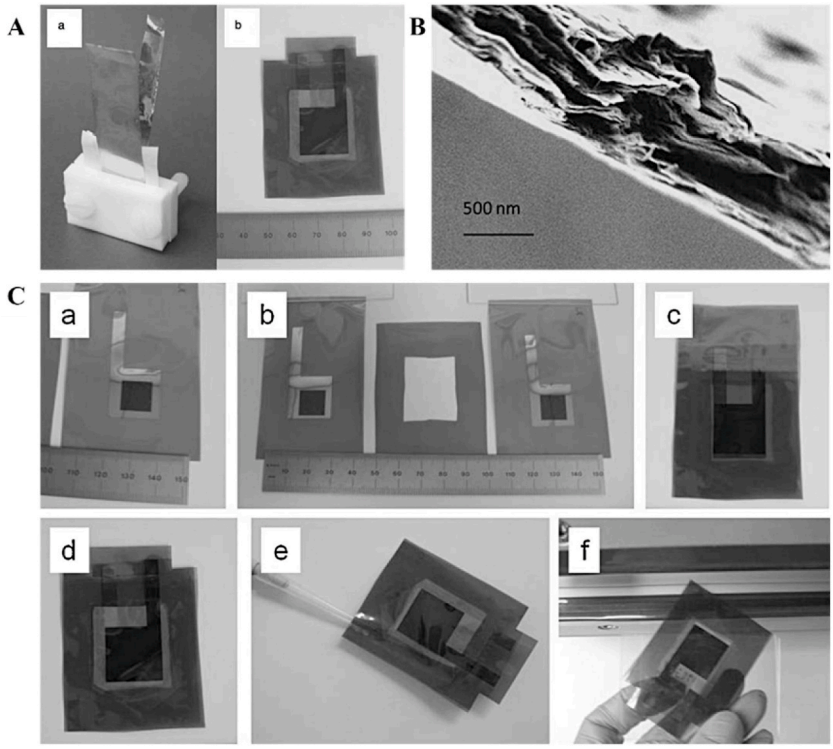

Fig. 27. (A) (a) IJP graphene on metal foil current collectors tested in a rigid clamp, (b) heat-sealed device made with IJP graphene and evaporated metal on Kapton current collectors (B) SEM image of IJP graphene on a silicon wafer (C) Flexible supercapacitor assembly process: (a) GO printed on a metal current collector on Kapton and reduced at 200 °C, (b) two electrodes were assembled with an intervening frame of FEP-coated Kapton, (c) electrodes were heat sealed face to face on three sides, (d) the polypropylene separator was placed between the electrodes, (e) the electrolyte was added, and (f) the final seal was made(Ervin et al. [199]).

trioxide (MoO_3) hybrids, thereby bolstering structural integrity, and augmenting electrochemical properties. The resultant RGO/MoO_3 electrodes exhibited a highly desirable close-contact structure, with MoO_3 nanosheets deposited on the surfaces and interfaces of RGO nanosheets. This strategic architecture not only amplified the active surface area but also curbed restacking tendencies, facilitating the construction of planar ultrathin flexible micro-supercapacitors with exceptional electrochemical prowess. These devices delivered an impressive array of performance metrics, including a wide voltage window spanning 0−0.8 V, a volumetric specific capacitance of 22.5 F cm^{-3}, and robust cyclic stability, retaining 82 % of their capacity even after 10,000 charge-discharge cycles.

Of particular significance are the energy storage capabilities of these micro-supercapacitors, showing a maximum energy density of 2 mWh cm^{-3} and a power density of 0.018 W cm^{-3}. Moreover, the inherent flexibility of these devices not only broadened their scope for integration into wearable and flexible electronics but also emphasized their resilience to bending and deformation without compromising performance. Through optimization of ink properties, printing parameters, and thermal treatment conditions, the study elucidates pathways for achieving superior device performance, thereby charting a course for IJP to revolutionize the landscape of energy storage technologies. The study explained the inherent advantages offered by IJP technology, such as cost-effectiveness, repeatability, and scalability, which position it as a frontrunner in the quest for fabricating high-performance micro-supercapacitors.

Sajedi-Moghaddam et al. research on MnO_2 nanoflowers on surface-modified A4 paper for flexible All-Solid-State micro-supercapacitors proves developing high-performance flexible micro-supercapacitors (MSCs), as shown in Fig. 30 [202]. The process initiates with the surface modification of standard A4 paper by spray-printing a conductive layer composed of graphene and silver nanowires (Ag NWs). This step is critical as it creates a conductive and adhesive substrate essential for the subsequent MnO_2 deposition. The choice of materials and the method of deposition directly influence the microstructure of the final device.

Following surface modification, MnO_2 ink is prepared by dispersing MnO_2 powder in a solvent system of ethanol and ethylene glycol. The inkjet printing technique is then employed to deposit MnO_2 nanoflowers onto the modified paper. Inkjet printing offers precision in material deposition, ensuring a uniform and controlled microstructure. Multiple layers of MnO_2 are printed in a patterned fashion, optimizing the electrochemical properties of the MSCs. The ability to finely control layer thickness and uniformity through the printing process directly affects the structural integrity and surface morphology of the MnO_2 electrodes.

The structural characteristics of the MnO_2 nanoflowers, including their high surface area and porous nature, are crucial for enhancing electrochemical performance. These features facilitate efficient ion transport and provide more active sites for electrochemical reactions, which are essential for high capacitance. The structure-property relationship is evident as the specific nanostructure of MnO_2 contributes to the MSC's high areal capacitance of 0.68 mF/cm^2 at a current density of 25 μA cm^{-2}. Additionally, the

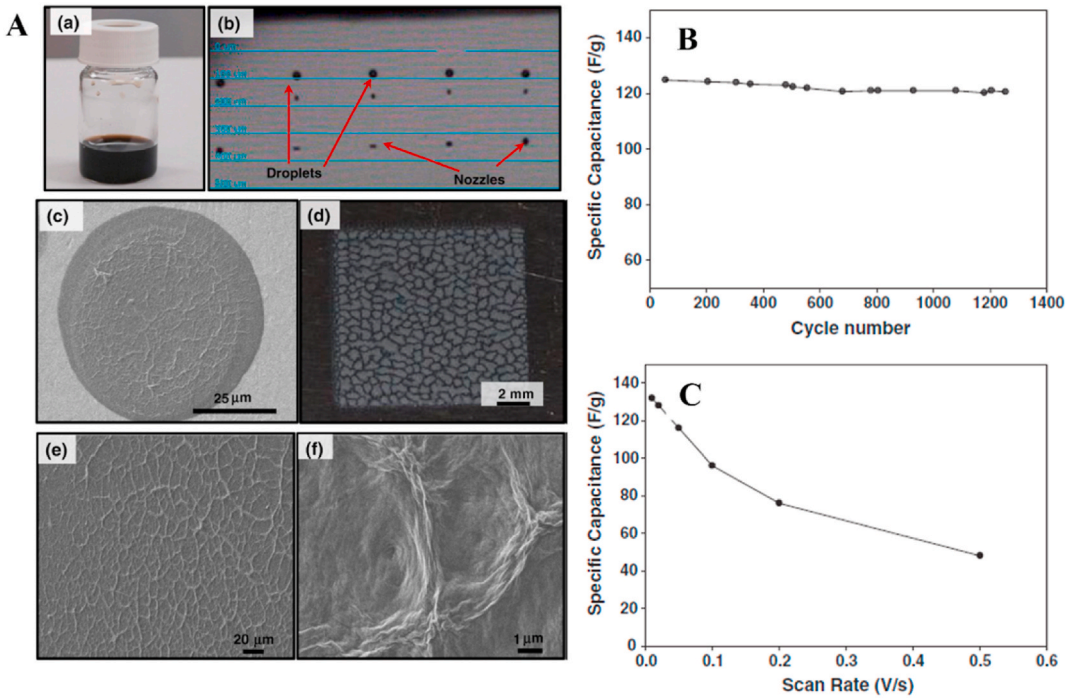

Fig. 28. (A) IPGE ink and morphology: (a) GO dispersed in water at 0.2 wt% as a stable ink; (b) spherical ink droplets generated by piezoelectric nozzles; (c) SEM image of a circular GO dot printed on the Ti foil surface after 20 printing passes at a spatial resolution of ~50 μm; and (d), (e) and (f) SEM images of IPGE printed on the Ti surface used for electrochemical evaluation. (B) specific capacitance retained as a function of CV cycles (C) specific capacitance as a function of voltage scan rates (Le et al. [200]).

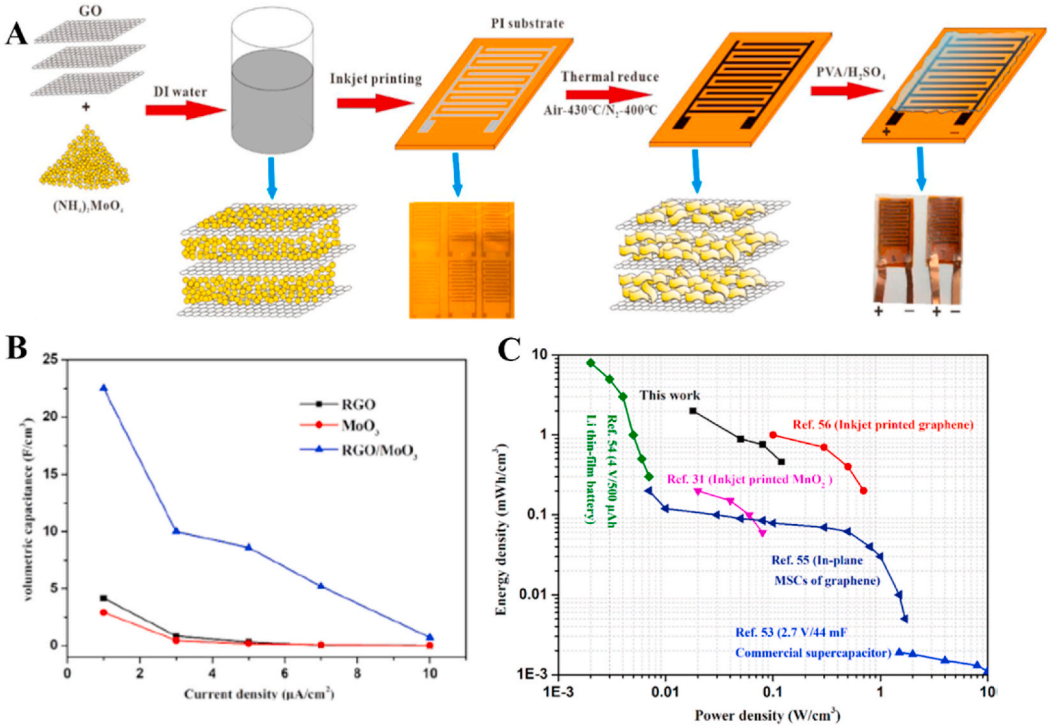

Fig. 29. (A) Schematic illustration of the fabrication of RGO/MoO3 nanosheets for solid-state micro-supercapacitors. (B) The evolution of the areal capacitance versus current densities for MoO3, RGO, and RGO/MoO3 nanocomposites (C) Energy and power density plot of the IJP MSCs and comparison with other literature (Li et al. [201]).

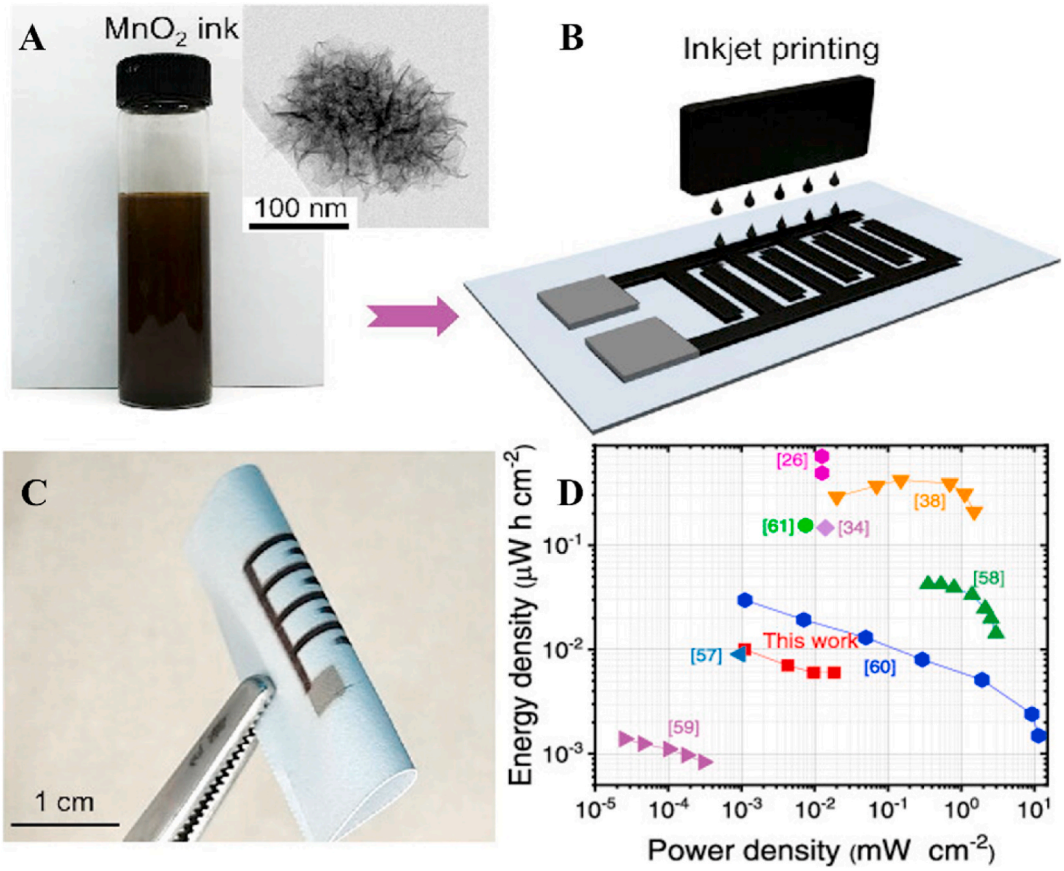

Fig. 30. (A) Photograph of the formulated MnO_2 ink. (B) Schematic of the preparation process of printed paper-based flexible MSCs. (C) Digital photograph of inkjet-printed flexible MSC. (D) Areal Ragone plot shows the energy density and power density of the inkjet-printed device, in comparison with other MSCs (Sajedi-Moghaddam et al. [202]).

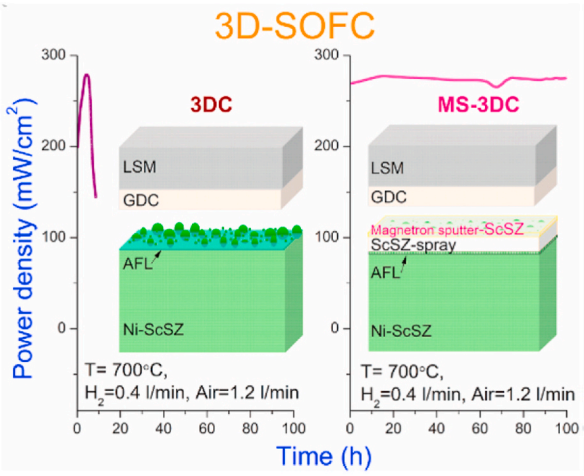

Fig. 31. Powder density of DIW SOFC with and without hybrid ScSZ layer consisting of a thick (~5 μm) ScSZ layer by spray coating and ~2 μm dense ScSZ by magnetron sputtering (Rath et al. [123]).

flexible paper substrate and the inherent mechanical stability of the MnO_2 nanostructure ensure that the MSCs maintain performance even under mechanical deformation, which is a critical property for flexible and wearable electronics.

3.2.3. *Fuel cells manufactured using direct ink writing and inkjet printing*

The utilization of DIW technology holds significant promise in the manufacturing of SOFCs. Especially, Rath et al. [123] conducted research on applying DIW in producing SOFCs, as illustrated in Fig. 31. These DIW-printed SOFCs featured an anode composed of NiO-added Sc_2O_3 stabilized zirconia (ScSZ) and a cathode made of lanthanum strontium manganite (LSM), with spin-coated electrolyte layers. The research revealed a peak power density of 442 mW/cm^2 for these SOFCs after integrating a hybrid ScSZ layer. This hybrid layer, consisting of a spray-coated ScSZ layer and a dense ScSZ layer produced via magnetron sputtering, played an essential role in protecting against ceria reduction on the anode side and improving contact between the layers during operation.

DIW technology offered optimization over the deposition of electrodes and electrolytes, allowing for the creation of complex structures tailored to specific properties. Achieving the desired electrode microstructure and final properties relied heavily on optimizing ink viscosity. DIW printers enabled customization and assembly according to specific requirements, thereby refining flexibility in fabrication processes. The microstructure of the electrodes, influenced by ink viscosity and printing parameters, played a critical role in determining electrochemical properties. The insertion of a hybrid ScSZ layer strengthens the contact between the electrolyte and anode, thereby improving performance metrics. These DIW-printed SOFCs exhibited impressive properties, including a peak power density of 368 mW/cm^2 at 800 °C and exceptional long-term stability. The incorporation of the hybrid ScSZ layer led to significant improvements in electrochemical performance, such as reduced polarization resistance and increased power density. Furthermore, the microstructural analysis indicated no interdiffusion or delamination after extended operation, highlighting the durability of the fabricated cells. The significance of the 0.854 % per hour voltage loss rate experienced by the DIW-printed SOFC after 100 h lies in its implications for long-term stability and performance. This rate suggested gradual performance degradation and helped assess maintenance and optimization needs, while also enabling comparative analysis with similar fuel cell configurations.

However, DIW still has some limitations that demand further investigations. Post-processing steps such as curing or drying are required in DIW, adding complexity to the manufacturing process. Scaling up DIW for industrial production, as with many other AM techniques, proves to be challenging due to the relatively slow production rate and inadequate process stability and repeatability. IJP offers a promising avenue for fabricating highly porous structures with nano-sized grain structures, leading to significant increases in specific surface area and electrochemical reactivity. Moreover, its ability to provide accurate tuning at the nano-level through carefully designed ink solutions makes it adaptable to a wide range of applications, including fuel cells.

Sobolev et al. demonstrated the unique advantages of IJP SOFCs utilizing a NiO colloidal ink solution [203]. The researchers successfully fabricated the main anode component on an electrolyte substrate using a monodispersed stable NiO ink colloidal solution. The synthesis process of NiO nanoparticles began with the dissolution of nickel nitrate hexahydrate in distilled water, followed by the addition of agents such as ammonium carbonate and Triton X-100 surfactant. After a mixing process, a clear, green-colored colloidal solution containing NiO nanoparticles was obtained. Dynamic Light Scattering (DLS) and HRTEM techniques were employed for

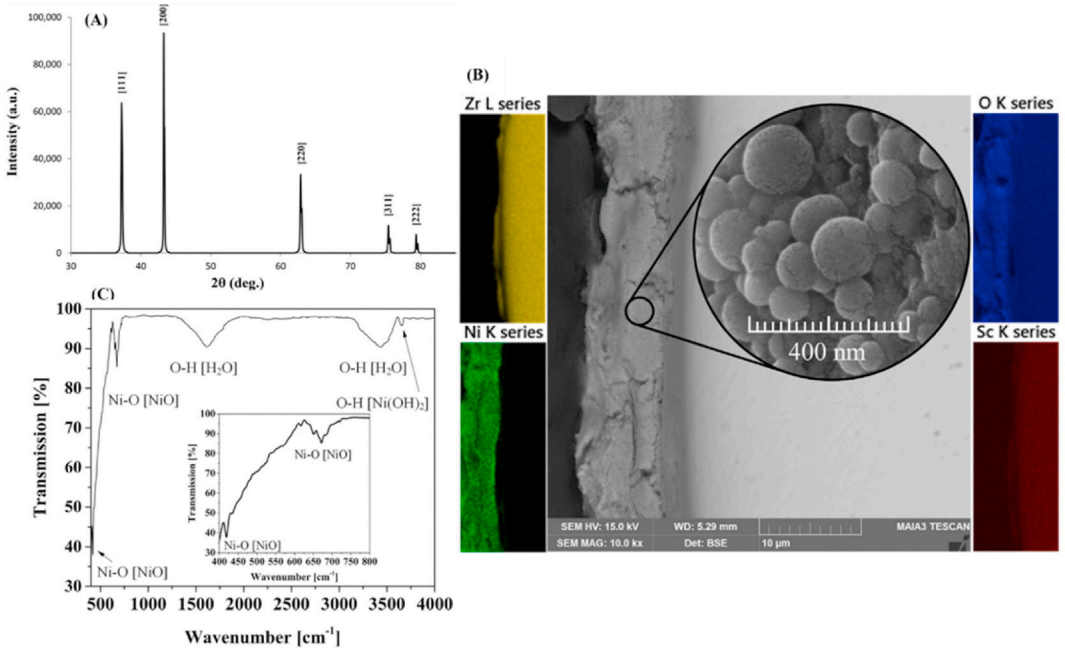

Fig. 32. IJP SOFC anode with NiO ink solution (A) XRD pattern of the calcined NiO printed coating. (B) SEM image of calcined printed coating enlarged area of the coating and mapping of the elemental distribution. (C) FTIR spectrum of calcined printed coating (Sobolev et al. [203]).

particle size measurements and detailed structural analysis, respectively. These findings are illustrated in Fig. 32. XRD analysis revealed the cubic structure of NiO nanoparticles, which could affect their thermal, electrical, and catalytic properties. SEM analysis showed the influence of NiO nanoparticles on the overall structure and homogeneity of the printed coating. The homogeneous coating comprising near-spherical NiO nanoparticles contributed to the stability and efficiency of the anode material. Furthermore, Fourier Transform Infrared (FTIR) spectroscopy identified specific chemical bonds, such as Ni–O bonds, within the printed coating. This provided valuable insights into its chemical composition and bonding.

IJP offers control over material deposition, facilitating the creation of nanostructured anodic layers. Rahumi et al. developed and characterized a single-step wet-chemical synthesis of NiO-SDC (Sm^{3+} doped ceria) colloidal ink for IJP of nanostructured anodic layers [204]. These layers were printed on commercial scandia-stabilized zirconia-ceria (10ScCeSZ) dense electrolyte, followed by sintering to burn out organic binders and minimize warpage defects. This work is illustrated in Fig. 33. XRD analysis of the IJP NiO-SDC layer sintered at 1250 °C revealed a highly crystalline composition, including $Ce_{0.8}Sm_{0.2}O_{1.9}$ (SDC), bunsenite (NiO), and $(Zr_{0.81}Sc_{0.18}Ce_{0.01})O_{1.91}$ (substrate material). The IJP anodic layers exhibited a conjugated nanostructured morphology with a bimodal distribution of nickel (Ni) and Sm^{3+} doped ceria (SDC) particles, where nanosized SDC particles uniformly surrounded submicron Ni particles. This unique microstructure extended the triple-phase boundary (TPB) length at the electrolyte-electrode interface and increased TPB site concentration, thereby reducing charge transfer resistance during hydrogen oxidation reaction (HOR) and improving catalyst activity. The porous microstructure of the post-sintered NiO-SDC layer with voids between particles provided an effective gas diffusion path through the anode.

Overall, the porous post-sintered IJP Ni-SDC layer demonstrated bimodal near-spherical nanoparticles with specific size ranges, an optimized porous microstructure that could increase gas diffusion efficiency and reduce charge transfer resistance. These were crucial factors contributing to the improved catalytic activity and performance of solid oxide fuel cells.

3.2.4. *Catalyst scaffolds manufactured using direct ink writing and IJP*

DIW and IJP offer promising avenues for catalyst printing due to their precision, material efficiency, rapid prototyping capabilities,

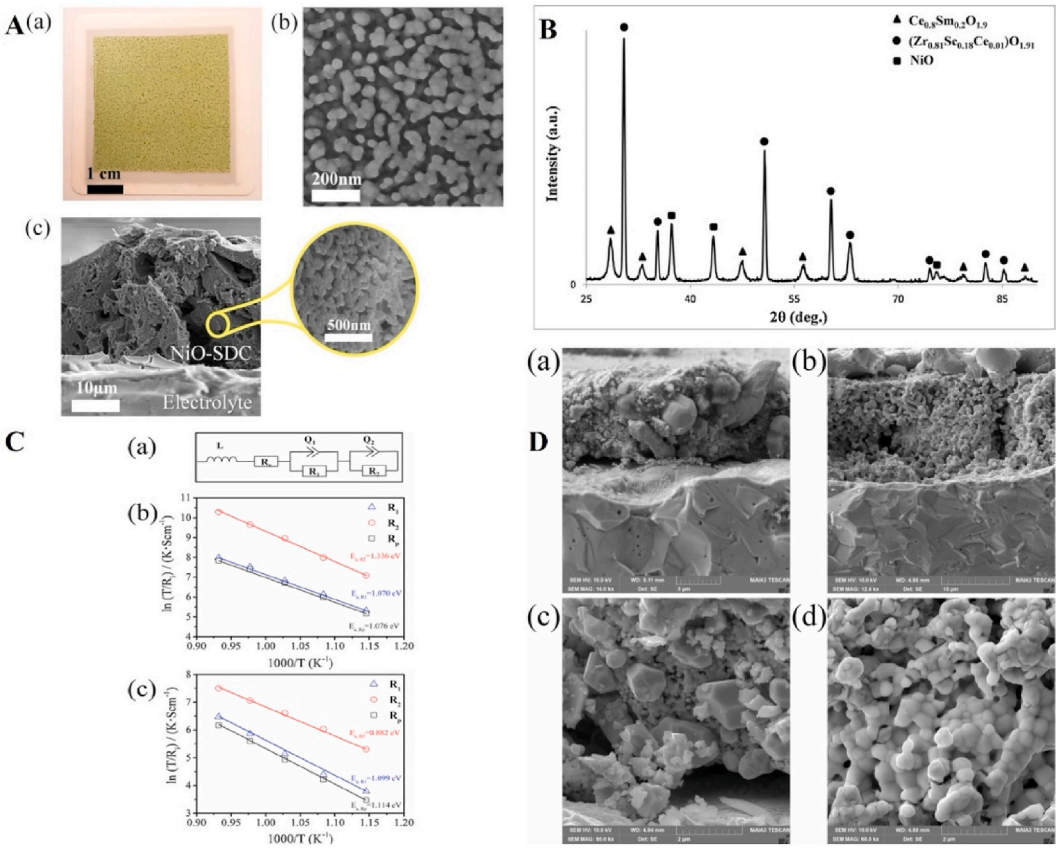

Fig. 33. IJP SOFC anode with NiO-SDC colloidal ink solution (A) (a) Photographic image of IJP NiO-SDC layer on 10ScCeSZ electrolyte sintered at 1250 °C, and the SEM images of NiO-SDC(b) top view and (c) cross-section (B) XRD pattern of the IJP NiO-SDC layer on 10ScCeSZ electrolyte. (C) (a) The equivalent circuit of the NiO-SDC half-cell. Interfacial (Ri) and the polarization resistance(Rp) of the (b) I-NC and (c) S-NC.(D) SEM images of the half-cell fabricated by (a) IJP and (b) screen printing method. The corresponding HR-SEM images of the Ni-SDC of (c) I-NC and (d) S-NC (Rahumi et al. [204]).

and the ability to integrate multiple materials. These techniques enable the fabrication of catalysts with unique geometries and tailored pore structures that optimize surface area and activity for specific reactions. By depositing materials only where necessary, DIW and IJP reduce wastage, particularly beneficial for expensive or rare catalyst materials. Furthermore, their flexibility in prototyping and scalability streamlines development cycles and production scaling. The integration of multiple materials into a single catalyst structure can potentially amplify properties like thermal stability and catalytic performance. These advantages position DIW and IJP as valuable methods for advancing catalyst manufacturing, potentially leading to more efficient and effective catalytic processes.

In water splitting, DIW and IJP prove invaluable for fabricating electrodes with tailored catalytic properties to drive efficient hydrogen and oxygen evolution reactions, as they allow customization of electrode designs to augment catalytic activity and stability [205]. As shown in Fig. 34, Cagirici et al., discussed the fabrication of Ni meshes using a specially formulated NiO ink that exhibited shear-thinning behavior, essential for effective extrusion through small nozzles [206]. They emphasized that optimizing the ink viscosity relative to the shear rate, along with DIW parameters such as pressure and speed, was critical for producing complex geometries in functional Ni meshes. The microstructure of Ni meshes was finely controlled through post-printing heat treatments, which adjust porosity, grain size, and density and ensure the microstructural integrity by avoiding cracks or delamination. XRD analysis confirmed the reduction of NiO to Ni during these treatments, a significant phase transformation essential for the desired catalytic properties.

The electrocatalytic performance of the Ni meshes was closely tied to their structural features such as surface area and porosity. These structures exhibited excellent catalytic activity for the oxygen evolution reaction (OER), demonstrated by a low overpotential of 222 mV at 10 mA/cm^2 and remarkable stability over 60 h at 1.58V. In addition, the mechanical properties of the meshes, including high yield strength and aspect ratio, were improved through careful ink formulation and thermal processing. This enabled the production of robust, free-standing structures that could withstand operational stresses. Overall, the Ni meshes fabricated through DIW showed promising electrochemical performance, structural integrity, and mechanical properties, which makes them suitable for industrial-scale applications in water-splitting and other catalytic processes. The careful tuning of process parameters and structural characteristics through DIW led to optimized properties that fulfill the demands of practical electrocatalytic applications.

Fu et al. [207] researched DIW, utilizing the process to fabricate hierarchical porous gold structures with complex porosity levels, as shown in Fig. 35. The DIW process enabled digital control of macroscale porosity by adjusting printing parameters like nozzle size and pressure. The hierarchical porous gold structures exhibited macroscale (≈500 μm), microscale (1−10 μm), and nanoscale (≈50 nm) pores, and thereby good mass transport properties. This controlled porosity affected electrochemical reactions, with nanoscale pores increasing surface area and macroscale pores facilitating mass transport. The hierarchical porous gold electrocatalysts exhibited impressive CO_2-to-CO reduction current densities, reaching 64.9 mA/cm^2 with a CO partial current density of 33.8 mA/cm^2, attributed to the unique structure enabled by DIW. Stability over time was observed, with a slight degradation in overpotential, and a selectivity of around 52 % for CO_2-to-CO conversion. The hierarchical structure increased mass transport efficiency and contributed to high current densities. The study highlighted the importance of engineered architectures that balance reaction rate and selectivity and provided valuable insights for designing electrocatalysts for CO_2 reduction and beyond. The hierarchical porous gold electrocatalysts offered a platform for further optimization and scale-up efforts in electrocatalysis.

IJP has emerged as a prominent technique in catalysis, offering precise deposition of catalyst materials onto substrates with exceptional resolution and control, which brings several advantages. The detailed deposition enables controlled deposition of catalyst

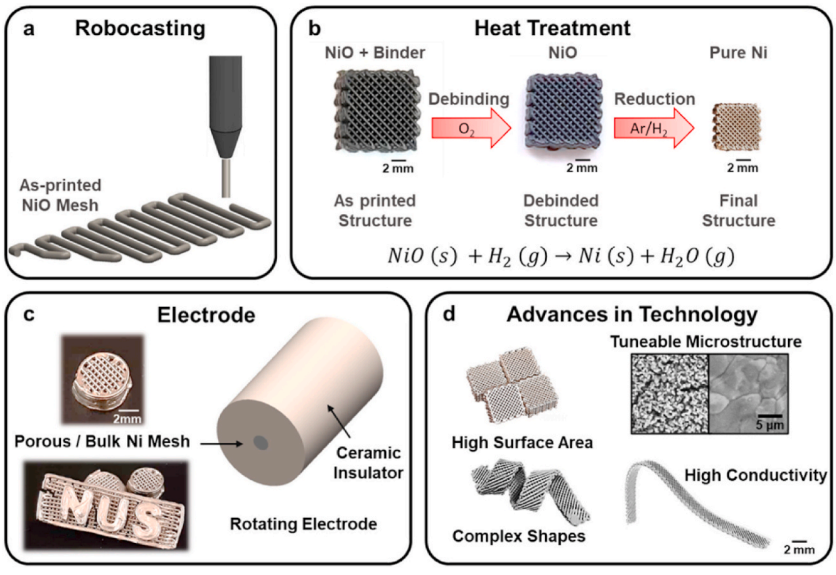

Fig. 34. Schematic illustration of metallic alloy fabrication using self-curable technique and metallic oxides. (a) Robocasting (DIW), (b) modified post-printing heat treatment, (c and d) potential applications and advances in metal fabrication via DIW(Cagirici et al. [206]).

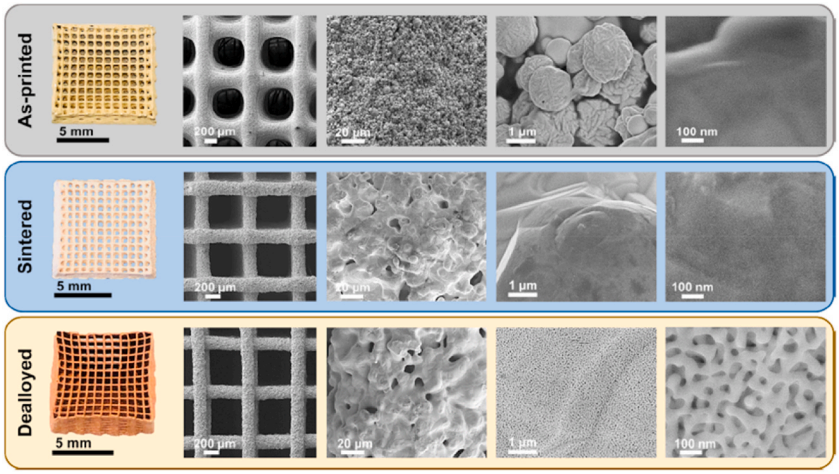

Fig. 35. Photograms and SEM images of hierarchical porous Au (HP–Au) at different processing stages (Fu et al. [207]).

materials, facilitating the creation of well-defined patterns and structures on diverse substrates to improve efficiency in catalytic processes, while minimizing material wastage for cost savings. Also, it is easily scalable for high-throughput production of catalytic materials, rendering it suitable for industrial applications [205].

Li et al. conducted a research process utilizing IJP, shown in Fig. 36. The process involved preparing inks containing MoS_2, PVP, and RGO dispersed in a mixed solvent of ethanol and deionized water [208]. These inks were prepared through the ultrasonic exfoliation of bulk MoS_2, resulting in the formation of MoS_2 and RGO nanostructures dispersed within. IJP facilitated the flexible deposition of catalysts in spatial patterns on various substrates, enabling the precise construction of electrocatalysts. The MoS_2-based electrocatalyst featured a 3D architecture with Cu film support, which fortified the exposure of active sites and facilitated electron transfer. Stability was ensured by the ink composition, with PVP assisting in surfactant-assisted exfoliation and RGO preventing restacking of MoS_2. The presence of defects and disorder in the MoS_2 structure, along with interactions between MoS_2 nanosheets and the substrate, influenced catalytic properties. Stability was demonstrated through potential sweeps for 5000 cycles, indicating the durability of the IJP electrocatalysts under continuous operation. The stable performance over extended cycling highlighted the reliability and robustness of the electrocatalyst for practical applications.

As for the hydrogen evolution reaction (HER), the 3D-structured MoS_2-based electrocatalyst exhibited high efficiency due to

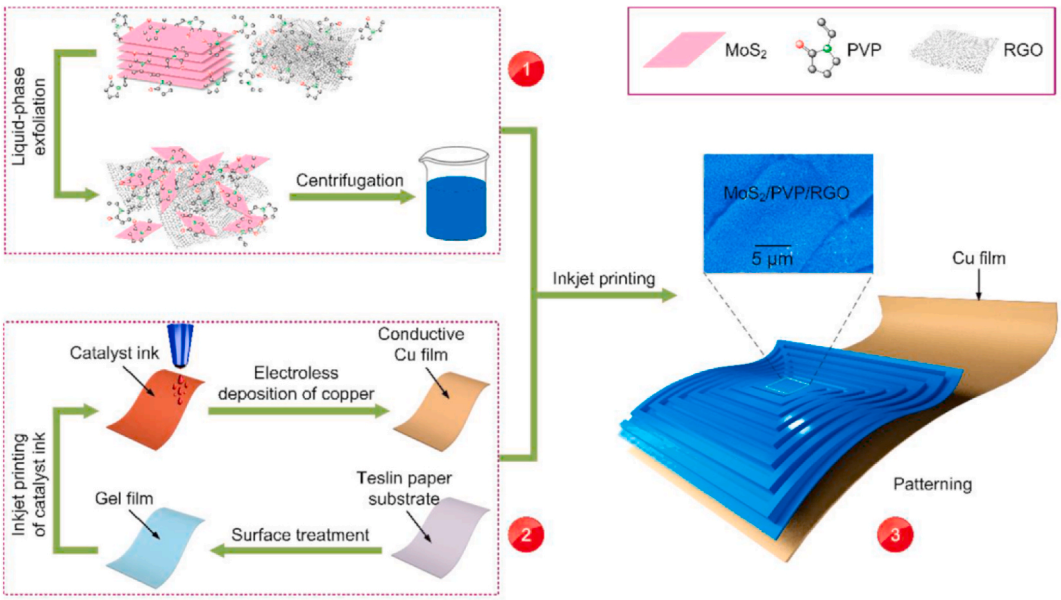

Fig. 36. General scheme for the preparation of catalytic electrodes with spatial patterning via IJP. The preparation process of MoS2/PVP/RGO ink (step 1), The fabrication of conductive Cu film on Teslin paper (step 2), and graphic printing of the MoS2/PVP/RGO ink, thus forming a spatial pattern of MoS2/PVP/RGO (step 3)(Li et al. [208]).

increased active site exposure, reduced charge-transfer impedance, and improved electron injection from the electrode. These catalytic materials, when formulated as inks for printing, demonstrated excellent HER activities, indicating their potential for industrial applications. Electronic coupling between the substrate and MoS_2 nanosheets, along with the presence of defects and disorder, played important roles in the electrocatalytic production of hydrogen. The electrocatalysts exhibited significantly lower overpotentials compared to pure catalysts, with the MoS_2/PVP/RGO catalyst requiring only 51 mV to achieve a current density of 10 mA cm^{-2}. A low Tafel slope of 32 mV dec^{-1}, comparable to Pt/C electrodes, suggested rapid kinetics and efficient hydrogen evolution. In terms of catalytic activity, the patterned c/PVP/RGO catalyst on Cu film exhibited advanced performance compared to planar catalysts, with ultrahigh cathodic current density and exceptional catalytic performance observed at different current densities. Furthermore, the electrocatalyst exhibited high intrinsic activity, with a per-site turnover frequency of 1.14 s^{-1} at a specific overpotential. This intrinsic activity provided insights into the fundamental catalytic properties of the material and its potential for industrial-scale hydrogen production.

Another research was conducted by Su et al. using IJP technology. As shown in Fig. 37, the researchers focused on the fabrication of uniform thin film patterns of zirconium-based porphyrinic MOF (MOF-525) [209]. The technology enabled management over the deposition of MOF crystal suspensions, allowing for layer-by-layer deposition and adjustment of film thickness by controlling the number of printed layers. The IJP process offered great precision in liquid administration, which positively affected the thickness and stacking of the printed MOF thin films. In terms of structure, the crystal sizes of MOF-525 were varied by adjusting the content of benzoic acid during synthesis, resulting in sizes ranging from 100 to 700 nm. The synthesized crystals exhibited a consistent surface area of 2500 m^2/g and a pore size of 1.85 nm, impacting the absorption and catalytic properties of the thin films. The morphology (i.e. film thickness, surface smoothness) of IJP MOF-525 thin films depended on the crystal size and substrate adhesion. Regarding electrocatalytic activity, the IJP MOF thin films were evaluated for nitrite oxidation and showed promising performance. Smaller crystal sizes led to more compact stacking and improved contact with the substrate. The ability to control film thickness through IJP influenced electrocatalytic behavior, with thicker films exhibiting different catalytic behaviors.

3.2.5. Sensors manufactured using direct ink writing and inkjet printing

The advantages of using ink-based AM for stretchable strain sensors are manifold. Firstly, it significantly reduces the fabrication complexity and cost, as it eliminates the need for expensive molds and substrates used in traditional methods. Secondly, it increases the functionality and performance of the sensors by allowing for the seamless integration of conductive elements with high precision and minimal material waste. This precision is essential for achieving the high degree of sensitivity and repeatability required in medical monitoring devices. Moreover, ink-based AM is inherently scalable and adaptable, facilitating rapid prototyping and customization that can adapt to the specific needs of different users or applications. This adaptability is particularly beneficial in the medical field where patient-specific devices can greatly elevate treatment outcomes.

Loh et al. employed DIW for the controlled deposition of graphene-based ink on substrates, as shown in Fig. 38 [210]. The ink formulation comprised graphene flakes and ethyl cellulose (EC) to adjust rheological properties and graphene concentration. Controlled drying and heating prevented the coffee ring effect, ensuring uniform graphene distribution. Characterization techniques, such as Raman spectroscopy, atomic force microscopy (AFM), and SEM, analyzed the film structure. The results revealed that graphene sheets draped over EC residues, which improved surface roughness and made available area for gas sensing. Layer-by-layer deposition facilitated the self-segregation of graphene, contributing to film uniqueness. Gas sensing performance was significant for methane (CH_4) and hydrogen (H_2), with nonlinear device response to increasing voltage when exposed to methane. This was attributed to interactions between gas molecules, graphene flakes, and thermal phonons. Electrical analysis evaluated conductivity and sensor response to different gases, demonstrating voltage-dependent sensitivity to CH_4 and H_2 in an argon environment. The evaporation-assisted solvent exchange method enabled graphene concentration tunability, while EC addition adjusted ink rheology. The robotic process allowed arbitrary film size and shape deposition, which could greatly increase the versatility of sensor design and

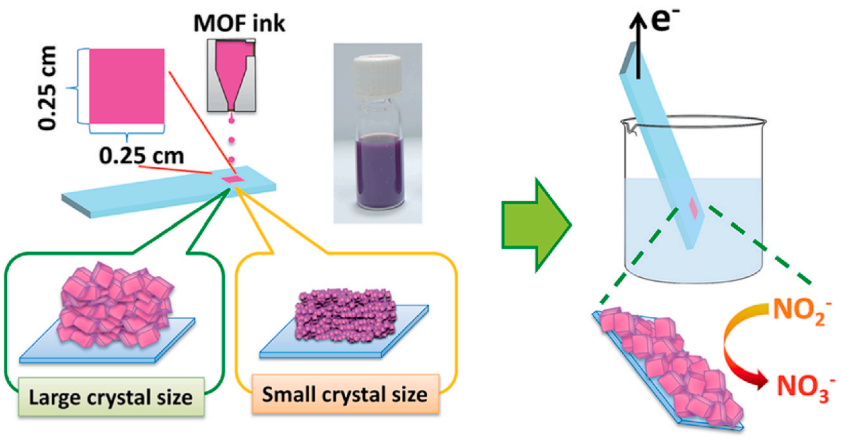

Fig. 37. Schematic representation of the IJP process and electrochemical measurements(Su et al. [209]).

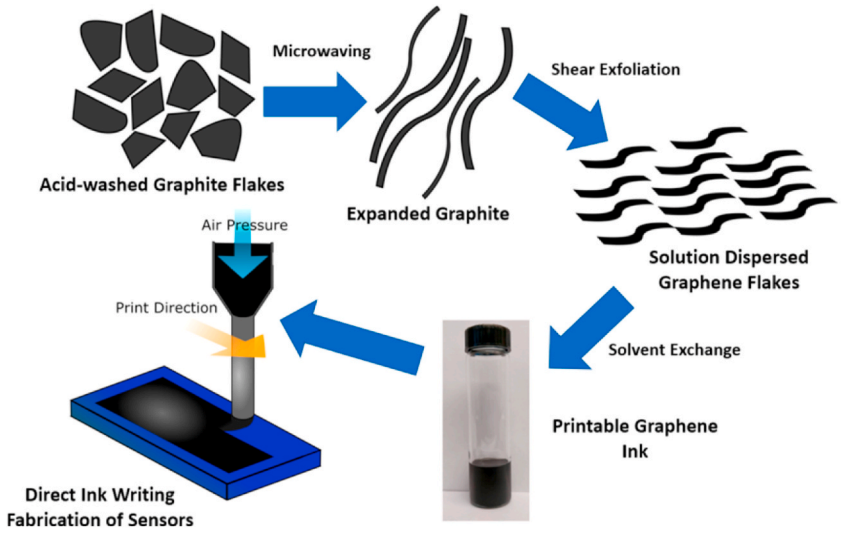

Fig. 38. Synthesis and processing schematic outlining the general procedure(Loh et al. [210]).

fabrication. These findings highlighted the potential of DIW sensors, with tailored structure and properties, for various gas sensing applications.

Chen et al. utilized a DIW process for sensor fabrication. The researchers employed a heterogeneous copolymerization route starting with monodispersed poly(butyl acrylate) (PBA) spheres synthesized via emulsion polymerization [211]. These spheres underwent a swelling process with 2-ethylhexyl acrylate (EHA) monomers, resulting in swollen-PBA spheres. The hydrogels formed consisted of linear poly(acrylamide) with uniformly distributed colloidal spheres serving as cross-linkers, reinforcements, and Bragg reflectors. This colloidal-array cross-linked structure improved the mechanical strength and allowed the reversible tuning of structural color over a large spectral range. This work is shown in Fig. 39. The hydrogels exhibited exceptional stretchability, with stretching deformation capacity above 2800 % in the freshly prepared state and above 1900 % in the fully swollen state. They also demonstrated

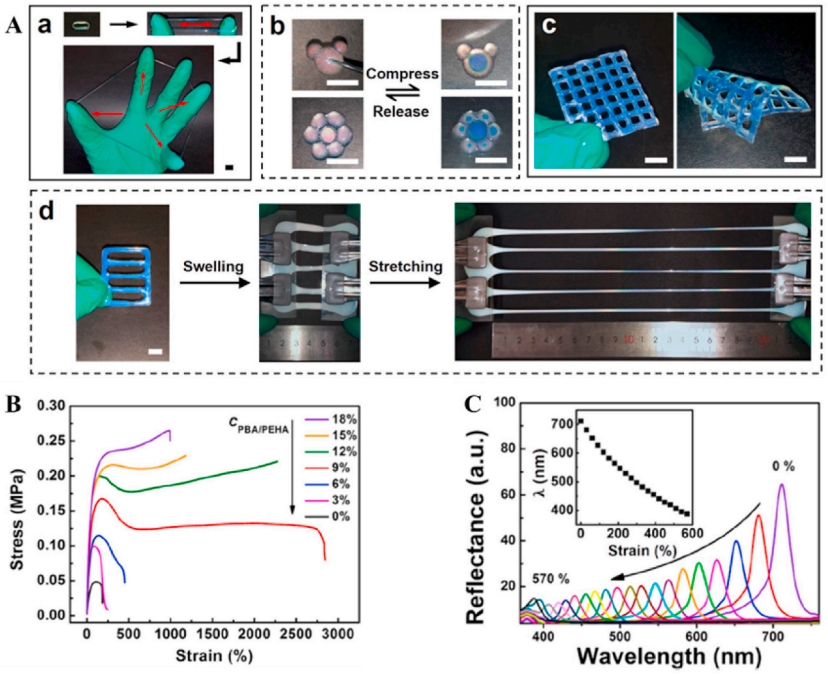

Fig. 39. (A) Direct ink writing of ACGs. (a) Handwritten ACG-12-38 ring showing high stretchability. (b) Handwritten ACG-12-38 patterns showing reversible mechanochromic behaviors (c) Printed flexible ACG-24-31 grid. (d) Fully swollen printed ACG-24-31 (B) tensile stress–strain curves of ACGs with different sphere concentrations (C) Normal incident reflectance spectra of fully swollen ACG-24-31 under different tensile strains (Chen et al. [211]).

augmented mechanical properties, with the PBA/PEHA spheres acting as physical cross-links and reinforcements, enabling high compression levels without breakage. The hydrogels possessed narrow reflectance peaks, allowing precise tuning of structural color, with reversible shifts in response to small compressive stress levels. In addition, they could be directly written into various shapes and patterns, highlighting their potential for customizable applications. The hydrogels offered a wide tunable range of the full-color spectrum, enabling reversible color changes in response to mechanical stress, as well as adaptability and responsiveness to external stimuli.

Dankoco et al. employed IJP to fabricate a silver-based thermistor on a polyimide substrate using a drop-on-demand Jetlab4 printer, shown in Fig. 40. Printing parameters were optimized to ensure consistent droplet formation and well-defined patterns, with printing performed at a jetting frequency of 400 Hz and a droplet velocity of approximately 4.5 m/s [212]. Precise dimensional control of the coating was achieved by adjusting pitch distances between droplets. The printed silver lines underwent a two-step thermal curing process, heating the substrate to 130 °C for 10 min followed by sintering at 150 °C for 30 min, resulting in a conductive silver film with a sheet resistance of 0.163 Ω/sq and a resistivity of 5.9 μΩ cm. The sensor design incorporated a meander pattern to improve sensitivity and linearity. Electrical functionality was evaluated using a 4-point probes method post-thermal curing, characterizing nominal resistance, sensitivity, linearity, and stability over time. The sensor exhibited a sensitivity of 2.19×10^{-3} °C^{-1} in the temperature range of 20–60 °C, with a nominal resistance of 2.032 kΩ at 38.5 °C. It demonstrated good linearity in response to temperature changes and hysteresis values within acceptable limits. Extended measurements over different days indicated the stability and reliability of the sensor over time. These findings suggested the potential of IJP thermistors for flexible sensor applications requiring accurate and reliable temperature monitoring.

Dua et al. employed IJP technology to fabricate rGO vapor sensors on poly(ethylene terephthalate) (PET) substrates [213]. The fabrication process, as shown in Fig. 41, involved depositing rGO ink, obtained from GO reduced by ascorbic acid, onto the PET substrates. IJP controlled the film thickness by adjusting parameters such as the number of passes and grayscale settings. Triton-X100 surfactant was used during dispersion to ensure uniformity, followed by sonication and washing in toluene to remove any residual surfactant, which resulted in a well-defined sensor structure with controlled dimensions. The structure of the IJP rGO film played an important role in its sensing properties. The structure of the film, characterized by high surface area due to two-dimensional sp2-bonded graphene sheets, Improved sensitivity to organic vapors. The thin rectangular strip design of the active sensor area enabled low-concentration vapor detection, ideal for applications requiring high sensitivity. Defects or functional groups on the rGO surface influenced its interaction with organic vapors and sensor response. X-ray photoelectron spectroscopy (XPS) data indicated the structural stability of the rGO film after exposure to harsh chemical environments like Cl_2 vapor.

The rGO sensor demonstrated high sensitivity to chemically aggressive vapors like NO_2 and Cl_2, showing a sharp increase in conductivity upon exposure. A linear relationship between vapor concentration and conductivity enabled the quantitative detection of organic vapors in parts per billion range. Also, the sensor exhibited selectivity towards electron-withdrawing vapors, distinguishing them from saturated organic vapors and NH_3. Reversible signal response and recovery upon exposure to vapors and subsequent UV irradiation highlighted the reusability and reliability of the sensor. Despite slow response and recovery times, UV exposure accelerated the recovery process. Slow signal recovery upon vapor removal was attributed to strong chemisorption, while UV light facilitated signal recovery without damaging the film or PET support, suggesting reversible physisorption. The sensor demonstrated stability under harsh chemical environments, reinforcing its long-term stability and performance.

4. Summary

Ink-based AM technologies, encompassing DIW, BJP, and IJP, are revolutionizing the fabrication of electrochemical devices, including fuel cells, catalyst scaffolds, batteries, supercapacitors, and sensors. The value of these technologies lies in their ability to control the "process-structure-properties" relationship.

The **"process"** aspect of these technologies involves the precise deposition of materials in predetermined patterns and structures. For DIW, this means the extrusion of a viscous ink through a nozzle, controlled in three dimensions to create structures layer by layer. BJP involves spreading a layer of powder material and selectively depositing a binder solution to form parts one layer at a time, while IJP deposits small droplets of ink with material of interest to create fine patterns. These processes are inherently flexible and can be

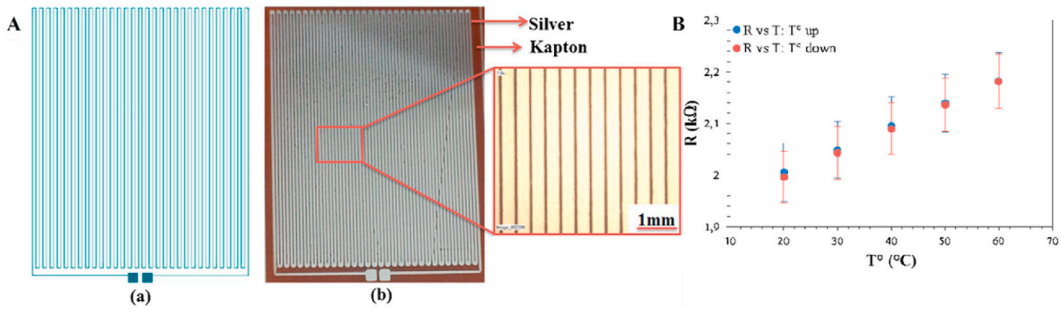

Fig. 40. (A) Photographs of (a) designed temperature sensor and (b) inkjet printed silver temperature sensor on Kapton substrate.(B) Resistance versus temperature over time of the printed temperature sensor(Dankoco et al. [212]).

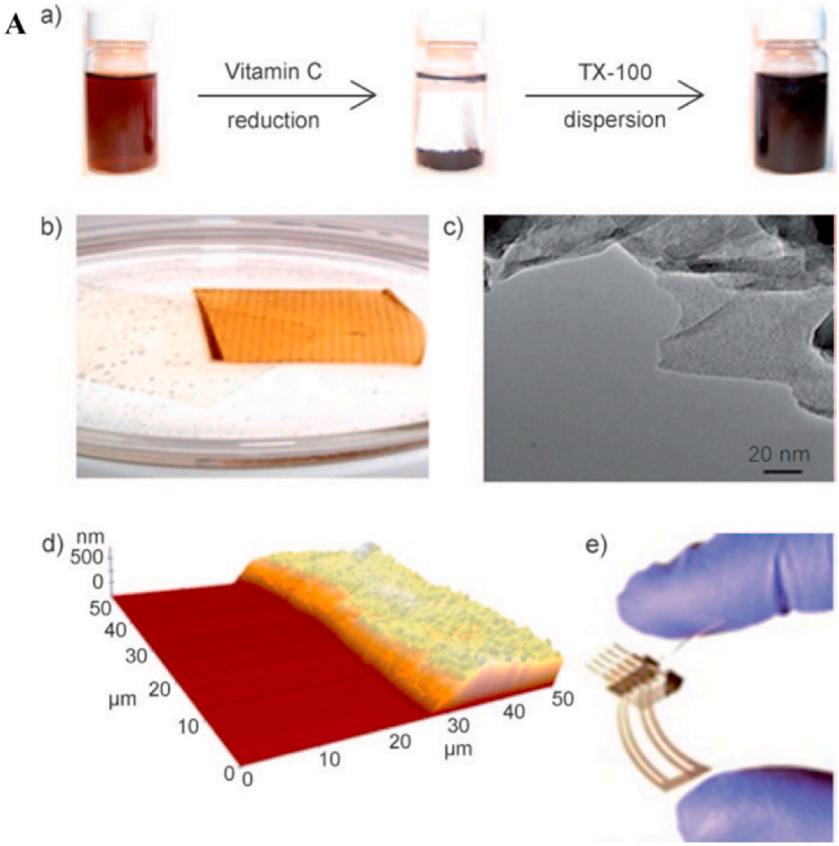

Fig. 41. (A) (a) Digital images of the vials containing GO and RGO dispersions. (b) IJP GO film lifts off the PET surface. (c) TEM image of the RGO powder. (d) AFM image of RGO film obtained by reduction of the film in (b) with ascorbic acid. (e) Digital image of IJP RGO/PET four-probe sensor (Dua et al. [213]).

adjusted in real time to suit specific material and design requirements, allowing for rapid prototyping and iteration. This flexibility is crucial in the R&D stage, where modifications are often necessary to optimize performance.

The **"structure"** that these AM processes create is important, especially considering the microarchitectures and surface geometries essential in electrochemical devices. For instance, the porosity, surface area, and pore size distribution can be finely tuned in catalyst scaffolds and electrodes for batteries and fuel cells. In fuel cells specifically, the complex architectures necessary for effective gas diffusion layers and catalyst layers can be directly fabricated, which can increase the material utilization efficiency and the reaction rate. Similarly, in batteries, the electrode structure can be optimized for ion transport and electronic conductivity, which will directly influence the capacity and cycling stability of the battery.

The **"properties"** of the electrochemical devices are directly influenced by the structures created through these printing techniques. By manipulating the microstructure, properties such as electrical conductivity, mechanical strength, and chemical reactivity can be tailored. In sensors, for example, the sensitivity and selectivity are greatly strengthened by creating structures that increase the effective surface area and promote interactions between the sensor material and the analyte. For supercapacitors, the high surface area and tailored pore size distribution of printed electrodes allow for greater energy storage per unit volume.

AM of these devices is particularly beneficial in solving the complex demands of modern electrochemical applications, where the performance is often limited by material and design constraints. By allowing for the microstructural features that determine the physical, chemical, and electrochemical properties of materials, ink-based AM techniques are critical in the iterative design and optimization process that is at the heart of developing next-generation electrochemical technologies. This capability significantly accelerates the development cycle, reduces costs, and ultimately leads to better-performing, more reliable, and more efficient electrochemical devices. Through such innovations, ink-based AM not only meets the technical requirements of modern applications but also contributes to broader sustainability goals by enhancing the efficiency and lifespan of devices critical to energy systems and environmental monitoring.

4.1. AM batteries

DIW and IJP revolutionize battery fabrication by offering precise material deposition with scalability and high resolution. These

methods enable intricate electrode structures with tailored properties, heightening battery performance across diverse applications. DIW utilizes an extrusion-based approach for layer-by-layer material deposition, facilitating the formation of complex electrode architectures with hierarchical porous structures. Parameters like printing path and ink concentration are finely tuned to control electrode structure and optimize electrochemical performance. One notable advantage of DIW is its ability to generate hierarchical porous structures within electrodes. These structures offer a high specific surface area, improving electrolyte-electrode interactions and ion transport, leading to upgraded battery performance. In addition, DIW enables the incorporation of additives like Super-P, improving conductivity and providing active sites for reactions, further boosting battery performance.

Similarly, IJP offers a non-contact printing method for precise material deposition at the microscale. This versatile technique allows for the fabrication of customized battery components with high resolution and uniformity, suitable for miniaturized devices like wearable biomedical devices. IJP facilitates the fabrication of quasi-solid-state lithium-ion batteries, achieving high capacities through precise deposition of printable inks for various battery components. Rheological optimization of inks ensures well-defined patterns without dispersion issues, leading to batteries with higher charge/discharge rates and stability. Modifying ink formulations and printing parameters refine electrode microstructure and electrochemical properties, resulting in higher discharge capacities and improved cycling stability. In addition, IJP facilitates the fabrication of lithium batteries. Tailoring printing parameters allow for the creation of electrodes with efficient Li^+ intercalation/deintercalation abilities and stable cycling performance. IJP also enables the fabrication of lithium-sulfur batteries with high capacities. By optimizing ink formulations and printing parameters, researchers can largely improve the properties of electrodes, boosting battery performance and reliability.

In summary, DIW and IJP offer advanced techniques for fabricating high-performance batteries with tailored structures and properties. These methods enable precise material deposition, enhancing battery performance for various applications, from portable electronic devices to energy storage systems. Important developments have been summarized in Table 3.

4.2. AM supercapacitors

Recent advances in supercapacitor technology are driven by breakthroughs in material science and sophisticated fabrication techniques, particularly DIW and IJP. This progression boosts the structural and electrochemical properties of supercapacitors, making them increasingly integral to applications ranging from portable electronics to large-scale energy systems.

Key to these advancements is the development of specialized conductive inks. Adjusting the rheological properties of these inks and refining the printing conditions allows for precision and scalability in production. And the architectures of these supercapacitors significantly influence their performance. Multi-layer structures, employing materials like polypyrrole nanotubes and GO, enable more efficient ion transport and energy efficiency. Further optimization is achieved through post-processing methods such as annealing, which refines the microstructures of electrodes to boost their electrical conductivity and durability. Flexibility and adaptability are also important, with innovations developing supercapacitors that maintain performance under physical stress, important for wearable technology. Important developments have been summarized in Table 4.

4.3. AM fuel cells

Recent advancements in SOFCs showcase the profound impact of sophisticated manufacturing processes on the structure and performance of these energy systems. AM offers unique advantages: BJP allows excellent control of porosity and layer structure, essential for optimizing gas diffusion and reactivity at the anode and cathode surfaces; DIW provides the precision necessary for achieving specific microstructures; IJP excels in depositing finely structured nanoparticle layers, ensuring uniformity and stability crucial for the functionality of anodes.

The structure of SOFCs is critically influenced by the chosen manufacturing technique and feedstock materials. The ability to control microstructural characteristics such as particle size distribution, porosity, and layer thickness directly impacts the efficiency and durability of the fuel cells. The goal of optimizing the process and structure of SOFCs is to fortify their properties, particularly in terms of conductivity, power density, and long-term operational stability. Properly controlled porosity promotes gas penetration and facilitates effective gas-solid reactions at the tri-phase boundary. Optimized electrode microstructures can reduce polarization resistance and improve peak power output, which will thereby ensure the longevity and reliability of the SOFCs. This is important for their commercial viability.

In essence, the interdependent relationship between process, structure, and properties in SOFC manufacturing emphasizes the

Table 3
Improved performance of ink-based 3D printed batteries via different processes, parameter changes, and structure.

Process	Material	Parameter	Structure	Performance Highlights
Direct ink writing	1. Graphene oxide ink 2. Quasi-solid-state lithium-ion batteries	Optimization of printable inks	1. Hierarchical porous structure electrode 2. Macro and microscale features 3. Complex structure	Improved discharge capacity
Inkjet printing	1. $LiFePO_4$ ink 2. $LiCoO_2$ ink	1. Varying pH values 2. Ink formulations 3. Printing parameters 4. Surface modification	1. Different particle size 2. Porous structure 3. Better dispersion 4. Surface modification	1. Improved electrical conductivity 2. Higher Specific capacities 3. Near 100 % charge-discharge efficiencies

Table 4
Improved performance of ink-based 3D printed supercapacitors via different processes, parameter changes, and structure.

Process	Material	Parameter	Structure	Performance Highlights
Direct ink writing	1. PEDOT: PSS, MXene nanosheets, and ethylene glycol (EG) 2. PEDOT: PSS 3. Polypyrrole nanotubes, graphene oxide, conductive carbon black 4. Graphene, cobalt ferrite nanoparticles, PVA binder 5. SW-CNT for electrodes, PVA-based gel electrolyte. 6. Activated carbon, PVA/H_3PO_4 electrolyte solution 7. $Ti_3C_2T_x$ MXene nanosheets, manganese dioxide nanowires, silver nanowires, fullerene	1. Rheology of ink 2. Shear-thinning behavior of ink 3. Printing speed 4. Temperature 5. Controlled flow 6. Loading of active material 7. Ion transport	1. Strengthened π–π coupling of PEDOT chains. 2. Interdigitated electrode structures 3. Multi-layer structure 4. Porous structure 5. Multi-cell supercapacitor arrays 6. Honeycomb-like	1. Higher capacitance, 2. Improved charge transport 3. Better cycling stability 4. Better energy density
Inkjet printing	1.Two-dimensional titanium carbide ($Ti_3C_2T_x$) MXene 2. Graphene oxide ink 3. GO and ammonium molybdate tetrahydrate inks, reduced to RGO/MoO_3 4. MnO_2 ink	1. High printing resolution 2. Annealing 3. Thermal treatment 4. finely control layer thickness	1. Close-contact structure 2. Connected graphene network 3. Connected graphene network 4. highly surface area and porosity	Better capacitance

complexity of material science in energy technology. As these AM techniques continue to evolve, they enable more control over the micro- and nanostructural elements of SOFCs, leading to significant improvements in performance. The ongoing R&D in this field not only improves our understanding of these relationships but also paves the way for the broader application of SOFC technology in sustainable energy solutions. Important developments have been summarized in Table 5.

4.4. AMcatalyst scaffolds

Recent research has delved into innovative approaches utilizing advanced printing technologies for catalyst scaffold fabrication, particularly in heterogeneous catalysis and electrocatalysis. Fabrication of scaffolds using BJP, can achieve high porosity by fine-tuning the ink composition and printing parameters, which is essential for catalysis performance. The reported works provided valuable insights into designing electrocatalysts for various applications by balancing reaction kinetics and selectivity through engineered architectures. Utilization of DIW technology to fabricate hierarchical porous structures demonstrated the potential in designing electrocatalysts with higher mass transport properties and catalytic efficiency.

Those AM methods and their uniqueness highlight the immense promise in the development of innovative catalyst materials and fabrication of catalyst scaffolds with tailored properties for various catalysis applications. Important developments have been summarized in Table 6.

4.5. AM sensors

DIW and IJP have emerged as important techniques in the fabrication of sensors due to their unique capabilities in material deposition and structural control. These advanced printing methods offer precise and versatile means to create sensor devices with tailored properties, enabling amplified performance across a wide range of applications. One of the key advantages of DIW and IJP lies in their ability to deposit functional materials with high precision onto various substrates. DIW achieved a uniform distribution of binder enhancing the surface roughness and available area for gas sensing. Optimizing the printing parameters of IJP ensures consistent droplet formation and well-defined patterns. This precise deposition of functional materials is essential for sensor fabrication as it directly influences the sensitivity and response of sensors.

Table 5
Improved performance ink-based 3D printed fuel cells via different processes, parameter changes, and structure.

Process	Material	Parameter	Structure	Performance Highlights
Binder jet printing	Ni-YSZ anode LSM-2 cathode YSZ electrolyte layers	Optimization of porosity	Controlled porosity	1. Advanced conductivity 2. Power density 3. Stability 4. Augmented catalytic activity
Direct ink writing	NiO-added ScSZ for the anode, LSM for the cathode	Optimization of ink viscosity	Hybrid ScSZ layer amplifying contact between layers	1. Peak power density 2. Reduced polarization resistance 3. Long-term stability
Inkjet printing	NiO nanoparticles NiO-SDC ink	1. Particle size 2. Dispersion 3. Sintering	1. Homogeneous coating 2. Bimodal distribution	1. Stability and efficiency 2. Augmented catalytic activity

Table 6
Improved ink-based 3D printed catalyst scaffold via different processes, parameter changes, and structure.

Process	Materials	Parameter	Structure	Performance Highlights
Binder jet printing	1. η- and γ- Al_2O_3 2. Pt/Al_2O_3 3. Cement-based materials with TiO_2 particle additions	1. Adjust ink composition 2. control the pore size distribution 3. adjust surface area 4. changing curing conductions	1. high porosity, controlled pore size distribution 2. complex channel geometries 3. particle size	1. Increased dehydrogenation rate 2. better increased dehydrogenation rate 3. enhanced photocatalytic activity
Direct ink writing	Ni meshes	1. Adjustment of ink viscosity 2. post-printing heat treatments 3. control of porosity	1. Controlled microstructure with optimized porosity and grain size 2. hierarchical structure	1. Excellent electrochemical performance for oxygen evolution reaction (OER) 2. robust mechanical properties for industrial applications
Inkjet printing	1. MoS_2-based electrocatalysts with Cu film support 2. Zirconium-based MOF thin films	1. Formulation of ink composition for stability 2. Control over film thickness and crystal size	1. Thin films with uniform morphology and controlled crystal size	1. High efficiency for hydrogen evolution reaction, 2. low overpotentials

Table 7
Improved performance of ink-based 3D printed sensor via different processes, parameter changes, and structure.

Process	Materials	Parameter Optimization	Structure Characteristics	Performance Highlights
Direct ink writing	1. Graphene-based ink 2. Poly(butyl acrylate) (PBA) spheres, poly(acrylamide), colloidal spheres	1. Controlled drying and heating 2. Ink formulation adjustment 3. Optimization of the swelling process	1. Graphene sheets draped over EC 2. Decreased surface roughness 3. Self-segregation of graphene 4. Uniformly distributed colloidal spheres	1. Gas sensing performance for CH_4 and H_2 2. Stretching deformation capacity 3. Wide tunable range of full-color spectrum
Inkjet printing	1. Silver-based thermistor on Polyimide substrate 2. Reduced graphene oxide on Poly(ethylene terephthalate) (PET) substrates	1. Optimization of jetting frequency and droplet velocity 2. Adjustment of ink deposition parameters	1. Consistent droplet formation and well-defined patterns 2. Uniform RGO film structure with high surface area	1. High sensitivity 2. Stability and reliability

With DIW, researchers can precisely control the deposition path and ink concentration, enabling the creation of intricate 3D structures layer-by-layer. On the other hand, IJP allows for the non-contact printing of materials, enabling the fabrication of sensors with high resolution and uniformity. Furthermore, DIW and IJP offer rapid prototyping capabilities, allowing for the efficient iteration and optimization of sensor designs. Researchers can easily adjust printing parameters and ink formulations to fine-tune sensor properties such as sensitivity, selectivity, and response time. This iterative process enables the rapid development of sensor prototypes and accelerates the translation of research findings into real-world applications. By systematically adjusting the printing parameters, they were able to fine-tune the electrical properties and achieve reliable performance under varying conditions. These advanced AM methods have the potential to revolutionize the field of sensor technology, enabling the development of next-generation sensing devices with performance and functionality. Important developments have been summarized in Table 7.

5. Challenges and Future Perspectives

The alignment of ink-based AM techniques with Industry 4.0 is perhaps most evident in its integration with digital tools and analytics. The use of digital models and the direct translation of these models into physical objects via AM embodies the digital-to-physical conversion at the heart of Industry 4.0. Furthermore, the integration of sensors and real-time monitoring in AM systems facilitates the collection of valuable data during the manufacturing process. This data can be analyzed using machine learning algorithms to predict and optimize print outcomes, reduce waste, and ensure quality control.

Despite its potential, the application of ink-based AM in the production of electrochemical devices faces several challenges. One of the main issues is the scalability of the technology for mass production, as the printing speeds and the size of the print beds may limit high-volume manufacturing, the long-term stability and repeatability of printed devices need to be validated through extensive testing. Also, the other chemicals in the inks (e.g. solvent, binder) may interact with the functional materials, which demands more research efforts. To solve these challenges, ongoing research is focused on boosting the speed and resolution of AM technologies, developing new ink feedstocks with improved performance characteristics, and integrating more robust quality control processes using AI and machine learning. By overcoming these hurdles, ink-based AM can not only fulfill its promise within electrochemical devices but also serve as a cornerstone technology in the broader context of Industry 4.0.

In conclusion, ink-based AM technologies offer a potent tool for the design and manufacture of advanced electrochemical devices, underpinned by the critical ‘process-structure-properties” relationship. The integration of these technologies with Industry 4.0 principles further improves their potential, setting a foundation for future innovations in energy technology and manufacturing practices. As these technologies continue to evolve, they will undoubtedly play an important role in shaping the future of both the energy sector and manufacturing at large.

CRediT authorship contribution statement

Runzhi Zhang: Writing – original draft, Investigation, Conceptualization. **Tao Sun:** Writing – review & editing, Supervision, Resources, Funding acquisition, Conceptualization.

Declaration of competing interest

The authors declare that they have no known competing financial interests or personal relationships that could have appeared to influence the work reported in this paper.

References

[1] R. Bogue, 3D printing: the dawn of a new era in manufacturing? Assemb. Autom. 33 (4) (2013) 307–311.
[2] H. Parmar, et al., Advanced robotics and additive manufacturing of composites: towards a new era in Industry 4.0, Mater. Manuf. Process. 37 (5) (2022) 483–517.
[3] R. Schlaepfer, M. Koch, P. Merkofer, Challenges and Solutions for the Digital Transformation and Use of Exponential Technologies, Deloitte, 2015.
[4] S. Roy, E. Andreou, Electroforming in the industry 4.0 era, Curr. Opin. Electrochem. 20 (2020) 108–115.
[5] A. Ambrosi, M. Pumera, 3D-printing technologies for electrochemical applications, Chem. Soc. Rev. 45 (10) (2016) 2740–2755.
[6] J. Cai, et al., Expediting the electrochemical kinetics of 3D-printed sulfur cathodes for Li–S batteries with high rate capability and areal capacity, Nano Energy 75 (2020) 104970.
[7] A. Pesce, et al., 3D printing the next generation of enhanced solid oxide fuel and electrolysis cells, J. Mater. Chem. A 8 (33) (2020) 16926–16932.
[8] A. Abdalla, B.A. Patel, 3D printed electrochemical sensors, Annu. Rev. Anal. Chem. 14 (2021) 47–63.
[9] D. Cogliati, et al., Intelligent cyber-physical systems for industry 4.0, in: 2018 First International Conference on Artificial Intelligence for Industries (AI4I), IEEE, 2018.
[10] M. Nagy, G. Lăzăroiu, K. Valaskova, Machine intelligence and autonomous robotic technologies in the corporate context of SMEs: deep learning and virtual simulation algorithms, cyber-physical production networks, and Industry 4.0-based manufacturing systems, Appl. Sci. 13 (3) (2023) 1681.
[11] I. Shin, M. Park, 3D printed conductive patterns based on laser irradiation, Phys. Status Solidi 214 (7) (2017) 1600943.
[12] R. Amin, et al., Electrochemical characterization of high energy density graphite electrodes made by freeze-casting, ACS Appl. Energy Mater. 1 (9) (2018) 4976–4981.
[13] H. Miyazaki, et al., Preparation and evaluation of LaNiO3 thin film electrode with chemical solution deposition, J. Eur. Ceram. Soc. 24 (6) (2004) 1005–1008.
[14] W. Yao, et al., Chemical deposition of platinum nanoparticles on iridium oxide for oxygen electrode of unitized regenerative fuel cell, Electrochem. Commun. 9 (5) (2007) 1029–1034.
[15] F. Wiesner, et al., Additive manufacturing of intertwined electrode pairs-guided mass transport with gyroids, Adv. Eng. Mater. 25 (1) (2023) 2200986.
[16] H. Peçenek, et al., Outstanding supercapacitor performance with intertwined flower-like NiO/MnO2/CNT electrodes, Mater. Res. Bull. 149 (2022) 111745.

[17] H. Li, et al., Intertwined carbon networks derived from Polyimide/Cellulose composite as porous electrode for symmetrical supercapacitor, J. Colloid Interface Sci. 609 (2022) 179–187.
[18] H. Hu, et al., Laser irradiation of electrode materials for energy storage and conversion, Matter 3 (1) (2020) 95–126.
[19] J. Cui, et al., Femtosecond laser irradiation of carbon nanotubes to metal electrodes, Appl. Sci. 9 (3) (2019) 476.
[20] L. Rassaei, P.S. Singh, S.G. Lemay, Lithography-based Nanoelectrochemistry, ACS Publications, 2011.
[21] W. Zhang, et al., Lignin laser lithography: a direct-write method for fabricating 3D graphene electrodes for microsupercapacitors, Adv. Energy Mater. 8 (27) (2018) 1801840.
[22] F. Zhang, et al., 3D printing technologies for electrochemical energy storage, Nano Energy 40 (2017) 418–431.
[23] O. Al-Ketan, R. Rowshan, R.K.A. Al-Rub, Topology-mechanical property relationship of 3D printed strut, skeletal, and sheet based periodic metallic cellular materials, Addit. Manuf. 19 (2018) 167–183.
[24] M. Kidambi, et al., Improving lithography throughput and minimizing waste using predictive multi-area scheduling, in: Metrology, Inspection, and Process Control for Microlithography, XXVI, SPIE, 2012.
[25] S.M.H. Ghazanfari, A. Zamanian, Phase transformation, microstructural and mechanical properties of hydroxyapatite/alumina nanocomposite scaffolds produced by freeze casting, Ceram. Int. 39 (8) (2013) 9835–9844.
[26] T.-M. Lee, et al., Color filter patterned by screen printing, Thin Solid Films 516 (21) (2008) 7875–7880.
[27] S.-F. Leung, et al., Roll-to-roll fabrication of large scale and regular arrays of three-dimensional nanospikes for high efficiency and flexible photovoltaics, Sci. Rep. 4 (1) (2014) 4243.
[28] S. Baek, Mathematical and Computational Models for Nanostructured Coating Using Electron Beam-Physical Vapor Deposition (EB-PVD), 2007.
[29] D.B. Hayden, Secondary Plasma Sources for Ionized Physical Vapor Deposition, University of Illinois at Urbana-Champaign, 1999.
[30] W. Swartout, R. Balzer, On the inevitable intertwining of specification and implementation, Commun. ACM 25 (7) (1982) 438–440.
[31] H. Zhou, et al., Synthesis of 3D printing materials and their electrochemical applications, Chin. Chem. Lett. 33 (8) (2022) 3681–3694.
[32] M.P. Browne, E. Redondo, M. Pumera, 3D printing for electrochemical energy applications, Chem. Rev. 120 (5) (2020) 2783–2810.
[33] A. Hu, et al., Optimizing redox reactions in aprotic lithium–sulfur batteries, Adv. Energy Mater. 10 (42) (2020) 2002180.
[34] D. Luo, et al., Surface-dominated sodium storage towards high capacity and ultrastable anode material for sodium-ion batteries, Adv. Funct. Mater. 28 (47) (2018) 1805371.
[35] Z. Zhu, et al., Highly stable and ultrafast electrode reaction of graphite for sodium ion batteries, J. Power Sources 293 (2015) 626–634.
[36] Y.X. Yin, et al., Lithium–sulfur batteries: electrochemistry, materials, and prospects, Angew. Chem. Int. Ed. 52 (50) (2013) 13186–13200.
[37] D. Kundu, et al., The emerging chemistry of sodium ion batteries for electrochemical energy storage, Angew. Chem. Int. Ed. 54 (11) (2015) 3431–3448.
[38] H. Jung, et al., Amorphous silicon anode for lithium-ion rechargeable batteries, J. Power Sources 115 (2) (2003) 346–351.
[39] C. Yan, et al., Toward critical electrode/electrolyte interfaces in rechargeable batteries, Adv. Funct. Mater. 30 (23) (2020) 1909887.
[40] W.B. Hawley, J. Li, Electrode manufacturing for lithium-ion batteries—analysis of current and next generation processing, J. Energy Storage 25 (2019) 100862.
[41] N. Verdier, et al., Challenges in solvent-free methods for manufacturing electrodes and electrolytes for lithium-based batteries, Polymers 13 (3) (2021) 323.
[42] V. Deimede, C. Elmasides, Separators for lithium-ion batteries: a review on the production processes and recent developments, Energy Technol. 3 (5) (2015) 453–468.
[43] L. Zolin, et al., An innovative process for ultra-thick electrodes elaboration: toward low-cost and high-energy batteries, Energy Technol. 7 (5) (2019) 1900025.
[44] M. Areir, et al., Development of 3D printing technology for the manufacture of flexible electric double-layer capacitors, Mater. Manuf. Process. 33 (8) (2018) 905–911.
[45] R. Burt, G. Birkett, X. Zhao, A review of molecular modelling of electric double layer capacitors, Phys. Chem. Chem. Phys. 16 (14) (2014) 6519–6538.
[46] D.D. Potphode, L. Sinha, P.M. Shirage, Redox additive enhanced capacitance: multi-walled carbon nanotubes/polyaniline nanocomposite based symmetric supercapacitors for rapid charge storage, Appl. Surf. Sci. 469 (2019) 162–172.
[47] J. Yeo, et al., Flexible supercapacitor fabrication by room temperature rapid laser processing of roll-to-roll printed metal nanoparticle ink for wearable electronics application, J. Power Sources 246 (2014) 562–568.
[48] S. Kang, et al., Roll-to-roll laser-printed graphene–graphitic carbon electrodes for high-performance supercapacitors, ACS Appl. Mater. Interfaces 10 (1) (2018) 1033–1038.
[49] S. Lehtimäki, et al., Performance, stability and operation voltage optimization of screen-printed aqueous supercapacitors, Sci. Rep. 7 (1) (2017) 46001.
[50] T. Pereira, J.V. Kennedy, J. Potgieter, A comparison of traditional manufacturing vs additive manufacturing, the best method for the job, Procedia Manuf. 30 (2019) 11–18.
[51] K. Choy, Chemical vapour deposition of coatings, Prog. Mater. Sci. 48 (2) (2003) 57–170.
[52] S. Mekhilef, R. Saidur, A. Safari, Comparative study of different fuel cell technologies, Renew. Sustain. Energy Rev. 16 (1) (2012) 981–989.
[53] J. Larminie, A. Dicks, M.S. McDonald, Fuel Cell Systems Explained, vol. 2, J. Wiley, Chichester, UK, 2003.
[54] K. Rajashekara, A.K. Rathore, Power conversion and control for fuel cell systems in transportation and stationary power generation, in: Renewable Energy Devices and Systems with Simulations in MATLAB® and ANSYS®, CRC Press, 2017, pp. 291–318.
[55] S. Cleghorn, et al., PEM fuel cells for transportation and stationary power generation applications, Int. J. Hydrogen Energy 22 (12) (1997) 1137–1144.
[56] K. Karacan, et al., Investigation of formability of metallic bipolar plates via stamping for light-weight PEM fuel cells, Int. J. Hydrogen Energy 45 (60) (2020) 35149–35161.
[57] Y. Zhang, et al., Modifying the electrode-electrolyte interface of anode supported solid oxide fuel cells (SOFCs) by laser-machining, Energy Convers. Manag. 171 (2018) 1030–1037.
[58] H. Lee, et al., Evaluation of graphite composite bipolar plate for PEM (proton exchange membrane) fuel cell: electrical, mechanical, and molding properties, J. Mater. Process. Technol. 187 (2007) 425–428.
[59] Z. Chen, et al., A review on non-precious metal electrocatalysts for PEM fuel cells, Energy Environ. Sci. 4 (9) (2011) 3167–3192.
[60] J. Zhang, X. Zhao, On the configuration of supercapacitors for maximizing electrochemical performance, ChemSusChem 5 (5) (2012) 818–841.
[61] Y. Lu, et al., Advanced low-temperature solid oxide fuel cells based on a built-in electric field, Energy Mater 1 (2022) 100007.
[62] C. Andrieux, J. Dumas-Bouchiat, J. Savéant, Homogeneous redox catalysis of electrochemical reactions: Part IV. Kinetic controls in the homogeneous process as characterized by stationary and quasi-stationary electrochemical techniques, J. Electroanal. Chem. Interfacial Electrochem. 113 (1) (1980) 1–18.
[63] X. Mao, et al., Electrochemically responsive heterogeneous catalysis for controlling reaction kinetics, J. Am. Chem. Soc. 137 (3) (2015) 1348–1355.
[64] C. Spöri, et al., The stability challenges of oxygen evolving catalysts: towards a common fundamental understanding and mitigation of catalyst degradation, Angew. Chem. Int. Ed. 56 (22) (2017) 5994–6021.
[65] T. Liu, et al., Enhanced electrocatalysis for energy-efficient hydrogen production over CoP catalyst with nonelectroactive Zn as a promoter, Adv. Energy Mater. 7 (15) (2017) 1700020.
[66] Y. Zhou, et al., Enhancement of Pt and Pt-alloy fuel cell catalyst activity and durability via nitrogen-modified carbon supports, Energy Environ. Sci. 3 (10) (2010) 1437–1446.
[67] M.R. DuBois, Catalytic applications of transition-metal complexes with sulfide ligands, Chem. Rev. 89 (1) (1989) 1–9.
[68] D. Liu, et al., 3D printing of metal-organic frameworks decorated hierarchical porous ceramics for high-efficiency catalytic degradation, Chem. Eng. J. 397 (2020) 125392.
[69] A.D. Salazar-Aguilar, et al., Iron-based metal-organic frameworks integrated into 3D printed ceramic architectures, Open Ceramics 5 (2021) 100047.
[70] H.V. Doan, et al., Hierarchical metal–organic frameworks with macroporosity: synthesis, achievements, and challenges, Nano-Micro Lett. 11 (2019) 1–33.
[71] X. Liu, et al., Two-dimensional black phosphorus and graphene oxide nanosheets synergistically enhance cell proliferation and osteogenesis on 3D printed scaffolds, ACS Appl. Mater. Interfaces 11 (26) (2019) 23558–23572.

[72] V. Middelkoop, et al., 3D printed Ni/Al2O3 based catalysts for CO2 methanation-a comparative and operando XRD-CT study, J. CO2 Util. 33 (2019) 478–487.
[73] Y. Zhang, et al., Operando spectroscopic study of dynamic structure of iron oxide catalysts during CO2 hydrogenation, ChemCatChem 10 (6) (2018) 1272–1276.
[74] A.I. Osman, et al., Biofuel production, hydrogen production and water remediation by photocatalysis, biocatalysis and electrocatalysis, Environ. Chem. Lett. 21 (3) (2023) 1315–1379.
[75] H. Yi, et al., Synergistic effect of artificial enzyme and 2D nano-structured Bi2WO6 for eco-friendly and efficient biomimetic photocatalysis, Appl. Catal. B Environ. 250 (2019) 52–62.
[76] S. Fukuzumi, D. Hong, Homogeneous versus heterogeneous catalysts in water oxidation, Eur. J. Inorg. Chem. 2014 (4) (2014) 645–659.
[77] M.J. Climent, A. Corma, S. Iborra, Homogeneous and heterogeneous catalysts for multicomponent reactions, RSC Adv. 2 (1) (2012) 16–58.
[78] L. Liu, et al., Metal-free carbonaceous materials as promising heterogeneous catalysts, ChemCatChem 7 (18) (2015) 2765–2787.
[79] Y.-B. Huang, et al., Multifunctional metal–organic framework catalysts: synergistic catalysis and tandem reactions, Chem. Soc. Rev. 46 (1) (2017) 126–157.
[80] A. Sandoval, et al., Bimetallic Au–Ag/TiO2 catalyst prepared by deposition–precipitation: high activity and stability in CO oxidation, J. Catal. 281 (1) (2011) 40–49.
[81] J.-H. Shim, G.-J. Lee, Y.W. Cho, Reaction products between TiCl3 catalyst and Li3AlH6 during mechanical mixing, J. Alloys Compd. 419 (1–2) (2006) 176–179.
[82] N. Mota, et al., Direct synthesis of dimethyl ether from CO2: recent advances in bifunctional/hybrid catalytic systems, Catalysts 11 (4) (2021) 411.
[83] J. Lu, J.W. Elam, P.C. Stair, Synthesis and stabilization of supported metal catalysts by atomic layer deposition, Accounts Chem. Res. 46 (8) (2013) 1806–1815.
[84] J.A. Singh, N. Yang, S.F. Bent, Nanoengineering heterogeneous catalysts by atomic layer deposition, Annu. Rev. Chem. Biomol. Eng. 8 (2017) 41–62.
[85] Z. Zhang, et al., Electrochemical deposition as a universal route for fabricating single-atom catalysts, Nat. Commun. 11 (1) (2020) 1215.
[86] Y. Wang, et al., Cu2O nano-flowers/graphene enabled scaffolding structure catalyst layer for enhanced CO2 electrochemical reduction, Appl. Catal. B Environ. 305 (2022) 121022.
[87] Y. Kwon, S. Kang, J. Bae, Development of a PrBaMn2O5+ δ-La0. 8Sr0. 2Ga0. 85Mg0. 15O3-δ composite electrode by scaffold infiltration for reversible solid oxide fuel cell applications, Int. J. Hydrogen Energy 45 (3) (2020) 1748–1758.
[88] B.J. Privett, J.H. Shin, M.H. Schoenfisch, Electrochemical sensors, Anal. Chem. 80 (12) (2008) 4499–4517.
[89] J.H. Haertel, G.F. Nellis, A fully developed flow thermofluid model for topology optimization of 3D-printed air-cooled heat exchangers, Appl. Therm. Eng. 119 (2017) 10–24.
[90] W. Sixel, et al., Ceramic 3D printed direct winding heat exchangers for improving electric machine thermal management, in: 2019 IEEE Energy Conversion Congress and Exposition (ECCE), IEEE, 2019.
[91] T. Dixit, et al., High performance, microarchitected, compact heat exchanger enabled by 3D printing, Appl. Therm. Eng. 210 (2022) 118339.
[92] R.l.A. Márquez-Montes, et al., Electrochemical engineering assessment of a novel 3D-printed filter-press electrochemical reactor for multipurpose laboratory applications, ACS Sustain. Chem. Eng. 8 (9) (2020) 3896–3905.
[93] D.M. Heard, S. Doobary, A.J. Lennox, 3D printed reactionware for synthetic electrochemistry with hydrogen fluoride reagents, Chemelectrochem 8 (11) (2021) 2070–2074.
[94] J. Muñoz, E. Redondo, M. Pumera, Versatile design of functional organic–inorganic 3D-printed (opto) electronic interfaces with custom catalytic activity, Small 17 (41) (2021) 2103189.
[95] G.D. O'Neil, et al., Single-step fabrication of electrochemical flow cells utilizing multi-material 3D printing, Electrochem. Commun. 99 (2019) 56–60.
[96] P. Zhang, et al., A crack healable syntactic foam reinforced by 3D printed healing-agent based honeycomb, Compos. B Eng. 151 (2018) 25–34.
[97] J. Lv, H. Shen, J. Fu, Fabrication of multi-functional Ni–Ti alloys by laser powder bed fusion, Int. J. Adv. Des. Manuf. Technol. (2022) 1–9.
[98] J. Skelton, et al., Efficacy of elemental mixing of in situ alloyed Al-33wt% Cu during laser powder bed fusion, J. Mater. Process. Technol. 299 (2022) 117379.
[99] L. Rabinskiy, et al., Fabrication of porous silicon nitride ceramics using binder jetting technology, in: IOP Conference Series: Materials Science and Engineering, IOP Publishing, 2016.
[100] E. Stevens, et al., Mastering a 1.2 K hysteresis for martensitic para-ferromagnetic partial transformation in Ni-Mn (Cu)-Ga magnetocaloric material via binder jet 3D printing, Addit. Manuf. 37 (2021) 101560.
[101] A. Mostafaei, et al., Effect of binder saturation and drying time on microstructure and resulting properties of sinter-HIP binder-jet 3D-printed WC-Co composites, Addit. Manuf. 46 (2021) 102128.
[102] E.M. Wilts, et al., Comparison of linear and 4-arm star poly (vinyl pyrrolidone) for aqueous binder jetting additive manufacturing of personalized dosage tablets, ACS Appl. Mater. Interfaces 11 (27) (2019) 23938–23947.
[103] R. Jiang, et al., Influence of powder type and binder saturation on binder jet 3D–printed and sintered Inconel 625 samples, Int. J. Adv. Des. Manuf. Technol. 116 (2021) 3827–3838.
[104] M. Mariani, et al., Tailoring α-alumina powder morphology through spray drying for cold consolidation by binder jetting, Open Ceramics 12 (2022) 100307.
[105] A. Mostafaei, Powder Bed Binder Jet 3D Printing of Alloy 625: Microstructural Evolution, Densification Kinetics and Mechanical Properties, University of Pittsburgh, 2018.
[106] H. Miyanaji, et al., Effect of fine powder particles on quality of binder jetting parts, Addit. Manuf. 36 (2020) 101587.
[107] S. Wu, et al., Study on powder particle behavior in powder spreading with discrete element method and its critical implications for binder jetting additive manufacturing processes, Virtual Phys. Prototyp. 18 (1) (2023) e2158877.
[108] D. Karlsson, et al., Binder jetting of the AlCoCrFeNi alloy, Addit. Manuf. 27 (2019) 72–79.
[109] P. Yadav, et al., Binder jetting 3D printing of titanium aluminides based materials: a feasibility study, Adv. Eng. Mater. 22 (9) (2020) 2000408.
[110] Q. Porter, Z. Pei, C. Ma, Binder jetting and infiltration of metal matrix nanocomposites, J. Manuf. Sci. Eng. 144 (7) (2022) 074502.
[111] A. Mostafaei, et al., Binder jet 3D printing—process parameters, materials, properties, modeling, and challenges, Prog. Mater. Sci. 119 (2021) 100707.
[112] F. Liravi, M. Vlasea, Powder bed binder jetting additive manufacturing of silicone structures, Addit. Manuf. 21 (2018) 112–124.
[113] N.B. Crane, Impact of part thickness and drying conditions on saturation limits in binder jet additive manufacturing, Addit. Manuf. 33 (2020) 101127.
[114] M. Li, et al., Binder jetting additive manufacturing: observations of compaction-induced powder bed surface defects, Manufacturing Letters 28 (2021) 50–53.
[115] G. Cheng, et al., Electrospun carbon nanofiber inlaid with tungsten carbide nanoparticle by in-situ carbothermal reaction as bifunctional electrode for vanadium redox flow battery, Electrochim. Acta 362 (2020) 137178.
[116] K. Sen, et al., Pharmaceutical applications of powder-based binder jet 3D printing process–a review, Adv. Drug Deliv. Rev. 177 (2021) 113943.
[117] M. Moghadasi, et al., Ceramic binder jetting additive manufacturing: effects of particle size on feedstock powder and final part properties, Ceram. Int. 46 (10) (2020) 16966–16972.
[118] Z. Feng, et al., 3D printed Sm-doped ceria composite electrolyte membrane for low temperature solid oxide fuel cells, Int. J. Hydrogen Energy 44 (26) (2019) 13843–13851.
[119] P. Theodosiou, J. Greenman, I.A. Ieropoulos, Developing 3D-printable cathode electrode for monolithically printed microbial fuel cells (MFCs), Molecules 25 (16) (2020) 3635.
[120] K.-E. Guima, et al., Harvesting energy from an organic pollutant model using a new 3D-printed microfluidic photo fuel cell, ACS Appl. Mater. Interfaces 12 (49) (2020) 54563–54572.
[121] B. Bian, et al., 3D printed porous carbon anode for enhanced power generation in microbial fuel cell, Nano Energy 44 (2018) 174–180.
[122] S. Masciandaro, et al., Three-dimensional printed yttria-stabilized zirconia self-supported electrolytes for solid oxide fuel cell applications, J. Eur. Ceram. Soc. 39 (1) (2019) 9–16.
[123] M.K. Rath, et al., Development of highly efficient and durable large-area solid oxide fuel cell by a direct-ink-writing three-dimensional printer, J. Power Sources 552 (2022) 232225.
[124] B. Bian, et al., Application of 3D printed porous copper anode in microbial fuel cells, Front. Energy Res. 6 (2018) 50.

[125] F.J. Hackemüller, et al., Manufacturing of large-scale titanium-based porous transport layers for polymer electrolyte membrane electrolysis by tape casting, Adv. Eng. Mater. 21 (6) (2019) 1801201.
[126] M. Vaezi, S. Yang, Extrusion-based additive manufacturing of PEEK for biomedical applications, Virtual Phys. Prototyp. 10 (3) (2015) 123–135.
[127] M. Vaezi, et al., Extrusion-based 3D printing technologies for 3D scaffold engineering, in: Functional 3D Tissue Engineering Scaffolds, Elsevier, 2018, pp. 235–254.
[128] X. Montero, M.C. Galetz, M. Schütze, A novel type of environmentally friendly slurry coatings, Jom 67 (2015) 77–86.
[129] P. Zhao, et al., Self-limiting chemical vapor deposition growth of monolayer graphene from ethanol, J. Phys. Chem. C 117 (20) (2013) 10755–10763.
[130] L. Arenas, C.P. de León, F. Walsh, 3D-printed porous electrodes for advanced electrochemical flow reactors: a Ni/stainless steel electrode and its mass transport characteristics, Electrochem. Commun. 77 (2017) 133–137.
[131] I. Jang, et al., Predicting optimal geometries of 3D-printed solid oxide electrochemical reactors, Electrochim. Acta 427 (2022) 140902.
[132] K.M. Fashalameh, Z. Sadeghian, R. Ebrahimi, A high-performance planar anode-supported solid oxide fuel cell with hierarchical porous structure through slurry-based three-dimensional printing, J. Alloys Compd. 916 (2022) 165406.
[133] Y. Paik, S.S. Kim, O.H. Han, Methanol behavior in direct methanol fuel cells, Angew. Chem. 120 (1) (2008) 100–102.
[134] A.S. Aricò, V. Baglio, V. Antonucci, Direct methanol fuel cells: history, status and perspectives, Electrocatalysis of direct methanol fuel cells (2009) 1–78.
[135] A. Blum, et al., Water-neutral micro direct-methanol fuel cell (DMFC) for portable applications, J. Power Sources 117 (1–2) (2003) 22–25.
[136] J. Dailly, M. Ancelin, M. Marrony, Long term testing of BCZY-based protonic ceramic fuel cell PCFC: micro-generation profile and reversible production of hydrogen and electricity, Solid State Ionics 306 (2017) 69–75.
[137] Z. Li, et al., Effects of cathode thickness and microstructural properties on the performance of protonic ceramic fuel cell (PCFC): a 3D modelling study, Int. J. Hydrogen Energy 47 (6) (2022) 4047–4061.
[138] Z. Li, et al., Ethylene and power cogeneration from proton ceramic fuel cells (PCFC): a thermo-electrochemical modelling study, J. Power Sources 536 (2022) 231503.
[139] S. Terada, et al., Stability of LiAlO2 as electrolyte matrix for molten carbonate fuel cells, J. Power Sources 75 (2) (1998) 223–229.
[140] E. Antolini, The stability of LiAlO2 powders and electrolyte matrices in molten carbonate fuel cell environment, Ceram. Int. 39 (4) (2013) 3463–3478.
[141] H.-J. Choi, et al., Fabrication and performance evaluation of electrolyte-combined α-LiAlO2 matrices for molten carbonate fuel cells, Int. J. Hydrogen Energy 36 (17) (2011) 11048–11055.
[142] K. Huang, J. Wan, J.B. Goodenough, Oxide-ion conducting ceramics for solid oxide fuel cells, J. Mater. Sci. 36 (2001) 1093–1098.
[143] A.M. Hussain, et al., Stannate-based ceramic oxide as anode materials for oxide-ion conducting low-temperature solid oxide fuel cells, J. Electrochem. Soc. 163 (10) (2016) F1198.
[144] S. Sun, Z. Cheng, H2S poisoning of proton conducting solid oxide fuel cell and comparison with conventional oxide-ion conducting solid oxide fuel cell, J. Electrochem. Soc. 165 (10) (2018) F836.
[145] R.M. Manglik, Y.N. Magar, Heat and mass transfer in planar anode-supported solid oxide fuel cells: effects of interconnect fuel/oxidant channel flow cross section, J. Therm. Sci. Eng. Appl. 7 (4) (2015).
[146] S. Badwal, Stability of solid oxide fuel cell components, Solid State Ionics 143 (1) (2001) 39–46.
[147] A. Tarancón, Strategies for lowering solid oxide fuel cells operating temperature, Energies 2 (4) (2009) 1130–1150.
[148] G. Manogharan, M. Kioko, C. Linkous, Binder jetting: a novel solid oxide fuel-cell fabrication process and evaluation, Jom 67 (2015) 660–667.
[149] S. Zhao, et al., Advances in Sn-based catalysts for electrochemical CO 2 reduction, Nano-Micro Lett. 11 (2019) 1–19.
[150] O. Aaboubi, et al., Ni–Mn based alloys as versatile catalyst for different electrochemical reactions, J. Power Sources 269 (2014) 597–607.
[151] Z. Lu, et al., Lithium electrochemical tuning for electrocatalysis, Adv. Mater. 30 (48) (2018) 1800978.
[152] H. Zhang, B.N. Kim, K. Morita, H. Yoshida Keijiro Hiraga, Y. Sakka, Effect of sintering temperature on optical properties and microstructure of translucent zirconia prepared by high-pressure spark plasma sintering, Sci. Technol. Adv. Mater. 12 (5) (2011) 055003.
[153] B.-Y. Li, L.-J. Rong, Y.-Y. Li, Porous NiTi alloy prepared from elemental powder sintering, J. Mater. Res. 13 (10) (1998) 2847–2851.
[154] P. Monash, G. Pugazhenthi, Development of ceramic supports derived from low-cost raw materials for membrane applications and its optimization based on sintering temperature, Int. J. Appl. Ceram. Technol. 8 (1) (2011) 227–238.
[155] H. Wang, et al., Preparation of a high-precision gama-Al2O3 structured catalyst by DLP 3D direct printing for hydrogen production from methanol, Ind. Eng. Chem. Res. 60 (35) (2021) 13107–13114.
[156] M. Arslan, et al., Effect of Al2O3 support on Co-based SiO2 core–shell catalysts for fischer–tropsch synthesis in 3D printed SS microchannel microreactor, Top. Catal. (2022) 1–21.
[157] M. Eickenscheidt, et al., 3D-printed hermetic alumina housings, Materials 14 (1) (2021) 200.
[158] M. Konarova, et al., Enabling process intensification by 3 D printing of catalytic structures, ChemCatChem 9 (21) (2017) 4132–4138.
[159] J. Liu, et al., Evaluation of the mechanical and photocatalytic properties of TiO2-reinforced cement-based materials in binder jet 3D printing, J. Build. Eng. 72 (2023) 106618.
[160] H.M. Bui, et al., Development of a manufacturing process for Binder Jet 3D printed porous Al2O3 supports used in heterogeneous catalysis, Addit. Manuf. 50 (2022).
[161] Bui, H.M., et al., Comparison of Direct Ink Writing and Binder Jetting for Additive Manufacturing of Pt/Al2o3 Catalysts for the Dehydrogenation of Perhydro-Dibenzyltoluene. Available at: SSRN 4197757.
[162] T. Ludwig, et al., Additive manufacturing of Al2O3-based carriers for heterogeneous catalysis, Chem. Ing. Tech. 90 (5) (2018) 703–707.
[163] A. Lind, et al., Multi-purpose structured catalysts designed and manufactured by 3D printing, Mater. Des. 187 (2020) 108377.
[164] M. Saadi, et al., Direct ink writing: a 3D printing technology for diverse materials, Adv. Mater. 34 (28) (2022) 2108855.
[165] S.-S. Li, et al., Preparation of laminated Cr3C2/Cu composites by direct ink writing and pressureless infiltration, Addit. Manuf. 59 (2022) 103189.
[166] M.M. Ovhal, N. Kumar, J.-W. Kang, 3D direct ink writing fabrication of high-performance all-solid-state micro-supercapacitors, Mol. Cryst. Liq. Cryst. 705 (1) (2020) 105–111.
[167] Q. Zheng, et al., A systematic printability study of direct ink writing towards high-resolution rapid manufacturing, Int. J. Extrem. Manuf. 5 (3) (2023) 035002.
[168] U. Golcha, A. Praveen, D.B. Paul, Direct ink writing of ceramics for bio medical applications–A Review, in: IOP Conference Series: Materials Science and Engineering, IOP Publishing, 2020.
[169] S. Waheed, et al., 3D printed microfluidic devices: enablers and barriers, Lab Chip 16 (11) (2016) 1993–2013.
[170] R. Seyedmahmoud, M. Messler, E. Loboa, 3D bioprinting technologies for tissue engineering: a mini review, HSOA Journal of Stem Cells Research Development Therapy 6 (2020).
[171] Y. Wu, et al., Research progress on the application of inkjet printing technology combined with hydrogels, Appl. Mater. Today 36 (2024) 102036.
[172] Z. Liu, et al., Direct ink writing of Li1. 3Al0. 3Ti1. 7 (PO4) 3-based solid-state electrolytes with customized shapes and remarkable electrochemical behaviors, Small 17 (6) (2021) 2002866.
[173] Q. Li, et al., Direct ink writing (DIW) of graphene aerogel composite electrode for vanadium redox flow battery, J. Power Sources 542 (2022) 231810.
[174] J. Bae, et al., High-performance, printable quasi-solid-state electrolytes toward all 3D direct ink writing of shape-versatile Li-ion batteries, Energy Storage Mater. 57 (2023) 277–288.
[175] J. Zhao, et al., Direct ink writing of adjustable electrochemical energy storage device with high gravimetric energy densities, Adv. Funct. Mater. 29 (26) (2019) 1900809.
[176] A. Alam, et al., Sonochemical synthesis of welded titanium dioxide-silver nanocomposite as a 3-dimensional direct ink writing printed cathode electrode material for high-performance supercapacitor, J. Energy Storage 45 (2022) 103524.
[177] M. Cheng, et al., Direct ink writing of polymer composite electrolytes with enhanced thermal conductivities, Adv. Funct. Mater. 31 (4) (2021) 2006683.

[178] Junho Bae, et al., High-performance, printable quasi-solid-state electrolytes toward all 3D direct ink writing of shape-versatile Li-ion batteries, Energy Storage Mater. 57 (2023) 277–288.
[179] Y. Gu, et al., Fabrication of rechargeable lithium ion batteries using water-based inkjet printed cathodes, J. Manuf. Process. 20 (2015) 198–205.
[180] P.-E. Delannoy, et al., Ink-jet printed porous composite LiFePO4 electrode from aqueous suspension for microbatteries, J. Power Sources 287 (2015) 261–268.
[181] J.-H. Lee, et al., Strategic dispersion of carbon black and its application to ink-jet-printed lithium cobalt oxide electrodes for lithium ion batteries, J. Power Sources 196 (15) (2011) 6449–6455.
[182] J. Huang, et al., Electrochemical properties of LiCoO2 thin film electrode prepared by ink-jet printing technique, Thin Solid Films 516 (10) (2008) 3314–3319.
[183] C.A. Milroy, et al., Inkjet-printed lithium–sulfur microcathodes for all-printed, integrated nanomanufacturing, Small 13 (11) (2017) 1603786.
[184] S. Jha, et al., Additively manufactured electrodes for supercapacitors: a review, Appl. Mater. Today 26 (2022) 101220.
[185] X. Li, et al., 3D-printed stretchable micro-supercapacitor with remarkable areal performance, Adv. Energy Mater. 10 (14) (2020) 1903794.
[186] F. Lai, et al., Three-phase boundary in cross-coupled micro-mesoporous networks enabling 3D-printed and ionogel-based quasi-solid-state micro-supercapacitors, Adv. Mater. 32 (40) (2020) 2002474.
[187] W. Zong, et al., Recent advances and perspectives of 3D printed micro-supercapacitors: from design to smart integrated devices, Chem. Commun. 58 (13) (2022) 2075–2095.
[188] C. Yang, et al., 3D printed template-assisted assembly of additive-free Ti3C2T x MXene microlattices with customized structures toward high areal capacitance, ACS Nano 16 (2) (2022) 2699–2710.
[189] L. Yu, et al., 3D printing of NiCoP/Ti 3 C 2 MXene architectures for energy storage devices with high areal and volumetric energy density, Nano-Micro Lett. 12 (2020) 1–13.
[190] C. Zhang, et al., Stamping of flexible, coplanar micro-supercapacitors using MXene inks, Adv. Funct. Mater. 28 (9) (2018) 1705506.
[191] L. Li, et al., Direct-ink-write 3D printing of programmable micro-supercapacitors from MXene-regulating conducting polymer inks, Adv. Energy Mater. 13 (9) (2023) 2203683.
[192] K. Wu, et al., Direct ink writing of PEDOT: PSS inks for flexible micro-supercapacitors, J. Ind. Eng. Chem. 123 (2023) 272–277.
[193] Y. Zhang, et al., All-printed solid-state substrate-versatile and high-performance micro-supercapacitors for in situ fabricated transferable and wearable energy storage via multi-material 3D printing, J. Power Sources 403 (2018) 109–117.
[194] D.T. Tung, et al., Direct ink writing of graphene–cobalt ferrite hybrid nanomaterial for supercapacitor electrodes, J. Electron. Mater. 49 (2020) 4671–4679.
[195] B. Chen, et al., Fully packaged carbon nanotube supercapacitors by direct ink writing on flexible substrates, ACS Appl. Mater. Interfaces 9 (34) (2017) 28433–28440.
[196] M. Idrees, et al., 3D printed supercapacitor using porous carbon derived from packaging waste, Addit. Manuf. 36 (2020) 101525.
[197] A. Sajedi-Moghaddam, E. Rahmanian, N. Naseri, Inkjet-printing technology for supercapacitor application: current state and perspectives, ACS Appl. Mater. Interfaces 12 (31) (2020) 34487–34504.
[198] C. Zhang, et al., Additive-free MXene inks and direct printing of micro-supercapacitors, Nat. Commun. 10 (1) (2019) 1795.
[199] M.H. Ervin, L.T. Le, W.Y. Lee, Inkjet-printed flexible graphene-based supercapacitor, Electrochim. Acta 147 (2014) 610–616.
[200] L.T. Le, et al., Graphene supercapacitor electrodes fabricated by inkjet printing and thermal reduction of graphene oxide, Electrochem. Commun. 13 (4) (2011) 355–358.
[201] B. Li, et al., Direct inkjet printing of aqueous inks to flexible all-solid-state graphene hybrid micro-supercapacitors, ACS Appl. Mater. Interfaces 11 (49) (2019) 46044–46053.
[202] A. Sajedi-Moghaddam, M. Gholami, N. Naseri, Inkjet printing of MnO2 nanoflowers on surface-modified A4 paper for flexible all-solid-state microsupercapacitors, ACS Appl. Mater. Interfaces 15 (3) (2023) 3894–3903.
[203] A. Sobolev, P. Stein, K. Borodianskiy, Synthesis and characterization of NiO colloidal ink solution for printing components of solid oxide fuel cells anodes, Ceram. Int. 46 (16) (2020) 25260–25265.
[204] O. Rahumi, et al., Nanostructured engineering of nickel cermet anode for solid oxide fuel cell using inkjet printing, J. Eur. Ceram. Soc. 41 (8) (2021) 4528–4536.
[205] S. Mojabi, N. Afsahi, N. Naseri, Additive manufacturing: New paradigm for developing water splitting systems, Int. J. Hydrogen Energy 49 (C) (2024) 116–142.
[206] M. Cagirici, et al., Direct ink writing of Ni structures for electrocatalytic water splitting applications, Mater. Chem. Phys. 311 (2024) 128574.
[207] J. Fu, et al., Sub-100 mA/cm2 CO2-to-CO reduction current densities in hierarchical porous gold electrocatalysts made by direct ink writing and dealloying, ACS Appl. Mater. Interfaces 15 (23) (2023) 27905–27914.
[208] P.-Z. Li, et al., Inkjet-printed MoS2-based 3D-structured electrocatalysts on Cu films for ultra-efficient hydrogen evolution reaction, Chem. Eng. J. 457 (2023) 141289.
[209] C.-H. Su, et al., Inkjet-printed porphyrinic metal–organic framework thin films for electrocatalysis, J. Mater. Chem. A 4 (28) (2016) 11094–11102.
[210] H.A. Loh, et al., Direct ink writing of graphene-based solutions for gas sensing, ACS Appl. Nano Mater. 2 (7) (2019) 4104–4112.
[211] J. Chen, et al., Highly stretchable photonic crystal hydrogels for a sensitive mechanochromic sensor and direct ink writing, Chem. Mater. 31 (21) (2019) 8918–8926.
[212] M. Dankoco, et al., Temperature sensor realized by inkjet printing process on flexible substrate, Mater. Sci. Eng., B 205 (2016) 1–5.
[213] V. Dua, et al., All-organic vapor sensor using inkjet-printed reduced graphene oxide, Angew. Chem. 122 (12) (2010) 2200–2203.